Master's thesis

NTNU
Norwegian University of Science and Technology
Faculty of Engineering
Department of Structural Engineering

Hedvig Vestad
Magnus Vestad

# Non-linear behaviour of insufficiently grouted post-tensioned concrete members

Master's thesis in Civil and Environmental Engineering
Supervisor: Daniel Cantero
June 2021

NTNU
Norwegian University of
Science and Technology

Hedvig Vestad
Magnus Vestad

# Non-linear behaviour of insufficiently grouted post-tensioned concrete members

Master's thesis in Civil and Environmental Engineering
Supervisor: Daniel Cantero
June 2021

Norwegian University of Science and Technology
Faculty of Engineering
Department of Structural Engineering

NTNU
Norwegian University of
Science and Technology

**Department of Structural Engineering**
Faculty of Engineering
**NTNU – Norwegian University of Science and Technology**

ACCESSIBILITY

Open

# MASTER THESIS 2021

| SUBJECT AREA: Non-linear analysis of prestressed concrete | DATE: 11.06.2021 | NO. OF PAGES: 139 |
|---|---|---|

TITLE:

**Non-linear behaviour of insufficiently grouted post-tensioned concrete members**

Ikke-lineær oppførsel av spennarmerte betongkonstruksjoner med ufullstendig mørtelinjeksjon

BY:

Hedvig Vestad

Magnus Vestad

SUMMARY:

The purpose of this master thesis is to investigate the structural effects of insufficiently grouted post-tensioned concrete members. This was carried out by performing non-linear analyses in the Finite element analysis program DIANA 10.
Reported experiments on four-point bending tests on concrete beams were recreated by performing non-linear analyses and were used to investigate how insufficient grouting can be modelled in DIANA. By using a concept called "bond-slip reinforcements", the user can model the tendon discretely with interface elements. By adjusting the stiffness of these elements, the level of bonding can be defined. A parametric study demonstrated that the choice of stiffnesses had a significant impact on the loss of prestress in the tendon. To proceed, a generic span of a beam bridge was modelled. A new parametric study of the stiffness parameters on the tendon interfaces was performed. Finally, the non-linear behaviour of the bridge was studied.
Both the beam model and the bridge model showed that insufficient grouting did not affect the linear behaviour of the member, while the ultimate capacity was slightly lower. The cracking patterns suggest that a grouted concrete member will have more evenly distributed cracks than an ungrouted member.

RESPONSIBLE TEACHER: Associate professor Daniel Cantero

SUPERVISOR: Associate professor Daniel Cantero

CARRIED OUT AT: Department of Structural Engineering

# Preface

This master thesis is the final work of a five-year-long master's degree programme at the Norwegian University of Science and Technology (NTNU). All the work related to this master thesis has been carried out over a period of 20 weeks in the spring 2021 at the Department of Structural Engineering. The work provides 30 credits per student. Daniel Cantero was the supervisor of this thesis.

Our motivation for working with this particular subject area was to establish a better understanding of bridge design and the finite element analysis. Before we started our work, neither of us had any prior experience with non-linear analyses, so the learning curve has been steep. The work has been challenging but rewarding, and we are certain that the knowledge gained from this thesis can be applied in our professional life.

We would like to thank our supervisor Daniel Cantero for arranging frequent meetings and guiding us through the thesis work. Gianclaudio Pinto has provided us with his knowledge of the DIANA software. Finally, we would like to thank Håvard Johansen from Statens Vegvesen for for his motivational and educational meetings.

Trondheim 11.06.2021

Hedvig Vestad

Magnus Vestad

# Abstract

The purpose of this master thesis was to investigate the structural effects of insufficiently grouted post-tensioned concrete members. This was carried out by performing non-linear analyses in the Finite element analysis program DIANA10.

The thesis is divided into two main parts. Part I was based on the recreation of experiments to gain a greater knowledge of the program. The modelled experiments were four-point bending tests performed on one ordinary reinforced beam and two post-tensioned beams. By comparing the numerical results to the experiments, it could be confirmed that the modelling and iterative analyses were correctly performed and could be used in the further work. One of the post-tensioned beam models was used to investigate how insufficient grouting can be modeled in DIANA by using a concept called ”bond-slip reinforcements”. This concept allows the user to model the tendon discretely with interface elements. By adjusting the normal and shear stiffness of these elements, the level of bonding could be defined. To find appropriate values for the stiffnesses of these elements, a parametric study was performed. The study demonstrated that the choice of stiffnesses had a great impact on the loss of prestress in the tendon.

In Part II of the thesis, the research question was connected to real structures. This was done by modelling a generic span of a post-tensioned beam bridge, inspired by the bridge Rossvollbrua. ”Håndbok R412 - Bruklassifisering” was used to calculate the relevant traffic loads. A new parametric study of the stiffness parameters on the tendon interfaces was performed, as these parameters proved to depend greatly on the element size and geometry of the tendon. Finally, a non-linear analysis was performed on the bridge model.

The results from the beam models and the bridge model showed the same tendencies. The difference between the behaviour of a completely grouted tendon and a tendon without any grouting was small. Until the point of cracking, the two models had the same linear behaviour. For the non-linear part of the load-deformation curves, the ungrouted model had a slightly lower capacity, giving a 7,6 % reduction of ultimate load capacity for the beam models and a 1,8 % lower capacity for the bridge model. The crack pattern when comparing the two cases were very similar, but the results suggest that the cracks of an ungrouted concrete member are concentrated in groups, contrary to the more evenly distributed cracks of a grouted concrete member.

# Sammendrag

Denne masteroppgaven har som mål å undersøke de konstruksjonstekniske effektene av manglende mørtel i etteroppspente betongkonstruksjoner. Dette ble gjort ved å gjennomføre ikke-lineære analyser i element-metodeprogrammet DIANA10.

Oppgaven er delt inn i to hoveddeler. Den første delen av oppgaven baserer seg på å gjenskape forsøk funnet i forskningsartikler for å få nærmere kjennskap til programmet. Forsøkene som ble modellert var firepunkts bøyetester på en passivarmert, og to etteroppspente bjelker. Ved å sammenligne de numeriske resultatene med forsøkene, kunne det bekreftes at modellene var korrekte, og at de valgte innstillingene og iterasjonsmetodene kunne brukes videre i arbeidet. En av de etteroppspente bjelkemodellene ble deretter brukt videre for å kartlegge hvordan manglende mørtel kan modelleres i DIANA, dette ved hjelp av et konsept kalt ”bond-slip reinforcements”. Dette konseptet går ut på at den forspente armeringen modelleres diskret, med elementer på overflaten som kalles ”interface elements”. Ved å regulere normal- og skjærstivheten på disse elementene, kan graden av heft mellom betong og stål justeres. For å finne korrekt stivhet på ”iterface elements”, ble det gjennomført en parameterstudie. Parameterstudien viste at stivheten på ”interface elements” i stor grad påvirket spennkrafttapet under oppspenning.

I den andre delen av oppgaven ble det forsøkt å knytte problemstillingen til eksisterende konstruksjoner. Dette ble gjort ved å modellere et generelt bjelkebruspenn, inspirert av Rossvollbrua. Videre ble det regnet på opptredende trafikklaster etter ”Håndbok R412 - Bruklassifisering”. En ny parameterstudie av stivhets-parametere ble gjennomført, ettersom stivheten til ”interface elements” er avhengig av modellens element-størrelse og armeringens geometri. Det viste seg at stivhetsparameterene som ga den minste forskjellen mellom numeriske og eksperimentelle resultater i del én, ikke kunne brukes for brumodellen. Til slutt ble det utført en ikke-lineær analyse av brumodellen.

Resultatene fra bjelkemodellene og brumodellen viste de samme tendensene. Det ble funnet svært liten forskjell mellom oppførselen til et fullstendig mørtelinjisert og et uinjisert spennarmeringsrør. Frem til oppsprekking hadde de to modellene helt lik lineær oppførsel. For den ikke-lineære delen av last-deformasjonskurven og frem til brudd, hadde modellen uten mørtel en noe lavere lastkapasitet, og ved brudd var denne 7,6% lavere for bjelkemodellen, og 1,8% lavere for brumodellen. Sprekkemønsteret var også svært likt, uavhengig av om mørtel var til stede, men resultatene antyder at sprekkene konsentreres i grupper for uinjiserte spennarmeringsrør.

# Definitions

### Abbreviations

The following abbreviations have been used throughout this thesis:

NS-EN1992-1-1:2004 [1] is referred to as Eurocode 2.

”Håndbok R412 - Bruklassifisering” is referred to as R412

The DIANA FEA software, version 10.4, provided by DIANA FEA BV, is referred to as DIANA.

### Sign conventions

When the results from the analyses from DIANA are discussed, it was decided to use the same sign conventions as in the software;

- Tensile forces are defined as positive
- Bending moments causing tension of the upper edge of the model is defined as positive
- Downward deflections were defined as positive when the analyses were discussed and the load-deflection curves were produced. However, DIANA defines deformations as positive along the positive axes, so the reader must note that the sign conventions does not always coincide when a DIANA model is compared to analytical calculations.

### DIANA Manual references

The DIANA Manual has been used to a large extent in the following pages. These manuals have been cited in the following fashion; [Reference, DIANA version.X, Chapter.X.X]
For example, [ [2] DIANA 10.1, 10.1.3] refers to DIANA Manual-10.1, Chapter 10.1.3.

# List of symbols

*Latin upper case letters*

| | |
|---|---|
| $A_c$ | Cross-sectional area of concrete |
| $A_p$ | Cross-sectional area of prestressing steel |
| $A_s$ | Cross-sectional area of passive reinforcement |
| $E_c$ | Modulus of elasticity of concrete |
| $E_p$ | Modulus of elasticity of prestressing steel |
| $E_s$ | Modulus of elasticity of reinforcing steel |
| $G_c$ | Concrete compressive fracture energy |
| $G_f$ | Concrete tensile fracture energy |
| $P$ | Prestressing force after immediate losses |
| $P_{max}$ | Jacking force |
| $R$ | Reaction force |

*Latin lower case letters*

| | |
|---|---|
| $e$ | Eccentricity |
| $f_{cc}$ | Compressive strength of concrete |
| $f_{cd}$ | Design value of concrete compressive strength |
| $f_{ck}$ | Characteristic compressive cylinder strength of concrete at 28 days |
| $f_{cm}$ | Mean value of concrete cylinder compressive strength |
| $f_{ct}$ | Tensile strength of concrete |
| $f_{p0,1}$ | 0,1% proof-stress of prestressing steel |
| $f_p$ | Tensile strength of prestressing steel |
| $f_{fy}$ | Yield strength of reinforcement |
| $f_{fyd}$ | Design yield strength of reinforcement |
| $k_{n,s}$ | The stiff normal stiffness parameter of the reinforcement interface elements |
| $k_{n,w}$ | The weak normal stiffness parameter of the reinforcement interface elements |
| $k_{t,s}$ | The stiff shear stiffness parameter of the reinforcement interface elements |
| $k_{t,w}$ | The weak shear stiffness parameter of the reinforcement interface elements |
| $n1$ | Number of notional lanes |
| $w$ | Width of carriageway |

*Greek lower case letters*

| | |
|---|---|
| $\alpha_{cc}$ | Coefficient used to calculate the concrete compressive strength |
| $\gamma_c$ | Partial factor for concrete |
| $\gamma_s$ | Partial factor for steel |
| $\Delta\epsilon_p$ | Change of strain for the prestressed reinforcement |
| $\epsilon_{p0}$ | Initial tensile strain of the prestressed reinforcement |
| $\epsilon'_{p0}$ | Resulting tensile strain of the prestressed reinforcement |
| $\epsilon_u$ | Ultimate strain |
| $\theta$ | Angle |
| $\mu$ | Coefficient of friction between the tendons and their ducts |
| $\nu$ | Poisson's ratio |
| $\rho$ | Density |
| $\sigma$ | Stress |

# Table of Contents

# 1 Introduction

This thesis is written as a part of Statens Vegvesen's "Bedre Bruvedlikehold" project. The aim of "Bedre Bruvedlikehold" is to develop methods to be able to prioritize which bridges are to be maintained [3]. NTNU is one of the partners of the project and has contributed with master thesis on topics regarding corrosion in post-tensioned bridges and alkali-silica reactions. As a part of the topic of damages in post-tensioned systems, studying and modelling the structural effects of insufficient grouting is treated in this thesis.

**Background**

Post-tensioning systems make it possible to build long spans and slender bridges. However, after tensioning and grouting, it is impossible to assess the state of the tendons. Human errors, as well as the choice of grouting material, can cause air pockets or voids to occur in the ducts in which the tendons are placed. When corrosion appears in these voids, the damages can be severe [4]. However, the direct structural effects of these voids are less known.

To investigate the damages in this situation, the non-linear behaviour has to be studied. When dealing with non-linear calculations, sophisticated computational programs have to be used. DIANA FEA is an acknowledged finite element analysis software that can be used in a wide range of engineering sectors. As non-linear analyses are quite complex, experience and knowledge is required to determine the validity of the results. It is important to understand the modelled problem and the impact of the different parameters to ensure a successful solution.

**Method**

To ensure a successful solution of the non-linear analyses, a literature study of the different functions in DIANA was performed. To further ensure that modelling was done correctly, it was decided to first recreate experimental results from provided research articles before a more advanced generic bridge model could be made. To model different levels of grouting, a concept called "bond-slip reinforcements" was used. Analytical calculations were made to control the numerical calculations.

**Layout**

The thesis is divided into chapters to best represent how the work developed. Following the introduction chapter, some basic theory and knowledge about post-tensioned constructions and some examples of insufficiently grouted bridges are presented. The next chapter explains the functions and analysis approaches provided by DIANA that have been used. This is meant to provide some insight into the theory behind a non-linear analysis. Then the thesis is divided into two parts. Part I contains details regarding the reference experiments on flexural bending tests on concrete beams. The modelling procedures and analysis setup used for these beams are stated, before the results are presented. Part II contains details regarding the modelling approach for the generic bridge model as well as the results from the non-linear analyses. Finally, the thesis is discussed and concluded.

# 2 Theory

## 2.1 Post-tensioned systems

In a prestressed concrete member, there has been introduced internal stresses of such magnitude and distribution that the stresses developing from external forces are counteracted [5]. As concrete is a material that works poorly in tension, the prestressing method applies a pre-compression to the concrete, which can eliminate undesirable tensile stresses. In other words, a concrete stress control is achieved. Through prestressing, both cracks and deflections can be limited and even avoided. As a result, prestressing systems make it possible to build concrete structures with larger spans that can sustain higher external forces than with ordinary reinforced concrete.

The internal forces resulting from a prestressing force, are obtained by applying a jacking force $P_{max}$ on the prestressing steel, which produces an initial tensile strain $\epsilon_{p0}$ [6]. After applying the prestressing force, the active reinforcement is fixed to the concrete member using anchors, resulting in a total strain of $\epsilon'_{po}$ in the reinforcement, which includes all effects commonly referred to as loss of prestress. This tensile strain is the source of the internal stresses present in prestressed concrete members, as the steel will try to counteract the strain and, as a result, produces a compressive force *P* uniformly distributed over the concrete cross-sectional area.

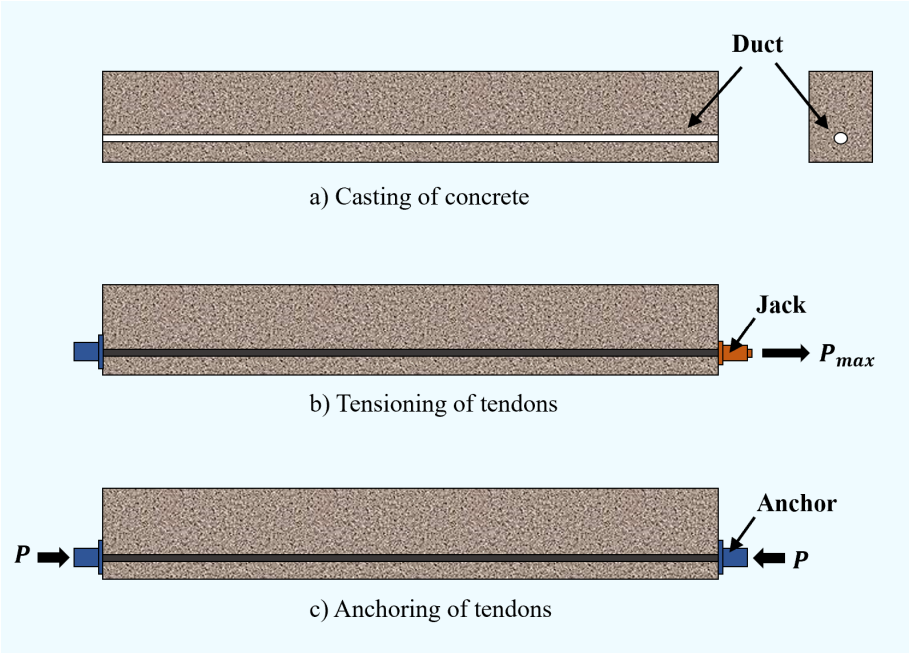


Figure 1: Simplified drawing of the post-tensioning procedure [7]

The prestressing systems are generally classified in two categories; *pre-tensioned* and *post-tensioned* systems [5], depending on the manufacturing process. In a pre-tensioned concrete member, the tendons are

stressed before the concrete is placed in the casting bed. In post-tensioned systems, which are discussed in this thesis, the prestressing is applied by using a jack after the casting when the concrete has hardened. This is shown in figure Figure 1 b). To avoid the prestressing force affecting the concrete, which would cause the concrete to crack instantly as it cannot withstand tensile forces, the tendon is placed inside a hollow conduit, called a duct. The duct ensures a minimal level of bonding between the concrete and the tendon during the jacking process. After the pre-strain is successfully achieved in the tendon, the two materials are connected with anchors, as seen in figure Figure 1 c), and the bonding between the concrete and the tendon is created by injecting grout into the ducts. From this point on, the strains of the concrete and the tendon will be compatible, meaning that the change of strain at the same level of the same cross-section, $\Delta\epsilon_p$ will be equal for the two materials. The appearing strains during the manufacturing and loading of the beam are shown in Figure 2.

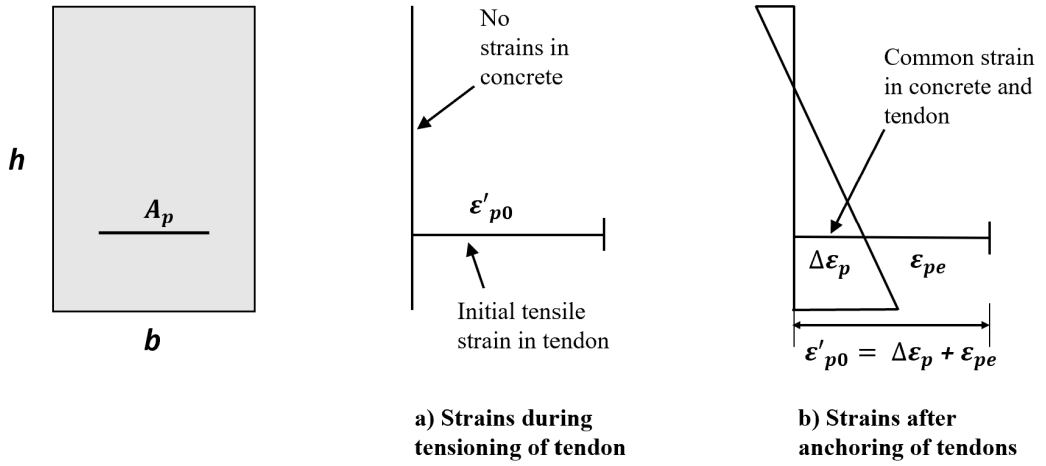


Figure 2: Idealized drawing of the strains during the jacking and loading of a Post-tensioned concrete member [6]

Alternatively, there is a way to post-tension the concrete with no bonding by not injecting grout into the ducts [6]. Normally, this is done by using pre-assembled tendons in plastic ducts filled with grease. The benefit of this method is that the grease will provide low friction during the tensioning phase, so the loss of prestress will decrease. Moreover, the problems connected to grouting are avoided. The disadvantages of using unbonded tendons are that the ultimate capacity normally becomes lower and that the reinforcement will not contribute to the cracking distribution. Moreover, special attention is required to ensure that the strand is protected from corrosion, where it enters the end anchorages. [8]

## 2.2 Insufficient grouting in post-tensioned bridges

Even though a fully bonded reinforcement is desired, this is not always the case. Mistakes during the construction, such as an incoherent grouting process, can cause air pockets or voids to occur in the grouting ducts [9]. These voids will result in a loss of bonding between the concrete and the reinforcement, and the reinforcement will be more prone to corrosion since the reinforcement is left unprotected.

In addition to human errors, the choice of material can also affect the level of grouting in the tendons. Notably, "Bleed water" can occur as a result of the separation and sedimentation of the grout. Because the heavier materials will sink to the bottom of the duct, water is pushed to the top. In most bridges, the reinforcement has a parabolic shape. As the water will run down to the low points of the reinforcement, the voids from bleed water are usually concentrated in high points of the reinforcement duct. These points are normally found over supports and abutments.

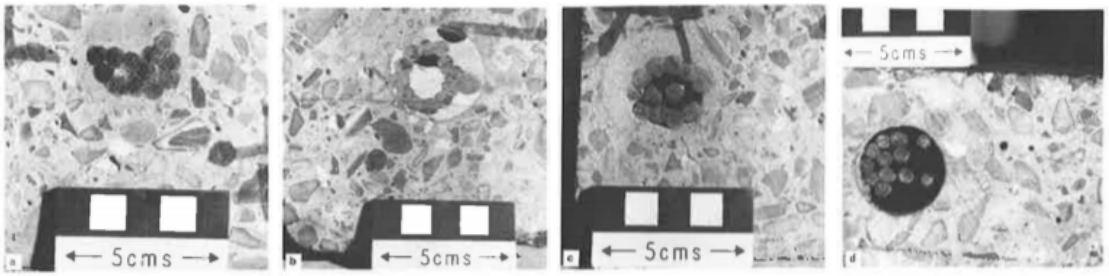


(a) Fully grouted duct. (b) Small air void. (c) Void between wires. (d) Empty duct.

Figure 3: Different levels of grouting [4]

The lack of grouting in these voids leaves the reinforcement less protected from corrosion and can be a possible entry point for corrosive chemicals and water. In cold climates, voids in the grouting ducts can be areas prone to freeze-thaw processes and frost damages, causing undesirable stress concentrations in the structure. [10]. It is particularly important to protect the post-tensioned reinforcement from corrosion. When the reinforcement corrodes, it will first expand, but if the corrosion is persistent, the reinforcement area will be reduced [11]. The change in stresses due to this change of area is large for post-tensioned reinforcements, as it is already tensioned by 60-75% of its tensile capacity [12]. The large change in stresses can, in a worst-case scenario, lead to failure of the whole tendon.

It is essential that the grouting process is executed without any mistakes, as it is very difficult to detect voids after the construction is built. The state of the tendons is mainly attained through observations during the grouting process [10]. There are some non-destructive approaches to detect voids after the construction is built, but these approaches can be difficult to use and the results can be even more difficult to interpret.

The damages connected to insufficient grouting can be catastrophic. Figure 4a shows the Ynys-y-Gwas bridge, which collapsed in 1985 in Wales. It was found that insufficiently grouted tendons were one of the contributing factors to the collapse [4]. Inadequate protection of the joints, as well as large voids where the

corrosion could extend along the length of the tendon, contributed to the collapse.

Likewise, the Saint Stefano bridge collapsed in 1999 in Italy, presented in Figure 4b. It was found that pitting corrosion near the box girder joint had caused the failure of the bridge. [13].

(a) The collapsed Ynys-y-Gwas bridge [4].

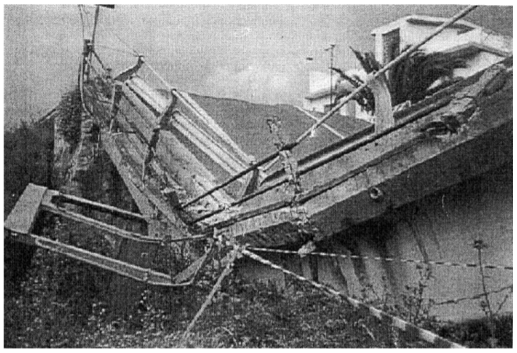

(b) The collapsed St.Stefano bridge [13].

Figure 4: Collapsed bridges

Given the length of the working life of concrete bridges, it should be mentioned that the post-tensioning technology is relatively new and that the bridges that collapsed were some of the first post-tensioned bridges built. At the time the Ynys-y-Gwas bridge was built, there would have been no anticipation of the combined impact of insufficiently grouted tendons and chloride penetration [14]. Following the collapse of the Ynys-y-Gwas bridge, the United Kingdom imposed a ban from 1992 to 1996 on the construction of post-tensioned bridges [15]. Today, there are multiple standards and regulations to ensure that the work is executed correctly. Moreover, the damages are taken seriously. In ”Publikasjon 14” [10] published by the Norwegian Concrete Association, it is suggested that the tendon should be considered as ”broken” if a void is discovered.

# 3 Modelling and non-linear analysis of Post-tensioned concrete members in DIANA

DIANA offers multiple ways of modelling, and there is a great variety of material models and behaviours to choose from. In that regard, this thesis will offer a short explanation of the theory behind the chosen modelling parameters. Some modelling alternatives might be mentioned, but if the reader wants further information on these alternatives, it is recommended to look them up in the DIANA manual [2].

The DIANA tutorials ”Pre-and post-tensioning of a concrete beam” [7] and ”Reinforced Concrete Beam: Simulation of an Experimental Test” [16] provides useful insight on the different modelling methods for pre-and post-tensioning behaviour of tendons in concrete. These tutorials, as well as relevant chapters from the DIANA 10.4 Users’ manual, [2], have provided the relevant information for this section.

## 3.1 Material models

Material models used in a finite element context specify the stress-strain relationship, that is assumed for the materials in the structure [17]. The material models are simplified abstractions of the true material behaviour.

### 3.1.1 Crack models

There are two main approaches for modelling cracking in concrete; *The discrete cracking* approach and *the smeared cracking* approach. When using the discrete cracking approach, fracture is assumed to occur when the nodal force normal to the element boundaries exceeds the tensile strength criterion [18]. Then, at that node location, new degrees of freedom are introduced. It is assumed that a geometrical discontinuity will occur between the original and the newly created node. The disadvantages of using this method are the computational difficulties connected to the continuous change in topology, and that mesh bias is introduced because cracks are forced to propagate along element boundaries.

In the smeared cracking approach, which is used in this thesis, a cracked solid is imagined to be a continuum where the notions of stress and strain are still valid. The behaviour of concrete is then described in terms of isotropic stress-strain relations which can be replaced by an orthotropic stress-strain relation upon cracking [19]. This approach is computationally efficient as the topology of the original finite element mesh remains preserved. The smeared cracking models can be further divided into *fixed crack models* and *rotating crack models*. DIANA offers multiple approaches to model the smeared rotating crack models. In ”Guidelines for Nonlinear Finite Element Analysis of Concrete Structures” [17] a total strain-based rotating crack model, which is used in this thesis, is recommended. This is because the rotating model usually results in a lower-limit failure as it does not suffer as much from spurious stress-locking.

### 3.1.2 Material models for concrete

When defining the properties of the concrete material in DIANA, the stress-strain relationship for the concrete tensile behaviour and the concrete compressive behaviour is modelled separately.

There are multiple approaches to modelling the tensile behaviour of total strain crack concrete models. When modelling tensile behaviour in smeared crack models, the functions are usually based on the tensile fracture energy, $G_f$, which is related to crack bandwidth. DIANA offers six different functions to model the tensile behaviour of concrete based on its tensile fracture energy calculated by Equation 1 [17].

$$G_f = 73\, f_{cm}^{0,18} \tag{1}$$

"Guidelines for Nonlinear Finite Element Analysis of Concrete Structures" [17] states that an exponential softening diagram is preferred, as the diagram will result in more localized cracks and consequently avoid large areas of diffuse cracking. In DIANA, the exponential softening diagram is a predefined function dependent on the tensile fracture energy $G_f$, and the tensile strength $f_{ct}$ as well as the crack bandwidth *h*, as presented in Figure 5a. The exponential softening function is predefined, which means that the user does not have to input the crack bandwidth *h* as it can be automatically calculated by DIANA [20]. The tensile behaviour can be modelled further by applying a damage based reduction of the Poisson's ratio[ [2]DIANA 10.4, 46.5.4]. This gives the concrete a more realistic behaviour as the Poisson effect of the concrete ceases to exist in a cracked state. Stretching of a cracked direction does no longer lead to contraction of the perpendicular directions.

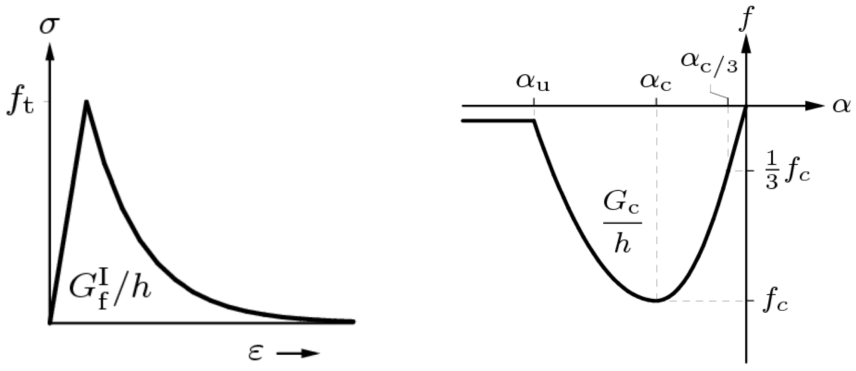


(a) Predefined exponential softening curve (b) Parabolic compression curve

Figure 5: Material models for concrete [ [2] DIANA 10.4, 46.5.4]

Just as for the tensile behaviour, there are multiple approaches to model the compressive behaviour of the total strain crack concrete model. Here, a parabolic stress-strain diagram based on the compressive fracture energy is recommended. This is in order to reduce the mesh size sensitivity. In DIANA, a parabolic curve based on the compressive fracture energy of the concrete $G_c$, calculated by Equation 2 [17] and the

compressive strength of concrete $f_c$ is available.

$$G_c = 250 G_f \tag{2}$$

In Figure 5b, the three points $\frac{\alpha_c}{3}$, $\alpha_c$ and $\alpha_u$ is automatically calculated by DIANA, as the function is predefined. The different $\alpha$ values are dependent on the concrete compressive strength, $f_c$, the elastic modulus $E_c$, the compressive fracture energy, $G_f$ and the crack bandwidth *h*. A more detailed compressive behaviour can be modelled by applying strength reduction by lateral cracking. Compressed concrete will have a *lateral confinement* effect as it will get increased strength and ductility with increasing isotropic stress, but at the same time, the strength should be reduced due to lateral cracking [20]. The lateral confinement is modelled in DIANA by selecting different parameters for the increasing and reducing strength respectively. The user may also choose to neglect these effects.

### 3.1.3 Material models for reinforcements

To represent the non-linear behaviour of the reinforcements, an elastoplastic material curve can be used. In DIANA, this non-linear model is called the Von Mises plasticity model [ [2] DIANA 10.1, 10.1.3]. Figure 6 shows the idealized stress-strain diagram for a Prestressed reinforcement which is recommended in Eurocode 2. [referanse her] This diagram is applied both for tensile and compressive stresses. Up to the yield stress $f_{p0,1}$ the model is linear, with an elastic modulus $E_p$. When the yield stress is surpassed according to the Von Mises yield criterion, the ductile phase begins. The user can define the ductile behaviour in DIANA by choosing a hardening function. The ”no hardening” option sets the yield stress as the maximum appearing stress, giving a horizontal top branch in the diagram. For the ”no hardening”-option, no point of failure is specified. The ductile behaviour can also be modelled as an inclined branch, with a defined point of failure at the strain limit $\epsilon_u$ with a maximum stress $f_p$.

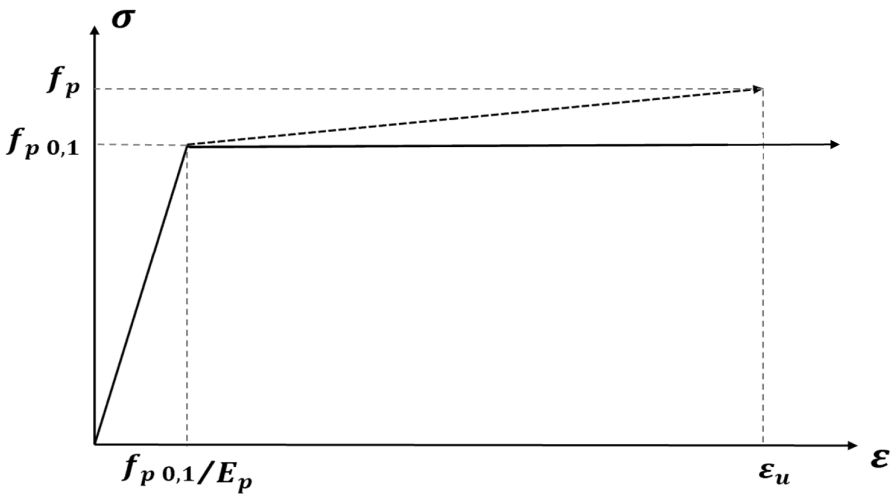


Figure 6: Stress-strain curve for Prestressing steel

### 3.1.4 Materials for support, load and anchorage plates and their interfaces

The problem with applying the point load to a single node of the concrete member is that such a big stress concentration can give instant cracking or crushing of the concrete at this point. When modelling concrete structures, the DIANA tutorials recommend to create support- and load plates at the points where the supports are defined or point loads are applied. For post-tensioned concrete models, anchorage plates can also be modelled in the same way. An example of a support plate is shown in Figure 7. The plates are normally modelled using steel with linear behaviour and no defined yielding point. Therefore, it can withhold stresses of any given magnitude. When applying point loads or reaction forces at the steel plates, the forces will be distributed over the thickness of the steel plate, as seen in Figure 7a.

On the surface between the steel plate and the concrete, an *interface* is defined to attach them to each other. In DIANA, the interfaces are marked as red and green T-shapes, as seen in Figure 7a. An interface material is defined using a non-linear elasticity model. A high value is used for the compressive normal stiffness and a low value is used for the shear stiffness. Therefore, this support is modelled as a roller support since the concrete can move relative to the steel plate in the horizontal direction. For the tensile behaviour, the model ”No-tension with shear stiffness reduction” is used, to ensure that the steel plate does not transfer any tensile forces to the concrete surface. Figure 7b shows how only the compressive forces are transferred to the concrete surface.

Interface elements are also used to describe bond-slip behaviour, which is explained further in Section 3.2.3.

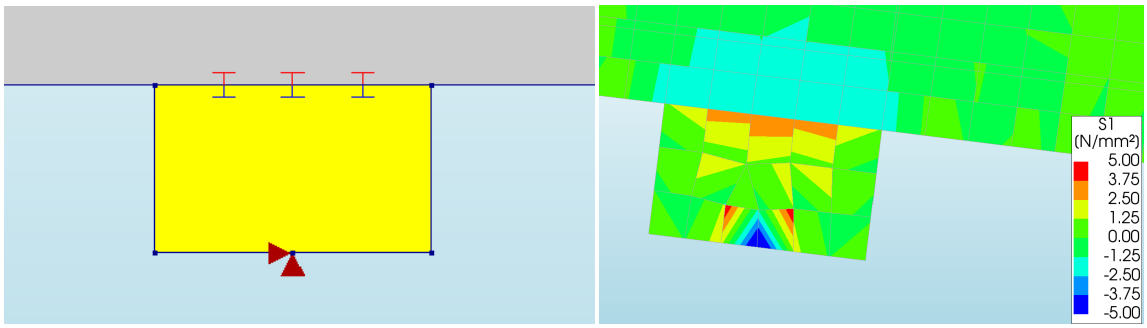


(a) Geometry of the support plate.

(b) Appearing Cauchy principle stresses when an upward reaction force appears on the support.

Figure 7: A support plate modelled on the bottom face of a concrete model.

## 3.2 Finite element types and meshing

### 3.2.1 Concrete elements

The choice of element types for the concrete depends on whether the project is modelled in two or three dimensions. The relevant finite elements for this thesis are the plane stress elements, which are used in two-dimensional modelling, and the three-dimensional solid elements.

Plane stress elements, also called membrane elements, have a plane geometry in the sense that their shape

is defined only in the *xy* plane. Optionally, a constant and small thickness *t* is defined in the *z*-direction [ [2]DIANA 10.4.4, I. Structural Elements], as presented in Figure 8a. The thickness *t* allows this type of element to be used for three-dimensional models that have a constant thickness in one direction, provided that the out of plane stress components $\sigma_{zz}$, $\sigma_{yz}$ and $\sigma_{xz}$ are zero [21]. This implies that the model can only be loaded in the *x* and *y* directions, in the plane of the element, and therefore, that there is no out-of-plane bending. The advantage with plane stress elements is that it allows a faster finite element analysis, as the stiffness matrices are reduced to a size of 3x3. The Q8MEM element, which is a four-nodal isoparametric plane stress element, has been used for the 2D modelling in this thesis.

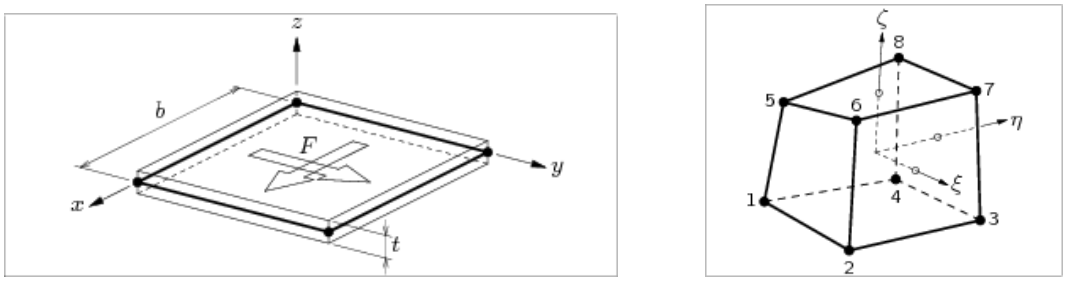


(a) Regular plane stress element (b) Eight-node isoparametric solid brick element (HX24L)

Figure 8: Finite element types used for the concrete material [ [2] DIANA 10.4.4, I. Structural Elements]

Solid elements are the most complex but also the most versatile finite element type in DIANA [22]. These elements are three-dimensional, and can adapt to complex, voluminous shapes. The stiffness matrices include translation and rotation about all three axes, which is particularly important when the loading directions are arbitrary [ [2]DIANA 10.4.4, I. Structural Elements]. The large system of equations which is generated during an analysis with this element type yields time-consuming computations, but the most precise results. The type of solid element used in this thesis, presented in Figure 8b, are linear brick-shaped elements with eight nodes, HX24L.

### 3.2.2 Embedded reinforcements

In DIANA, the presence of a reinforcement bar in a concrete model is normally considered by defining the shape of the reinforcement as lines, called *embedded reinforcements*[ [2]DIANA 9.6, 7.9]. These lines are not finite elements of their own, and thus, they do not have degrees of freedom. Instead, the stiffness contribution from the embedded reinforcement is calculated by adjusting the stiffness of the adjacent concrete elements, also called the *mother elements*. The resulting stiffness is computed by considering the position of the reinforcement, its material properties, and its cross-section. However, the space occupied by the reinforcement, as well as its weight, is not affecting the mother element. As seen in Figure 9, the reinforcement bar is divided in *particles* which lies within a mother element. Inside a particle, several *location points* are defined, with *integration points* in between them.

After the displacement field of the mother element is found, it is used to find the displacement $\xi$ of the location points on the reinforcement. Based on the displacements of the two closest location points, the

strains $\epsilon_{xx}$ and the stresses, $\sigma_{xx}$ are found along a vector $\hat{x}$. This vector is located at the integration point of the reinforcement, in the direction tangential to the bar axis. The displacement of the concrete element defines the displacement of the reinforcement, which means they are not able to move independently from each other. Therefore, embedded reinforcements represent a perfect bond.

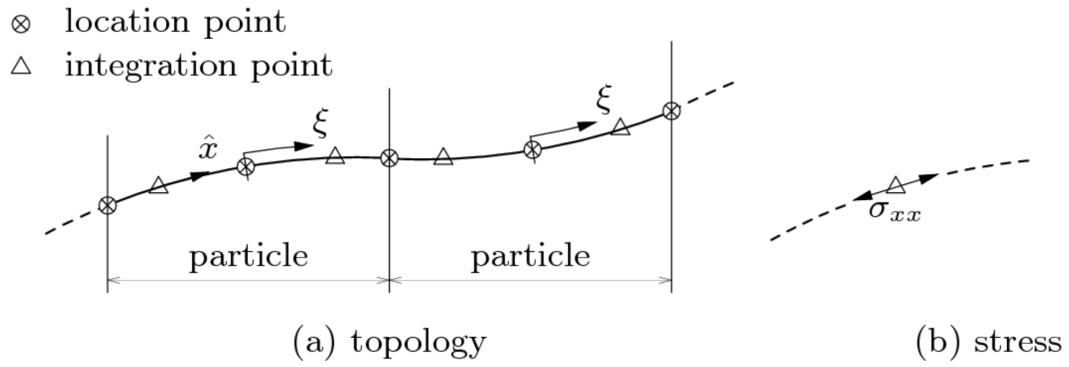


Figure 9: The embedded reinforcement bar inside a mother element [ [2] DIANA 9.6, 7.9]

### 3.2.3 Bond-slip reinforcements and reinforcement interface elements

Unlike the embedded reinforcements, the bond-slip reinforcement bars allows the user to model a relative slip $\Delta u$ between the reinforcement and the mother elements, which means that the deformation of the reinforcement is different from the surrounding concrete at a specific point;

$$\Delta u = \delta_{concrete} - \delta_{steel} \tag{3}$$

Equation 3 is computed for each location point, as seen in Figure 9. In this case, the reinforcement bar is defined as an internally modelled finite element[ [2]DIANA 10.1,7.9.2], which can either be truss elements or beam elements depending on the preference of the user. The difference between truss elements and beam elements, is that beam elements also include rotational degrees of freedom.

| | **2D-modelling** | **3D-modelling** |
|---|---|---|
| **Mother element** | Q8MEM | HX24L |
| **Truss reinforcement** | L4TRU | L6TRU |
| **Beam reinforcement** | L7BEN | L13BEN |

Table 1: Elements for bond-slip reinforcements, depending on the choice of mother elements

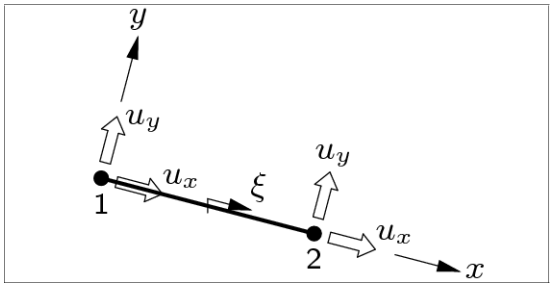


Figure 10: Truss element with four degrees of freedom, L4TRU[ [2] DIANA 10.4.4, I. Structural Elements]

Table 1 shows what types of truss and beam elements that is used for the Q8MEM and the HX24L concrete elements. In this thesis, only truss elements were modelled. For two-dimensional modelling, the element type L4TRU is used. This element has four degrees of freedom, with translations $u_x$ and $u_y$ in each of the two nodes, as seen in Figure 10. For three-dimensional modelling, the translation in the $z$-direction is also included, giving 6 degrees of freedom for L6TRU.

The bond-slip behaviour is discretely modelled by using *interface elements* with zero thickness[ [2]DIANA 10.2, 26] at the interface of the bond-slip reinforcement. The stiffness of the interface material defines the level of bonding of the reinforcement. The relative displacement $\Delta u$ will depend on the stiffness *D* of the interface, which expresses the relationship between the traction $\tau$ acting on the location point, and the displacement $\Delta u$. This stiffness can be decomposed into the stiffness along the *t*-axis parallel to the reinforcement, and the *n*-axis normal to the reinforcement, see Figure 11.

The interface material can either have an elastic or a non-linear behaviour. When there is a linear relationship between the traction and the displacement, there is a constant stiffness $k$ as described by Hooke's law. The stiffnesses are hereby referred to as the shear stiffness $k_t$ and the normal stiffness $k_n$. Effectively, the relationship between the traction force and the displacement in each of the directions can be described as

$$\begin{bmatrix} \tau_t \\ \tau_n \end{bmatrix} = \begin{bmatrix} D_{11} & 0 \\ 0 & D_{22} \end{bmatrix} \cdot \begin{bmatrix} \Delta u_t \\ \Delta u_n \end{bmatrix} = \begin{bmatrix} k_t & 0 \\ 0 & k_n \end{bmatrix} \cdot \begin{bmatrix} \Delta u_t \\ \Delta u_n \end{bmatrix}$$

where $\tau_t$ is shear traction, and $\tau_n$ is the normal traction[ [2] DIANA 9.5, 10.2.2].

Figure 11 demonstrates how the interface material works on a location point of the model, by representing it as two points attached by springs. The two red points represents the location point at either side of the interface. Before loading, these points would be overlapping, as there is not yet any relative displacement. After loading, we will have a relative displacement between the concrete and the steel dependent on the stiffnesses $k_t$ and $k_n$. For straight post-tensioned reinforcements, $k_t$ is the only parameter affecting the model, as no vertical displacement is expected. This is because the post-tensioning force $P$ is horizontal along the tendon. For a tendon with a parabolic shape, $P$ has a vertical component along the tendon, which means that $k_n$ must be defined to represent the bond-slip.

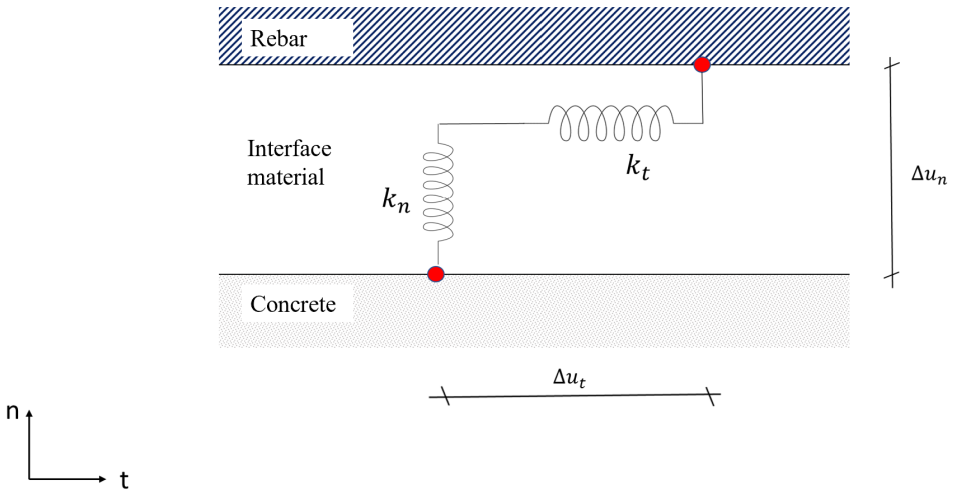


Figure 11: Idealized model of the interface material. It should be noted that the real thickness of the interface material in DIANA is zero.

The bond-slip model can be developed further by introducing a non-linear relationship between the shear traction $\tau_t$ and the shear slip $\Delta u_t$, while the behaviour in the normal direction is still described by a linear relationship $k_n$. This kind of modelling is recommended by the DIANA tutorial "Pre- and post- tensioning of a concrete beam" [7]. A cubic function introduced by Dörr (1980) gives a more realistic representation of the complex interaction between the reinforcement and the concrete [ [2]DIANA 10.2, 26]. The linear relation $\tau_t = k_t \cdot \Delta u_t$ is replaced with the function $\tau_t = f_t(dt)$ as described by Dörr:

$$\tau_t = \begin{cases} c\left(5\left(\frac{\Delta u_t}{\Delta u_t^0}\right) - 4.5\left(\frac{\Delta u_t}{\Delta u_t^0}\right)^2 + 1.4\left(\frac{\Delta u_t}{\Delta u_t^0}^3\right)\right) & \text{if } 0 \leq \Delta u_t < \Delta u_t^0 \\ 1.9c & \text{if } \Delta u_t \geq \Delta u_t^0 \end{cases} \tag{4}$$

The cubic function is shown in Figure 12. Observe that up to a certain value of the relative displacement, $\Delta u_t^0$, there is a polynomial relation between the shear traction $\tau_t$ and the displacement $\Delta u_t$. The shear traction will then reach a maximum level of $1.9c$. After the displacement $\Delta u_t^0$ is reached, the shear traction will have a constant value of $\tau_t = 1.9c$, which means there is no bonding between the reinforcement and the steel. The limit before this plateau is reached, is therefore defined by the parameter $c$. In DIANA, the user can manually set the parameter $c$ to define the level of bonding at the interface. If a large value is set for the parameter, typically $f_{ct}$, the shear traction $\tau_t$ will reach a relatively high value before the reinforcement slips from the concrete, giving a negligible bond-slip $\Delta u$. In DIANA, this scenario should therefore be similar to the embedded reinforcements. On the contrary, a very low value of $c$, will mean that this no-bond situation happens instantly when applying the loads, allowing no traction forces on the interface.

This corresponds to the flat part of the curve in Figure 12.

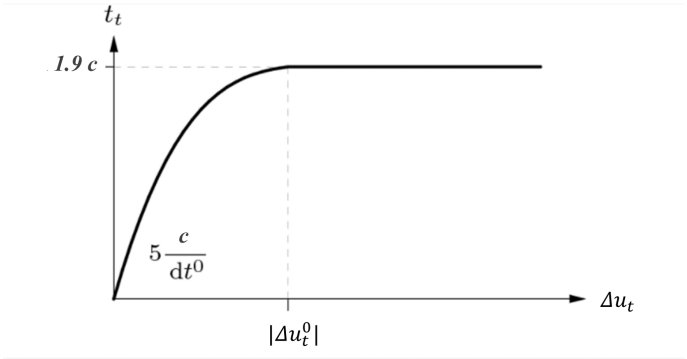


Figure 12: Dörr's cubic function for bond-slip as expressed in Equation 4

### 3.2.4 Choice of mesh size

The size of the finite elements play a vital role on the accuracy of a non-linear finite element analysis [17]. The element size should be small enough to give a quite smooth stress field. For a beam structure, the recommended element size can be chosen based on the recommendations in Table 2.

| | **Maximum element size** |
|---|---|
| **2D modelling** | $\min\left(\frac{l}{50}, \frac{h}{6}\right)$ |
| **3D modelling** | $\min\left(\frac{l}{50}, \frac{h}{6}, \frac{b}{6}\right)$ |

Table 2: Recommended maximum element sizes
for a beam with a span $l$, a height $h$ and a width $b$ [17].

However, it is recommended to compare results with different finite element discretizations to detect any weaknesses of the model, or distortions, and evaluate whether a further refining of the mesh is necessary. As the computational time increases considerably by refining the mesh, this should always be taken into account.

### 3.2.5 Composed line elements

Composed line elements can be added to a model in DIANA, with the sole purpose of calculating the cross-section forces and bending moments in the model after the analysis[ [2] DIANA 9.4.4, 13.8]. The calculations are based on the stress field in each cross-section of the model. The composed line does not influence the geometry or the behaviour of the model during loading, but is simply a tool for the post-processing of the results.

## 3.3 Numerical iterative approaches

In a non-linear finite element analysis, the relation between a force vector and a displacement is no longer linear[ [2] DIANA 10.4, 75.1]. Similarly to a linear analysis, the purpose is to calculate a displacement vector with equilibrium between the internal and external forces. Contrary to the linear analysis, the compatibility in the non-linear analysis is based on the deformed geometry of the element. Given that the geometry of the element is changing by deformations, the stiffness of the element will also change. In other words, the stiffness matrix **K**, representing the relation between forces and displacements, is no longer constant.

To determine the state of equilibrium in a non-linear analysis, the problem has to be discretised in space, with finite elements, and in time, with increments[ [2] DIANA 10.4, 75.1.1]. To achieve equilibrium at the end of the increment, an iterative solution algorithm can be used. An *incremental-iterative* solution is the combination of the two methods.

For all iterative procedures, the total displacement increment $\Delta u$ is adapted iteratively. This is done by iterating increments $\delta u$ until equilibrium, within a chosen tolerance, is reached[ [2] DIANA 10.4, 75.1.1]. The incremental displacements are calculated from Equation 5.

$$\Delta u_{i+1} = \Delta u_i + \delta u_{i+1} \tag{5}$$

There are multiple iteration methods in DIANA, and in this thesis the Regular Newton-Raphson method, hereby referred to as *the Newton-Raphson method*, and the Quasi-Newton method, also called *the Secant method*, have been used. As mentioned above, the stiffness matrix **K** represents some kind of linearized form of the relation between the forces and the displacements. The stiffness matrix can change for every iteration, and can be used to determine the iterative increment $\delta u$ as shown in Equation 6, where $g_i$ is the out-of-balance force vector at the start of iteration *i*. The difference between several of the iterative procedures is the way in which the stiffness matrix is used to determine the iterative increments.

$$\delta u_i = {\mathbf{K}_i}^{-1} g_i \tag{6}$$

### 3.3.1 Newton-Raphson method

The Newton-Raphson method, see Figure 13, converges to the final solution in only a few iterations due to its quadratic convergence characteristic.

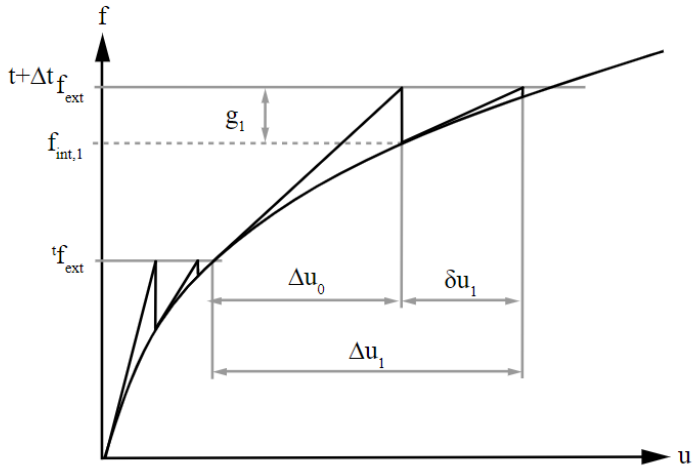


Figure 13: Newton-Raphson iteration [ [2] DIANA 10.4, 75.1.1.1]

Equation 7 is used to find the stiffness matrix $\mathbf{K}_i$ which represents the tangential stiffness of the structure and is used in Equation 6.

$$\mathbf{K}_i = \frac{\partial g}{\partial \Delta u} \tag{7}$$

The stiffness relation from Equation 7 is evaluated after every iteration. This means that the prediction of the iterative increment $\delta u$ is based on the last predicted situation even if it is not an equilibrium state. In "Guidelines for Nonlinear Finite Element Analysis of Concrete Structures" [17] a Newton-Raphson iterative method is recommended, as it is sufficiently accurate and efficient. There are, however, some disadvantages to the method. The stiffness matrix **K** has to be set up and potentially decomposed for every iteration. This process can be time-consuming. Moreover, the Newton Raphson method is prone to divergence if the initial prediction is far from the final solution.

### 3.3.2 Secant method

Contrary to the Newton-Rahpson method, the Secant method does not set up a completely new stiffness matrix for every iteration. The inverse stiffness matrix $\mathbf{K}_{i+1}^{-1}$ can be derived directly from the previous stiffness matrix.

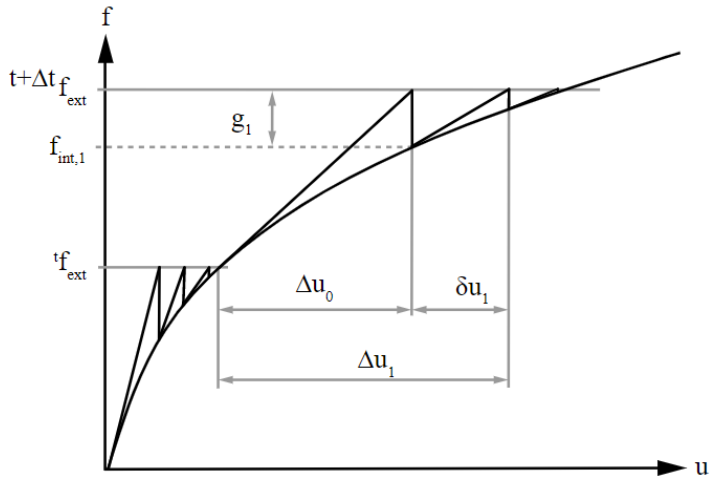


Figure 14: Secant method iteration [ [2] DIANA 10.4, 75.1.1.2]

The Secant relation for the iterative displacement increment, $\delta u$, and the change in out-of-balance force vector, $\delta g_i = g_{i+1} - g_i$ is presented in Equation 8. The stiffness of the structure is determined from the known positions at the equilibrium path, and the method uses the information of previous solution vectors and out-of-balance force vectors during the increment to achieve a better approximation.

$$\mathbf{K}_{i+1}\delta u_i = \delta g_i \tag{8}$$

There are three different Secant methods in DIANA; The Broyden method, the Chrisfield method, and the Broyden-Fletcher-Goldfarb-Schanno method, which is used in this thesis and hereby referred to as the BFGS method. It can be shown that Equation 9 and Equation 10 satisfy the Secant relation in Equation 8 by substituting *c*. In the BFGS method, *c* is substituted by $\delta u$, and $\mathbf{K}_{i+1}$ is inverted.

$$\mathbf{K}_{i+1} = \mathbf{K}_i + \frac{(\delta g_i - \mathbf{K}_i \delta u_i)c^T}{c^T \delta u_i} \tag{9}$$

$$\mathbf{K}_{i+1} = \mathbf{K}_i + \frac{(\delta g_i - \mathbf{K}_i \delta u_i)c^T + c(\delta g_i - \mathbf{K}_i \delta u_i)^T}{c^T \delta u_i} - \frac{(\delta g_i - \mathbf{K}_i \delta u_i)^T \delta u_i \; c \; c^T}{(c^T \delta u_i)^2} \tag{10}$$

Effectively, Equation 10 can yield the BFGS relation presented in Equation 11

$$\mathbf{K}_{i+1}^{-1} = (I + \frac{\delta u_i \delta g_i^T}{\delta u_i^T \delta g_i})\mathbf{K}_i^{-1}(I - \frac{\delta g_i \delta u_i^T}{\delta u_i^T \delta g_i} + \frac{\delta u_i \delta u_i^T}{\delta u_i^T \delta g_i}) \tag{11}$$

The resulting stiffness can be calculated from the stiffness matrix $\mathbf{K}_0$ that was used at the start of the increment and an update vector for every iteration. This is done by calculating the iterative displacement $\delta u$ by substitution of Equation 11 in Equation 6.

The Secant method normally converges slower than the Newton-Raphson method [20], but the iterations are usually faster. The BFGS Secant method will demand more memory and storage than the Newton-Raphson method. This is because the updated vectors used for every iteration in the BFGS Secant method is to be stored with size ”number of degrees of freedom”[ [2] DIANA 10.4, 75.1.1.4].

### 3.3.3 Convergence criteria

A suitable convergence criterion has to be chosen so that the iteration process is stopped if the results are adequate or obviously lead to divergence. In DIANA, the convergence criteria are based on a force-norm, displacement-norm, energy-norm, residual-norm or a combination of them. In ”Guidelines for Nonlinear Finite Element Analysis of Concrete Structures” [17] an energy-norm together with a force-norm is recommended, whereas only the energy-norm is used in the DIANA tutorial ”Reinforced Concrete Beam: Simulation of an Experimental Test” [16]. When the type of norm is defined, a vector is calculated to compare the result of each iterative step to the result in a previous step. For example, the force norm is based on the calculation of the out-of balance force vector $g_i$, as stated in Equation 6, which is compared to the initial unbalance of forces $g_0$ [ [2] DIANA 9.4.3, 30.1.4]. This ratio is used to detect whether the results seem to converge or not. The most appropriate type of convergence criteria will depend on the characteristics of the model which is analysed. Notably, a model which can expand freely in one direction, for example a simply supported beam, will not be useful to analyse with a force norm, where a balance between external and internal forces is calculated. This is because the boundary constraints will not cause any internal forces to appear in the structure. The user should also be aware that the energy norm will give a slower iterative process, because it requires an additional iteration to detect divergence.

### 3.3.4 Stepping schemes and arc length control

In a non-linear analysis, the computation is discretised in time, using increments. As explained in the previous subchapters, every increment is calculated using a numerical iteration method. The increments themselves are applied in a stepwise manner, using either an applied load or a prescribed deformation gradually increasing in magnitude [ [2] DIANA 9.6, 11.3.5]. The two methods are called *load control* and *displacement control*.

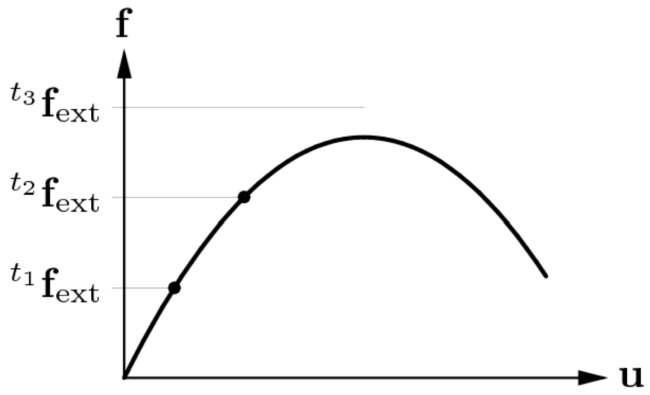


Figure 15: Load step control [ [2] DIANA 10.4, 75.1]

The load control, presented in Figure 15, allows the user to apply a force vector $\boldsymbol{f_{ext}}$ on the model, which is increased by a load step size $(t_{i+1} - t_i)$. Every new step is computed based on the numerical iteration. If not further specified, the load step size of each increment is constant, giving a fixed load increment. This will represent a risk of inaccurate results, because it may give too rough predictions of the displacements if the load-displacement curve is almost horizontal. However, DIANA provides a solution to this, called *the arc length control*. The arc length control can be used to adapt the load step size according to the displacement of a user-specified control node during the analysis. If the displacement of the control node is increasing rapidly, the step size will be reduced. When the arc length control is applied, *snap-through* behaviour and *snap-back* behaviour can be analyzed, which means that a softening behaviour of the model, and a change of the direction of the displacement, will also be detected.

# 4 Modelling level of grouting through bond-slip reinforcments

When modelling a post-tensioned system in DIANA, the two-step prestressing process explained in chapter 2.1 can be imitated by using so-called *execute blocks* during the analysis. In the first block, the post-tensioning force *P* is applied to the active reinforcement. Meanwhile, a no-bonding condition is prescribed between the tendon and the concrete. This ensures that the tendon is able to elongate to a strain $\epsilon_{p0}$ without affecting the concrete. The next execute block is carried out after changing the bonding parameters on the reinforcement interface and will simulate the behaviour of a fully grouted concrete member. The prestressing force is removed, and the anchoring is implemented so that the tendon is fixed to the concrete at both ends of the beam. Then, optionally, the model can be loaded with additional external loads.

DIANA provides two possible methods to model the post-tensioning behaviour of concrete [7]:

- With *embedded reinforcements*, the post-tensioning behaviour is modelled indirectly, which was explained in Chapter 3.2.2. This is a simplified model, which does not include any bond-slip modelling. The method is used to model all passive reinforcement in this thesis.
- With *bond-slip reinforcements*, the bond-slip behaviour of the post-tensioned tendons is discretely modelled, and we use reinforcement interface elements to specify the bond-slip condition as explained in Chapter 3.2.3. This method allows for a detailed bond-slip analysis, where the level of bonding can be manually set by the user.

## 4.1 Modelling and analysis with embedded reinforcements

For the modelling of the embedded reinforcement in DIANA, the following aspects need to be included;

- When the material model for the tendon is defined, the *NOBOND* command must be applied. This command sets a no-bonding condition as a default setting for the tendon, which means that the reinforcement is initially not bonded to the mother elements. This setting will be turned off in the second step of the analysis, after the tensioning phase.
- During the geometry definition of the tendon, *Reinforcement type* is set to ”Embedded”.
- The post-tensioning force $P$, is defined as follows;
  - The prestress force $P$ is assigned to the whole tendon (*Load target type*=”shape”), to a value of *P*. This value is positive, as it represents a tensile force.
  - The *Load type* is set to ”Post-tensioning load”, and the *tensioning type* is set to ”Both ends” so simulate a jacking process from both sides of the beam. The user also has the option to simulate a jacking from one side only. This will not affect the results, except that the deformation of the tendon will only be to one side while the other side is fixed.

– Finally, the two ends of the tendon are defined as the anchoring points.

– ”CEB-FIP Model Code 1990” is selected as the *Post-tensioning scheme*. As explained in chapter 3.2.2, the embedded reinforcement is not defined as finite elements. From the applied force at the anchors, $P$, the stress distribution in the tendon is computed based on the results from the finite element analysis, using the European CEB-FIB Model Code 1990 or the Korean Post-tensioning Scheme.[ [2] DIANA 9.4.4, 25.]

– Based on the recommendations in the DIANA manual, the *Coulomb friction coefficient* and the *wobble effect* can be chosen. These two parameters define the level of friction on the tendon and thereby the loss of prestress. The Coulomb friction coefficient defines the friction due to the curvature $\kappa$ of the tendon. The wobble effect takes into account the friction loss because of the local irregularities in the surrounding concrete.

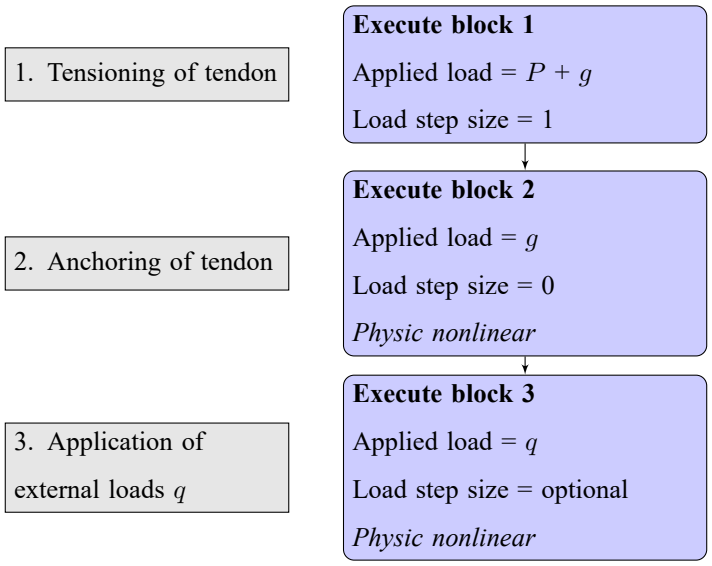


Figure 16: Flow chart showing the order of applied loads during an analysis with Embedded tendons

Figure 16 shows the order of the non-linear analysis when the embedded reinforcements are used. With execute blocks, the user may apply and remove the defined loads on the model in different stages of the analysis;

In **Execute block 1**, the load combination corresponding to the post-tensioning force $P$ and the self weight $g$ are applied to the model. The load step size is set to 1, which means the forces are added in one single step, using the preferred iteration method and number of iterations.

In **Execute block 2**, the termination of the jacking and the anchoring is simulated. Only the self weight is applied, with zero step size, as to remove the prestressing force $P$. By adding the *physic nonlinear* option to the execute block, the user can edit the properties of the tendon and set them to

”fully bonded reinforcement”. The *NOBOND* condition defined for the reinforcement material is then turned off.

Optionally, **Execute block 3** can be added so that the model can be loaded with external loads $q$.

## 4.2 Modelling and analysis with bond-slip reinforcements

Because of the differences between the embedded reinforcements and the bond-slip reinforcements, the model has to be defined in a slightly different manner;

- When defining the material for the prestressed reinforcement, the *material model* is set to ”bond-slip reinforcement”. Then, the Bond-slip interface option box appears and allows the user to define the material properties of the interface element, as described in Section 3.2.3. To model both the ungrouted situation during the tensioning phase and the grouted situation, it is necessary to define two materials for the prestressed reinforcement. The two materials will have different stiffness parameters representing the different levels of bond-slip. For the shear stiffness parameter $k_t$, the user can choose between a simple linear behaviour and a more complex non-linear behaviour such as the Dörr curve, whereas the normal stiffness parameter $k_n$ is always linear. Independently of which model is chosen, the stiffness parameters should be set very low to represent the ungrouted situation and high to represent a perfectly grouted concrete member.
- For the geometry definition of the prestressed reinforcement, the *Reinforcement type* is now set to ”truss bondslip”.
- A very important step is to define *element data* for the reinforcement bar, which ensures that the reinforcement bar is modelled as a finite element. Here, either *TRUSS* or *BEAM* is selected, depending on which type of element the user prefers.
- When defining the loads, the prestressing force $P$ acting on the bond-slip reinforcements is defined in a different manner than for embedded reinforcements;
  - The prestressing force $P$ is applied to the two nodes at the far ends of the tendon. The direction of the force should be applied so that the tendon is in tension.
  - Reaction forces $R$ of the same magnitude, but with opposite direction than the prestressing forces, has to be applied to the nodes of the concrete that overlaps with the ends of the tendon. This reaction force ensures that the concrete is not affected by the prestressing force.
  - For bond-slip reinforcements, the anchorage points where $P$ and $R$ are applied, have to be simulated by using *tyings*. Tyings define a connection point between two nodes of different elements, which creates a linear dependency between the degrees of freedom of the adjacent elements of the node[ [2]DIANA 9.4.4, 2.2]. For bond-slip reinforcements, the tyings equalize the degrees of freedom between the concrete and the reinforcement at the point of the anchorage. This means

that the edges of the concrete member will follow the deformations of the tendon in the second block.

In DIANA, an analysis with bond-slip reinforcements is performed using a concept called *Phased Analysis* [ [2]DIANA 9.5, *VII Phased Analysis*]. From one phase to another, the finite element model can be modified by adding or removing elements or constraints or changing the material properties. A phased analysis allows the user to simulate a phased construction and will give the results for different stages of the concrete members' history. In this case, the material conditions of the interface material will be changed between the two phases, and the tyings defined earlier will only be applied in the second phase. Each new phase will use the result from the previous phase as a starting point by default. However, any nodal displacement calculated from the previous point must be manually selected if it should serve as the initial position for the next phase. Otherwise, the analysis of the next phase will use the undeformed model as a starting point.

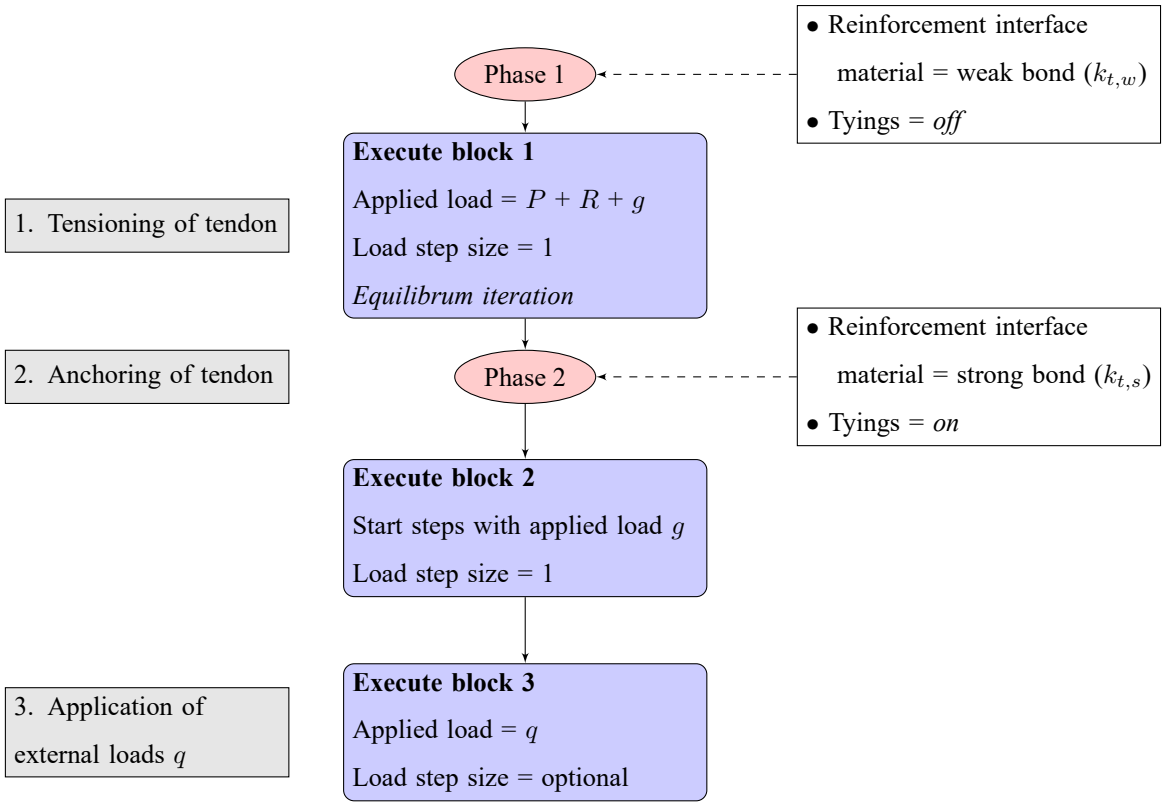


Figure 17: Flow chart showing the order of applied loads during an analysis with Bond-slip tendons

Figure 17 shows the consecutive execute blocks during a non-linear analysis with bond-slip reinforcements;

- In **Phase 1**, the reinforcement interface material with a weak shear stiffness parameter $k_{t,w}$ is defined to represent null bond conditions for the first phase. The tyings are also deactivated to produce a pre-strain in the tendons without affecting the concrete edges' positions.

- In **Execute block 1**, the prestressing load $P$, the reaction force $R$ and the self weight $g$ are added to the model to simulate the tensioning phase.
- In **Phase 2**, the stiffness parameter is changed to $k_{t,s}$ as to represent a grouted concrete member. The tyings are turned on to simulate the anchoring of the tendons.
- In **Execute block 2**, it is necessary to add *start steps* to specify which external loads from the previous phase that should be kept in the next case, which will be the self weight only, as the jacking force and the reaction force is removed.
- Optionally, **Execute block 3** can be added to load the model with service loads $q$.

By using the bond-slip reinforcements it is also possible to model an insufficiently grouted post-tensioned member. This can be done by changing the material properties of the reinforcement interface material.

| **Phase** | **Ungrouted tendons** | **Grouted tendons** |
|---|---|---|
| Jacking phase /tensioning phase | $k_{t,w}$ and $k_{n,w}$ | $k_{t,w}$ and $k_{n,w}$ |
| Loading phase | $k_{t,w}$ and $k_{n,w}$ | $k_{t,s}$ and $k_{n,s}$ |

Table 3: Stiffnesses of the bond-slip reinforcement interface material for grouted and ungrouted beams in the two phases of the analysis.

Table 3 shows how the material properties should be changed in order to model a fully grouted or completely ungrouted beam. In the first phase, the bonding must always be set to a very low stiffness parameter $k_w$ during the jacking phase. For ungrouted beams, this value is kept for the second phase of the analysis. For grouted beams, the stiffness parameter has to be changed to $k_s$ in the second phase to represent a bonded situation. It is also possible to split the reinforcement into different parts using the *split wire* command. The different parts can have different material properties assigned to them. Therefore, it is also possible to model a partly grouted reinforcement, where some areas are bonded to the concrete, while other areas are not.

# Part I

# Post-tensioned beams with lack of grouting

# 5 Presentation of reference experiments

Part I of this thesis describes how four-point bending tests on post-tensioned beams with different levels of grouting were modelled in DIANA. To ensure that the modelling and analysis procedures were representative and valid, three beams were made with the same geometry and loading procedure as in published experimental results. The numerical results and the experimental results are compared in the next chapter.

The reference experiments that were used have been found in the research papers described in the following sections.

## 5.1 RC Beam

”Flexural Behaviour of External Reinforced Concrete Beams” by Rudy Djamaluddin [23] was used as a reference for a non-linear analysis on an ordinary reinforced concrete beam. This experiment will be referred to as the **RC beam** hereafter. This beam was chosen as a starting point for the non-linear analysis as it is a simple case without the potential errors that may occur when the post-tensioning is included. The beam was used to gain experience on the most efficient material models and analysis procedures. It was attempted to match the numerical results to the experimental results before proceeding to study the post-tensioned beam cases. Figure 18 shows the load-deformation curve reported in the article. Here, only the ”Normal Beam” was modelled.

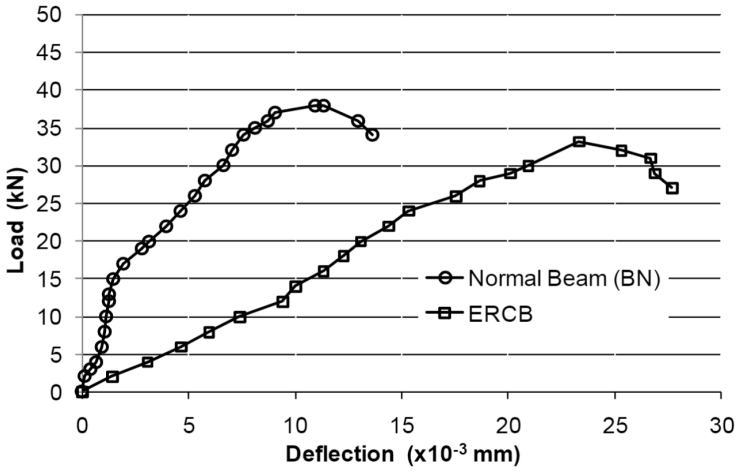


Figure 18: Load-deflection curve for the experimental results of the RC Beam. [23]

## 5.2 PT1 Beam

”Effect of insufficient grouting and strand corrosion on flexural behaviour of PC beams” by Lei Wang Et Al. [24] is an article that treats the non-linear response of beams with insufficient grouting, and the model from this article will hereby be referred to as **PT1**. The article indicates what could be the expected response of a post-tensioned concrete beam when there is a lack of grouting, and has therefore been an important reference for this thesis. In this experiment, five post-tensioned concrete beams with different levels of grouting were constructed;

**B1;** A fully grouted beam

**B2;** A beam with no grouting

**B3;** A beam with grouting in half the cross-section of the duct

**B4;** A beam with no grouting in half of the span

**B5;** A beam with no grouting in the central region of the duct

On each of the beams, a flexural bending test was performed. The load was applied monotonically until the final failure, and the load was measured by a load cell. It can be observed from Figure 19 that there is a noticeable difference in the response during the flexural bending of the five different beams.

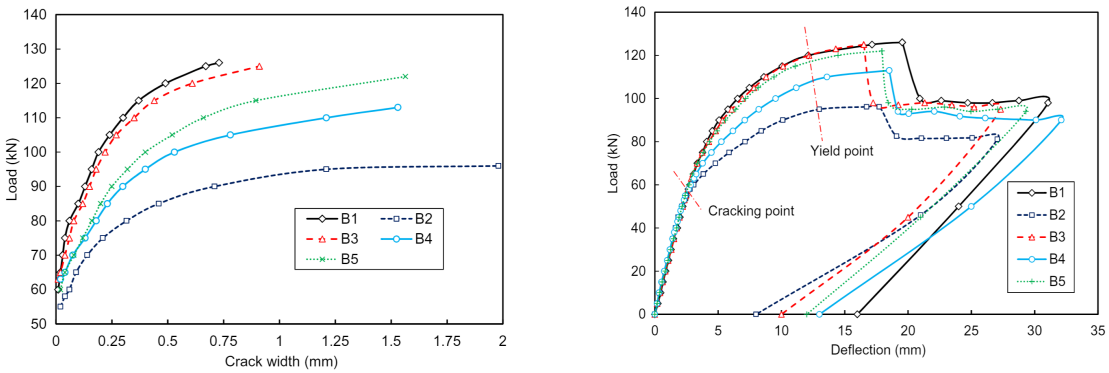


Figure 19: Load-crack width curves (left) and load-deflection curves (right) for the experimental results of the PT1 Beam. [24]

## 5.3 PT2 Beam

Because it was not managed to successfully recreate the load-deflection curve from the experiment, the PT2 beam was modelled as an alternative.

”Response of post-tensioned concrete beams with unbonded tendons including serviceability and ultimate limit state” by N.A. Vu Et Al. [25] is a flexural bending test performed on a prestressed concrete beam with unbonded tendons. This beam is referred to as **PT2** from this point on. Figure 20 shows the load-deflection curve from the experiment. Given that the beam was unbonded and the friction would be negligible, it was assumed to have similar behaviour as an ungrouted beam. To compare the results with PT1, it was decided to model a grouted model of PT2 as well.

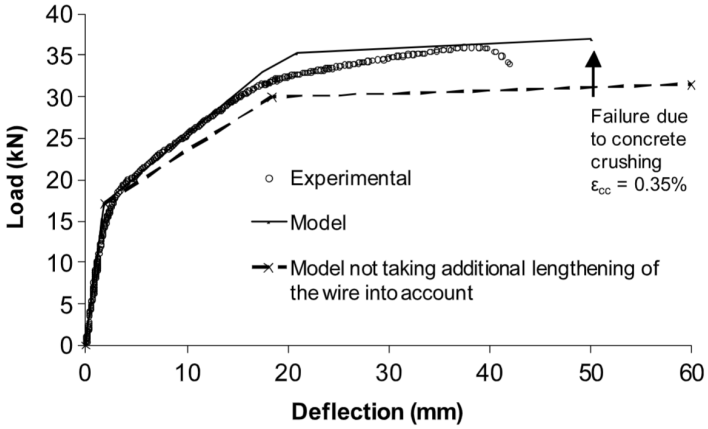


Figure 20: Load-deflection curve for the experimental results of the PT2 Beam. [25]

As the two experiments from PT1 and PT2 had a similar geometry and set-up, it was expected to see a similar tendency when comparing a grouted and ungrouted beam, as can be observed in Figure 19. Specifically, a considerably lower ultimate load capacity was expected when the beam was modelled as ungrouted, compared to a fully grouted beam. In addition, a noticeable difference in crack width was expected when comparing the two situations.

# 6 Modelling of a simple post-tensioned beam with insufficient grouting

This chapter contains the methodology for the modelling and analysis of the RC Beam, the PT1 Beam and the PT2 Beam. First, the general modelling method used for all three beams is described. In the following chapters, the geometry and specific properties of each beam model are presented. The relevant material models, finite elements and analysis methods mentioned in this chapter are presented and explained in Chapter 3 and 4. To study the effect of insufficiently grouted tendons, it was decided to start by modelling and comparing the extreme cases of no grouting and full grouting.

## 6.1 General modelling procedure and analysis scheme of the Beam models

As the beams have a simple rectangular cross-section, they were modelled in two dimensions, using plane stress finite elements. All the beam models are simply supported concrete beams, loaded with a load cell under monotonic loading. The load cell applies a gradually increasing downward load to the beam, as two point loads $F$.

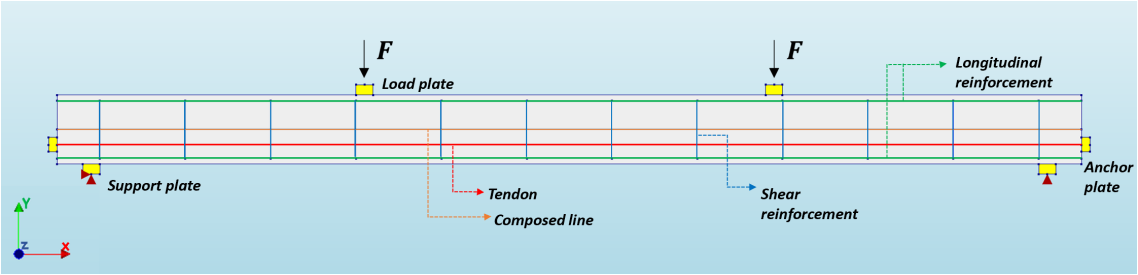


Figure 21: General set-up of the beam models in DIANA

A generic drawing of the DIANA model is presented in Figure 21. When defining the boundary conditions of the beams, the left support was restrained in both the $x$ and the $y$ direction (horizontally and vertically), while the right support was restrained only in the $y$ direction. At the points of support, steel plates and interfaces were modelled. Steel plates were also used to model load plates between the applied point loads $F$ and the upper edge of the beam and as anchor plates at the extremities of the tendon.

The longitudinal and shear reinforcements were modelled as embedded reinforcements and thereby a perfect bond between these reinforcements and the surrounding concrete was assumed. For the post-tensioned beam models PT1 and PT2, the tendons were modelled both with embedded reinforcements and with bond-slip reinforcements.

In all beam models, a composed line was included. The line is located in the centre of the cross-section and is only used for the post-processing of the results. The geometry of the composed line was set to cylindrical and the diameter was not defined. This means that the composed line has an infinite size and that all elements in the model will be included in the post-processing.

### 6.1.1 Material models

**Concrete**

When defining the properties for the concrete beam, the Element Class was set to *Regular Plane Stress*. The concrete material was defined with the properties stated below.

| | |
|---|---|
| Class; | *Concrete and masonry* |
| Material model; | *Total strain based crack model* |
| Crack orientation; | *Rotating* |
| Tensile curve; | *Exponential* |
| Crack bandwidth specification; | *Rots* |
| Poisson's ratio reduction model; | *No reduction* |
| Compression curve; | *Parabolic* |
| Reduction due to lateral cracking; | *Reduction model by Vecchio and Collins 1993* |
| Lower bound reduction curve | 0,6 |
| Stress confinement model | *No increase* |

**Reinforcement**

The passive reinforcements of the beam models, including the tendons, were defined as;

| | |
|---|---|
| Class; | *Reinforcements and pile foundations* |
| Material model; | *Von Mises Plasticity* |
| Hardening function; | *No hardening* |

**Steel plates**

The definition of the material defined for the steel plates is presented in Table 15. The table also includes the chosen geometry of the plates.

| | |
|---|---|
| **Support- and load plates** | |
| Length | 50 mm |
| Width | = *width* b *of beam* |
| Thickness | 30 mm |
| **Anchor plates** | |
| Height | 40 mm |
| Width | = *width* b *of beam* |
| Thickness | 25 mm |
| **Material properties** | |
| Class | *Steel* |
| Material model | *Linear elastic isotropic* |
| Elastic modulus | 210000 N/mm$^2$ |
| Poisson's ratio | 0,3 |
| Mass density | 0 |
| **Interface material properties** | |
| Class | *Interface elements* |
| Material model | *Nonlinear elasticity* |
| Type | *2D line interface* |
| Normal stiffness modulus-y | 34200 N/mm$^3$ |
| Shear stiffness modulus-x | 0,000342 N/mm$^3$ |
| No-tension or diagram | *No-tension with shear stiffness reduction* |
| Critical interface opening for reduction | 0,001 mm |
| Normal/shear stiffness reduction factor | 0 |

Table 4: Dimensions and material properties of the support plate

### 6.1.2 Numerical iterative procedures

The non-linear analyses for the beam models were executed with both the Newton-Raphson iteration method and the Secant iteration method. For the Newton Raphson analysis, the following settings were used;

- Maximum number of iterations; 25
- Method; *Newton-Raphson*
- Type; *Regular*
- First tangent; *Tangential*
- Line search; *off*
- Convergence norm;
  - Convergence criterion; *Energy*
  - Convergence tolerance; 0,005
  - Abort criterion; 10000
  - Reference; *set up new*
  - No convergnce; *Continue*

For the non-linear analyses with the Secant iteration method, the same settings as in the list above were used with a few exceptions; ”Method” was set to Secant(Quasi-Newton), ”Type” was set to *BFGS* and ”First tangent” was set to *Previous iteration*.

,

## 6.2 Modelling and analysis of the RC Beam

The ordinary concrete beam was modelled using the same geometry and material properties as the beam referred to as the ”Normal Beam” in the experimental flexural test [23]. In this experiment, the load was applied until failure, using hydraulic jacks with an incremental application of 1 kN per step. Simultaneously, the deflection at midspan was measured as well as the appearance of cracks. The geometry of the RC beam is presented in Figure 22 and Figure 23. The cover of the reinforcement was 30 mm. The materials were defined with the parameters stated in Table 5.

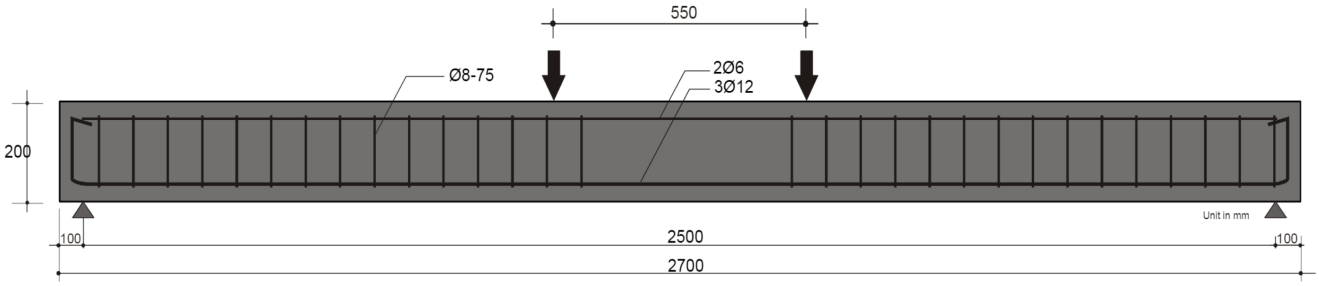


Figure 22: Geometry and load configuration of the RC beam. [23]
Measures are in mm.

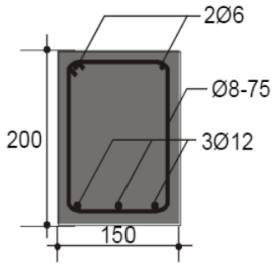


Figure 23: Cross-section of the RC Beam. [23]
Measures are in mm.

| **Material** | **Symbol** | **Magnitude** | **Unit** |
|---|---|---|---|
| **Concrete** | | | |
| Elastic modulus | $E_c$ | 24800 | N/mm$^2$ |
| Compressive strength | $f_{cc}$ | 26,3 | N/mm$^2$ |
| Tensile strength | $f_{ct}$ | 3,47 | N/mm$^2$ |
| Poisson ratio | $\upsilon_c$ | 0,2 | |
| Concrete weight | $\gamma_c$ | 2400 | kg/m$^3$ |
| **Ordinary reinforcement** | | | |
| Elastic modulus | $E_s$ | 210000 | N/mm$^2$ |
| Yield strength | $f_y$ | 410 | N/mm$^2$ |

Table 5: Material properties of the RC beam

Q8MEM elements were used, with a defined maximum size of 20 mm. The non-linear analysis of the RC-beam was performed using two execute blocks. In the first block, the self weight $g$ is applied. In the second block, the external point loads $2F$ were applied by using load steps so that they were gradually increasing. Figure 24 shows how the execute block was defined.

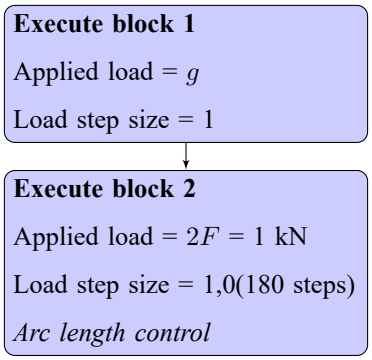


Figure 24: Flow chart showing the order of the non-linear analysis of the RC beam model with embedded tendons

## 6.3 Modelling and analysis of the PT1 Beam

Similarly to the RC Beam, the PT1 beam was subjected to two point loads applied symmetrically about midspan until the beam reached failure. The geometry and position of the reinforcements are given in Figure 25, while the position of the point loads and the supports are presented in Figure 26. Figure 27 shows a cross-sectional view of the beam.

Regarding the passive reinforcement, the longitudinal reinforcements were two plain HPB235 bars with 8 mm diameter at the bottom and two deformed HRB335 bars with 12 mm diameter at the top. It should be noted that the covers of the passive reinforcement were not stated in the article. In the model, these were assumed to be 45 mm by measuring the figures. The material properties of the stirrups are not stated in the article, but were given the same yield strength as the bottom reinforcement, $f_y$= 235 N/mm$^2$. A prestressing strand with a diameter of 15.2 mm consisting of seven wires was placed in a 32 mm duct 60 mm over the bottom of the beam as shown in Figure 27. The article states that *"The initial strength of prestressing strand is 1395 MPa, i.e. 0.75 times of the ultimate strength"* [24]. The magnitude of the post-tensioning force $P$ is not mentioned anywhere else in the article. It was therefore assumed that the the applied prestressing force to the tendons was

$$P = \sigma \cdot A_p = 1395 \text{ MPa} \cdot \pi \cdot \frac{(15,2 \text{ mm})^2}{4} = 253134 \text{ N}$$

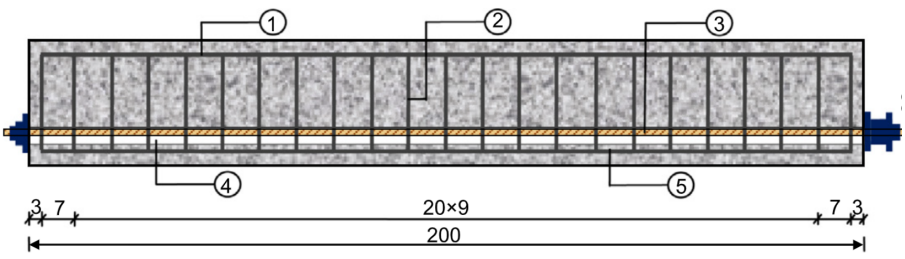


Figure 25: Geometry and reinforcements of the PT1 Beam [24]
Measurements are in cm.

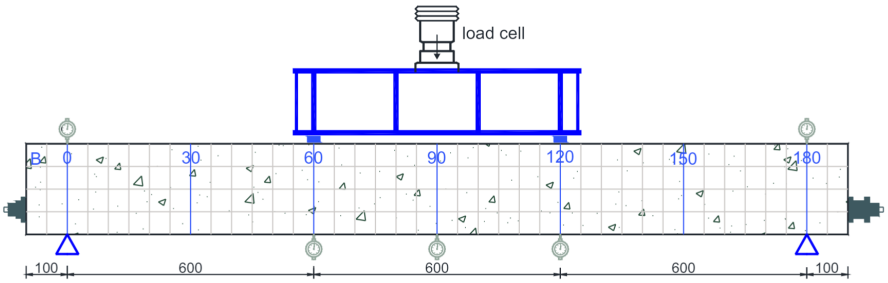


Figure 26: Load application and position of supports for the PT1 Beam [24]
Measurements are in mm.

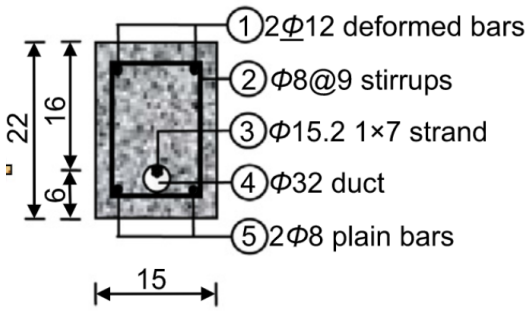


Figure 27: Cross-section of the PT1 Beam [24]
Measurements are in cm.

| Material | Symbol | Magnitude | Unit |
|---|---|---|---|
| **Concrete** | | | |
| Elastic modulus | $E_c$ | 31793 * | N/mm$^2$ |
| Compression strength | $f_{cc}$ | 34,12 | N/mm$^2$ |
| Tensile strength | $f_{ct}$ | 2,64 * | N/mm$^2$ |
| Poisson ratio | $\upsilon_c$ | 0,2 | |
| Concrete weight | $\gamma_c$ | 2400 | kg/m$^3$ |
| **Ordinary reinforcement** | | | |
| Elastic modulus | $E_s$ | 210000 | N/mm$^2$ |
| Yield strength | $f_y$ | 235/335 ** | N/mm$^2$ |
| **Prestressed tendon** | | | |
| Elastic modulus | $E_p$ | 195000 | N/mm$^2$ |
| Yield strength | $f_{p0,1}$ | 1830 | N/mm$^2$ |

Table 6: Material properties of the Prestressed beam 1
* Not stated in article, calculated in Section A of the Appendix based on $f_{cc}$
** Strength for bottom and top ordinary reinforcement, respectively

The mesh was assigned to the PT1 model using Q8MEM elements with a maximum size of 10 mm. The behaviour of the fully grouted beam, referred to as *B1* in the article, was then attempted to be recreated

by using both embedded reinforcements and bond-slip reinforcements to model the tendon. The difference between these two methods is explained in 4.1 and 4.2. The two analysis types are presented in the flow charts in Figure 28 and Figure 29.

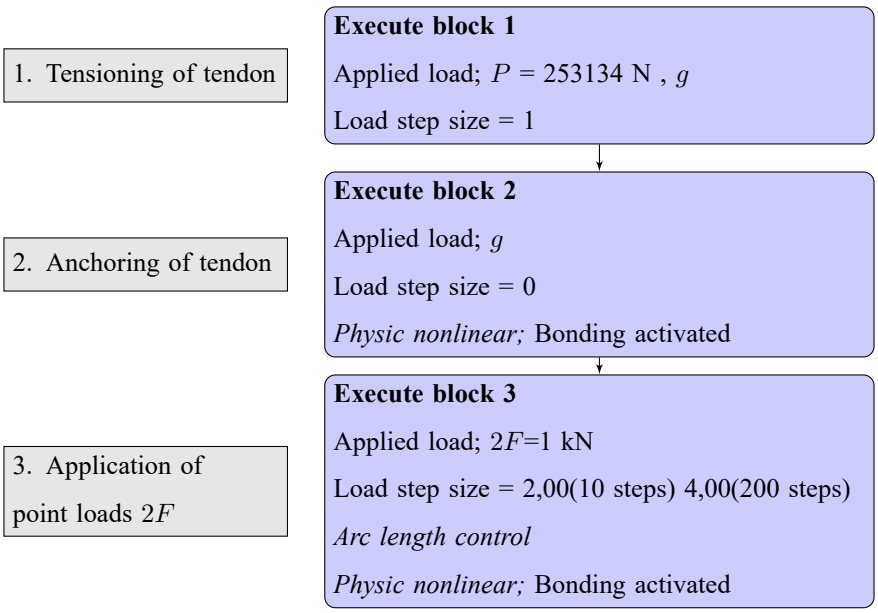


Figure 28: Flow chart showing the order of applied loads for PT1 during an analysis with embedded tendons

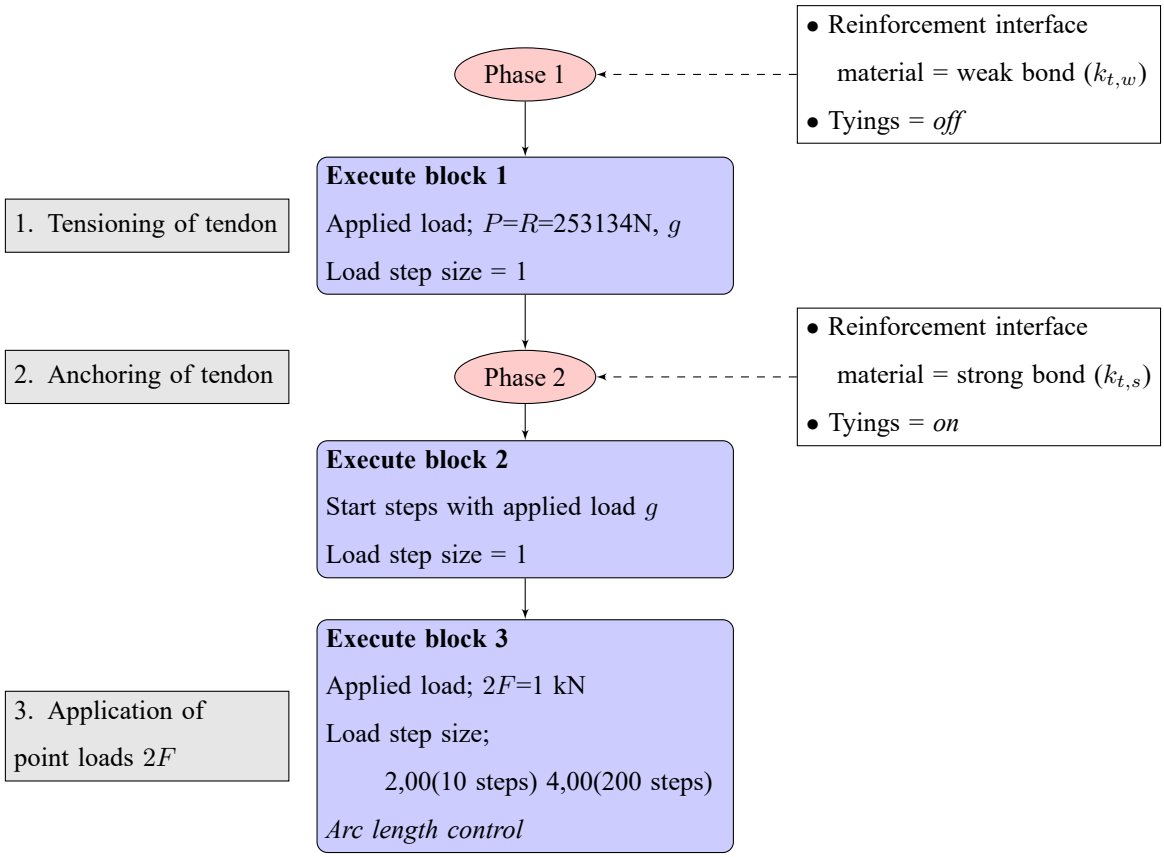


Figure 29: Flow chart showing the order of applied loads during an analysis with bond-slip tendons

## 6.4 Modelling and analysis of PT2

The PT2 model is based on an experimental study by Vu Et Al. [25] that treats the behaviour of unbonded post-tensioned prestressed beams subjected to four-point bending tests. The study investigates both monotonically increasing loading and repeated loading cycles, where only the former was attempted to be recreated in this thesis. The geometry definition and position of the reinforcement is presented in Figure 30 and Figure 31, while Figure 32 shows the position of the applied load $2F$ and the support plates.

The tendon is reported as an 8 mm wire with an applied tensioning force $P$ = 54 kN. This leads to a stress equal to 80% of the yield stress. The material properties of the beam are presented in Table 7.

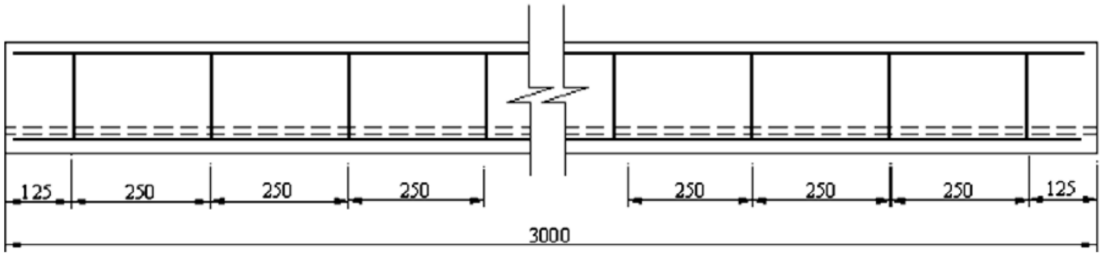


Figure 30: Geometry and reinforcements of the PT2 Beam [25]
Measurements are in mm.

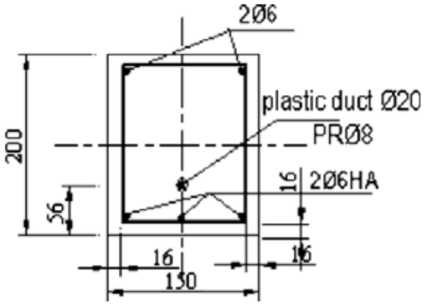


Figure 31: Cross-section of the PT2 [25]
Measurements are in mm.

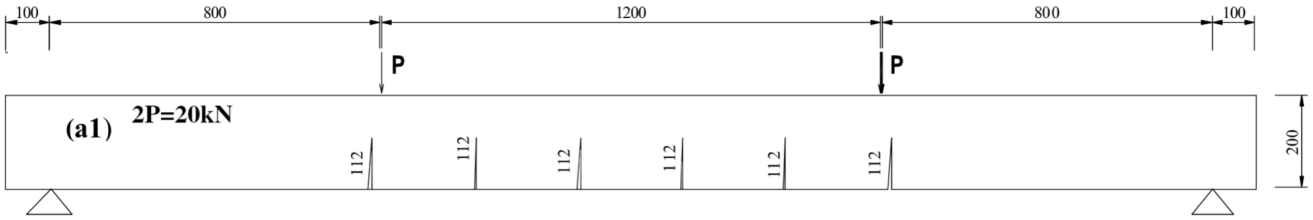


Figure 32: Position of the applied point loads and the supports and crack patterns. [25]
Measurements are in mm.

| Material | Symbol | Magnitude | Unit |
|---|---|---|---|
| **Concrete** | | | |
| Elastic modulus | $E_c$ | 30000 | N/mm$^2$ |
| Compression strength | $f_{cc}$ | 45 | N/mm$^2$ |
| Tensile strength | $f_{ct}$ | 2,9 | N/mm$^2$ |
| Poisson ratio | $\upsilon_c$ | 0,2 | |
| Concrete weight | $\gamma_c$ | 2400 | kg/m$^3$ |
| **Ordinary reinforcement** | | | |
| Elastic modulus | $E_s$ | 200000 | N/mm$^2$ |
| Yield strength | $f_y$ | 400 | N/mm$^2$ |
| **Prestressed tendon** | | | |
| Elastic modulus | $E_p$ | 210000 | N/mm$^2$ |
| Yield strength | $f_{p0,1}$ | 1300 | N/mm$^2$ |

Table 7: Material properties of PT2

Similarly to the PT1 beam, the maximum element size was defined as 10 mm, using Q8MEM elements. Figure 33 shows the set-up of the analysis using embedded reinforcements for the tendons, whereas Figure 34 shows the analysis when bond-slip reinforcements were used.

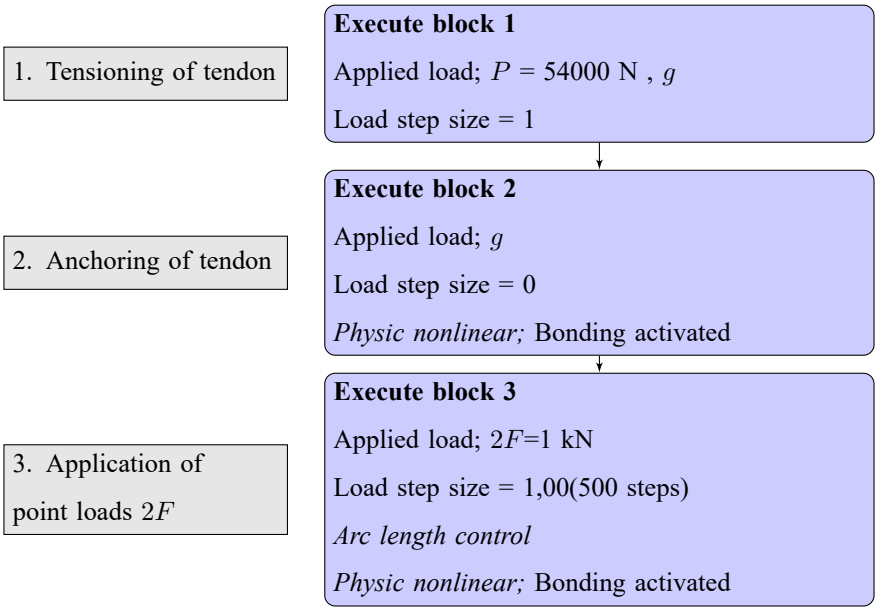


Figure 33: Flow chart showing the order of applied loads for PT2 during an analysis with embedded tendons

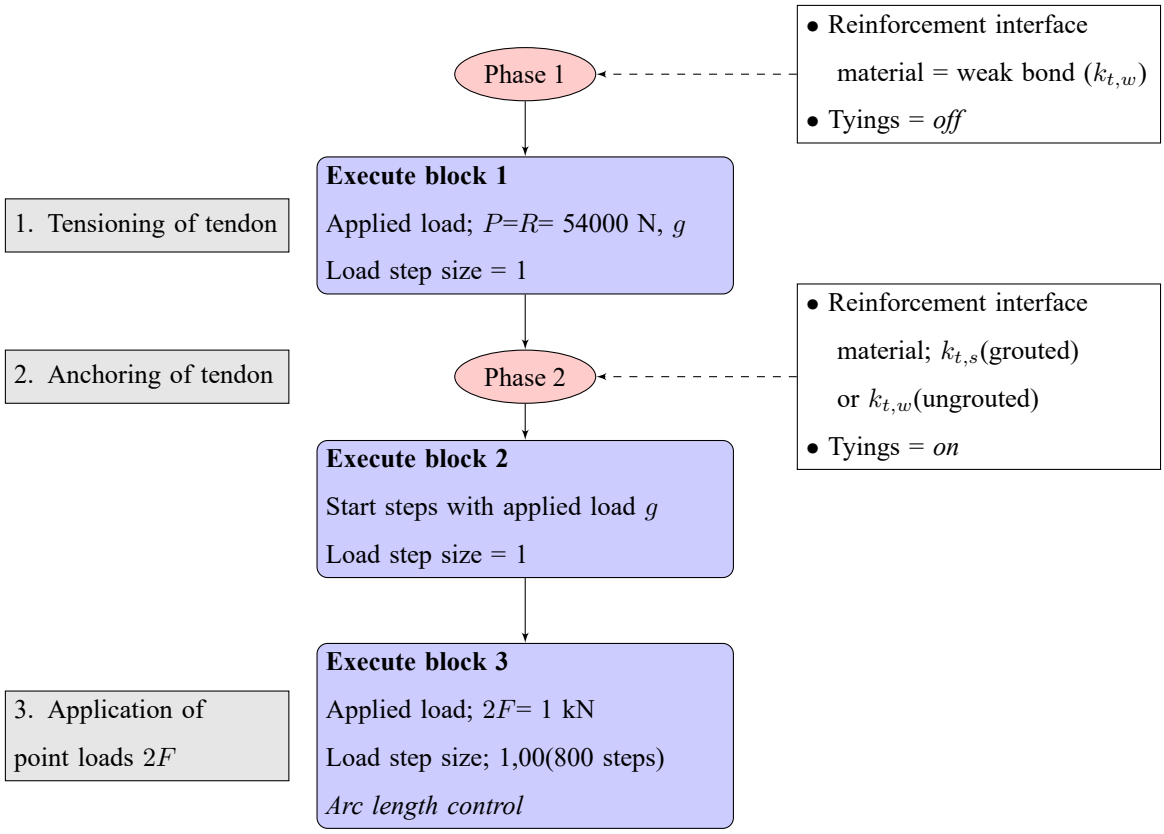


Figure 34: Flow chart showing the order of applied loads during an analysis of PT2, with tendons defined as bond-slip reinforcements

# 7 Results and discussion for beam models

## 7.1 Results from the RC Beam

The resulting load-deflection curve from the non-linear analysis of the RC beam is presented in Figure 35 and Table 8. The numerical results show a good agreement with both the analytical calculations and the experiment for the linear behaviour and the point of cracking. The point of cracking is registered in DIANA even for very small crack widths. Figure 36 shows the crack widths at load-step 9, which is the point where the first cracks are registered. As expected, the cracks appear at the midspan on the bottom edge of the beam, where the tensile forces are highest. The largest cracks at this stage have a width of only $1 \cdot 10^{-4}$ mm, so the reason why the point of cracking is reported later in the experiment might be that the cracks were not big enough to be detected.

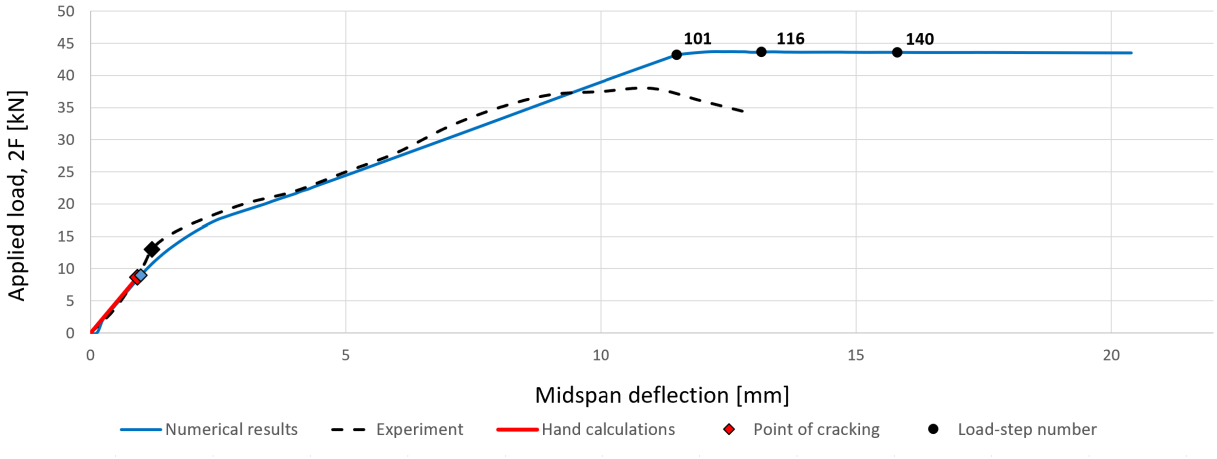


Figure 35: Load-deflection curve for the RC beam, compared to the experimental results and the analytical calculations

| | Numerical results | Experimental results | Analytical calculations |
|---|---|---|---|
| Cracking load $2F_{cr}$ [kN] | 8,9 | 13,0 | 7,5 |
| Corresponding midspan deflection [mm] | 0,98 | 1,2 | 0,92 |
| Ultimate load capacity $2F_{Rd}$ [kN] | 44,5 | 38,0 | 39,5 |

Table 8: Results for the RC beam. The point of cracking and the ultimate load capacity found in the numerical analysis, compared to the experimental results and the analytical calculations.

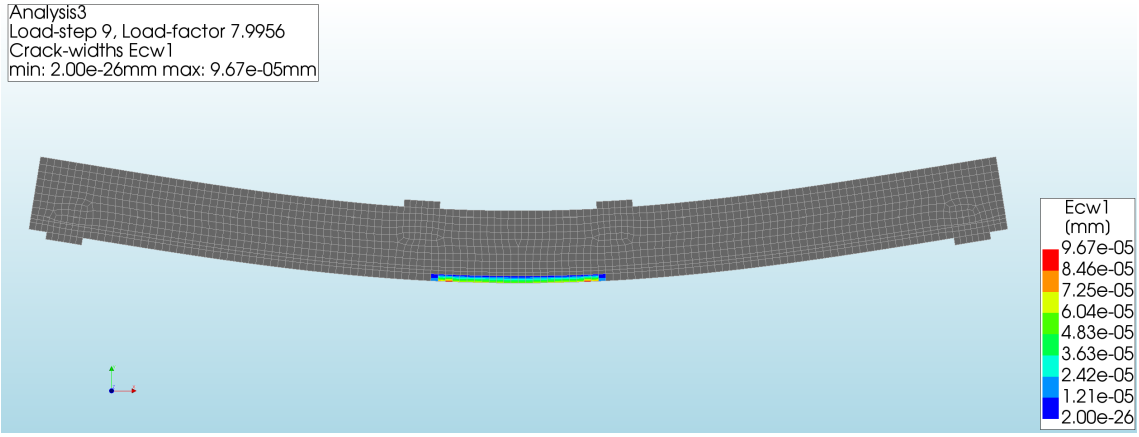


Figure 36: Cracking point for the RC beam at load step 9, The applied load, $2F$, is 8,9 kN, and the deflection at midspan is 0,98 mm.

After the beam has reached the non-linear behaviour, there seems to be a good agreement between the numerical and the experimental results. When the applied load reaches 38 kN, the beam in the experiment reached failure, as can be read in the reference [23]; *"When the applied load on normal beam reached to approximately 38 kN, then the tensile reinforcement entered into plastic range. The yielding of tensile reinforcement was followed by the crushing of the compression concrete. This affects to the decreasing of the flexural capacity of the beam."* In DIANA, the modelled beam had a higher capacity and withheld a maximum applied load of $2F$ = 44,5 kN, which is 12,7 % bigger than in the analytical calculations. As seen in Figure 37, the tensile reinforcement begins to yield($f_y$ = 410 N/mm$^2$) at load step 101, where the beam is loaded with $2F$ = 43,2 kN. After this point, the load-deformation curve flattens and becomes almost horizontal. Figure 37 also shows the crack distribution at this point, which is similar to the crack patterns reported in the reference, as presented in Figure 38. The maximum crack width at this point is 0,28 mm.

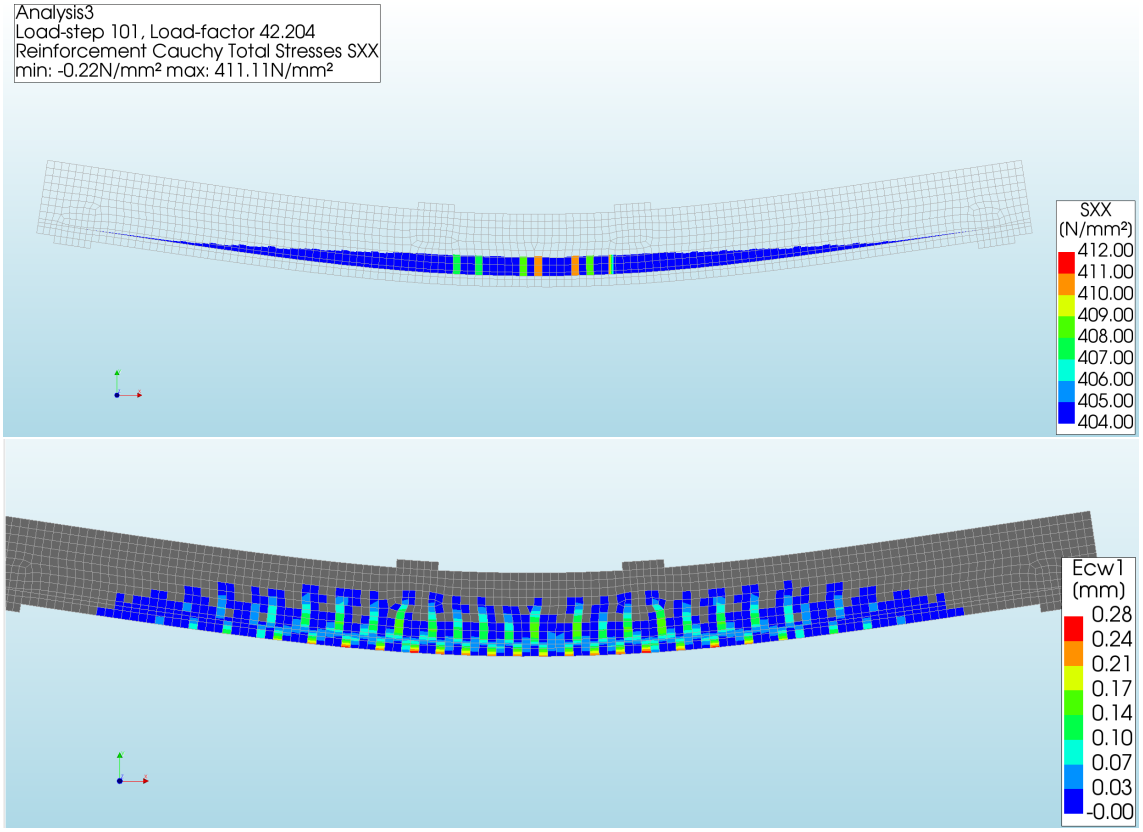


Figure 37: Point of yielding for the RC beam at load-step 101. The first picture shows the tensile stresses $\sigma_x$ in the tensile reinforcement, while the second shows the crack widths and crack distributions.

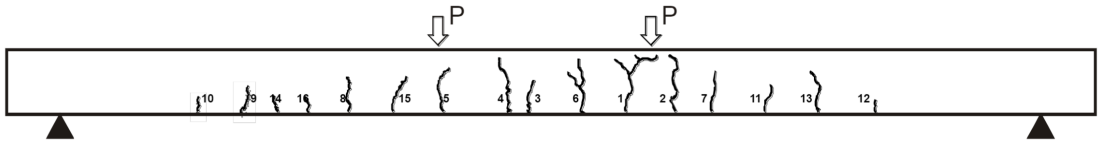


Figure 38: Crack pattern as reported in the reference research article. [23]

At load-step 116, the applied load $2F$ has increased to 43,6 kN. The top fibres of concrete reach the concrete compressive capacity of $f_{cc}$=26,3 N/mm$^2$, and will therefore cause the concrete to crush at this point. The concrete stress levels in the x-direction are shown in Figure 39. Note that the minimum and maximum stress levels stated in the upper left box also include the stresses appearing on the steel plates, which can be neglected.

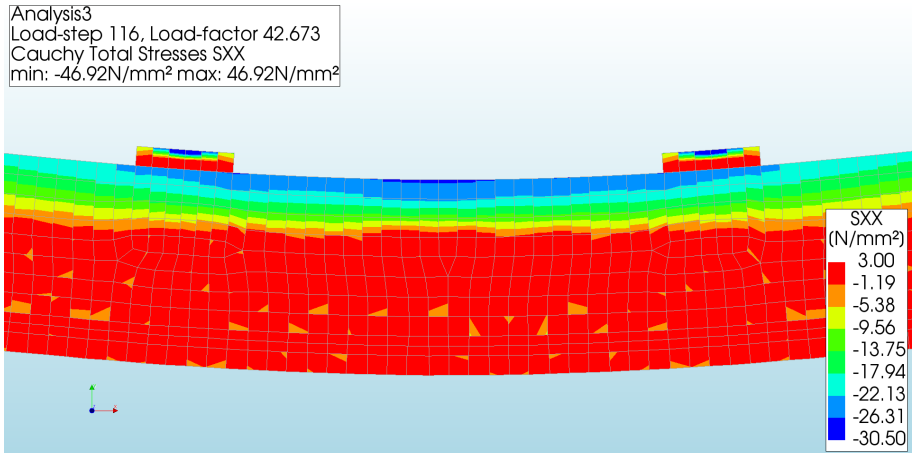


Figure 39: Point of failure of the RC beam at load-step 116. Cauchy total stresses in the x direction.

After the crushing of the concrete, the analysis did not detect any failure of the beam, which would normally be registered as a sudden drop in the load-deflection curve, followed by an automatic termination of the analysis. Instead, the analysis continued, with a constant applied load $2F$ while the deflections were still increasing, until the demanded number of load-steps were performed. A further inspection of the model for the horizontal part of the load-deflection curve, shows that a larger amount of the tensile reinforcement will yield for each load step. However, the maximum stress does not exceed the yield stress of 410 N/mm$^2$, because no hardening or ultimate capacity of the reinforcement was defined in the reinforcement material model. This can explain why the analysis seems to continue infinitely instead of registering a failure of the beam when it starts to crush. In addition, a large crack appears at the midspan of the beam after the point of crushing, with an increasing crack width. Figure 40 shows the crack widths at load-step 140 of the analysis. The magnitude of this crack is now 1,72 mm, which should imply that the beam would have failed at this point. Therefore, it can be assumed that this part of the analysis is no longer valid and can be neglected.

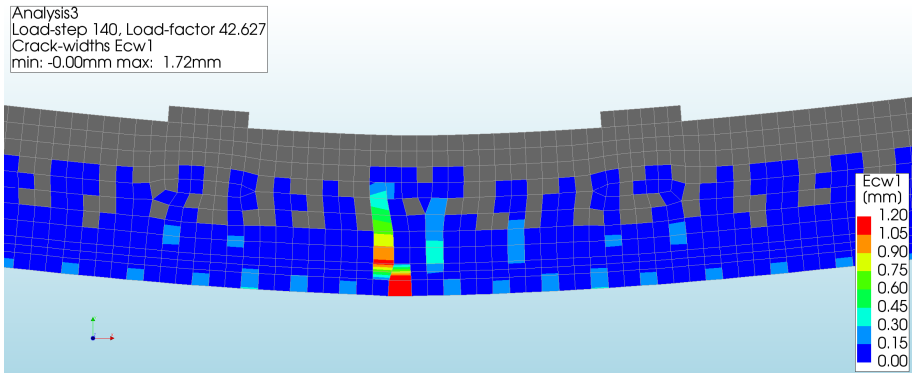


Figure 40: Crack widths of the RC beam at load-step 140.

An important assumption that was made for the interpretation of the results presented in the reference of the experiment was that the order of magnitude for the midspan deflection is wrongly reported in the article. In one diagram ( [23] Figure 7), the results are given in millimetres with a cracking deflection of 12 mm and a

maximum deflection of about 120 mm. However, these results seem to be almost exactly ten times bigger than the deformations found numerically and analytically. Therefore, a cracking deflection of 1,2 mm and a maximum deflection of 12 mm was assumed when plotting Figure 35.

Finally, it may be concluded that the DIANA analysis gave satisfactory results for the RC Beam. During the linear behaviour in Stage I, the numerical results are very precise. When approaching the ultimate load capacity, the model had a capacity that is 17,1% larger than the experimental results, and 12,7% larger than the analytical calculations. This may be due to the fact that the finite element method is not exact, and some differences between the numerical outputs and the analytical calculations are to be expected. A further refining of the mesh, especially at the points with large stress concentrations, might have given a more accurate result, but this was not attempted due to the limited time scope. It may also be noted that the DIANA manual's own verification report [26] provides some examples of numerical results of non-linear analyses compared to experiments, and even here, there are noticeable differences when the results are compared.

## 7.2 Results from PT1

Figure 41 shows the load-deflection curves for a selection of DIANA models together with the reported behaviour of the flexural bending test of the experiment. The analytical calculations for the behaviour of the beam in Stage I are also included in the figure. These can be found in Section D of the Appendix. All of the results are representing a perfect bond between the tendon and the concrete, and therefore a fully grouted situation. Four different DIANA models are included, using both the Dörr bond-slip model and embedded reinforcements. The iterations were performed using both the Newton-Raphson method and the Secant method. The results at the point of cracking and the ultimate load capacity in the three cases are presented in Table 9.

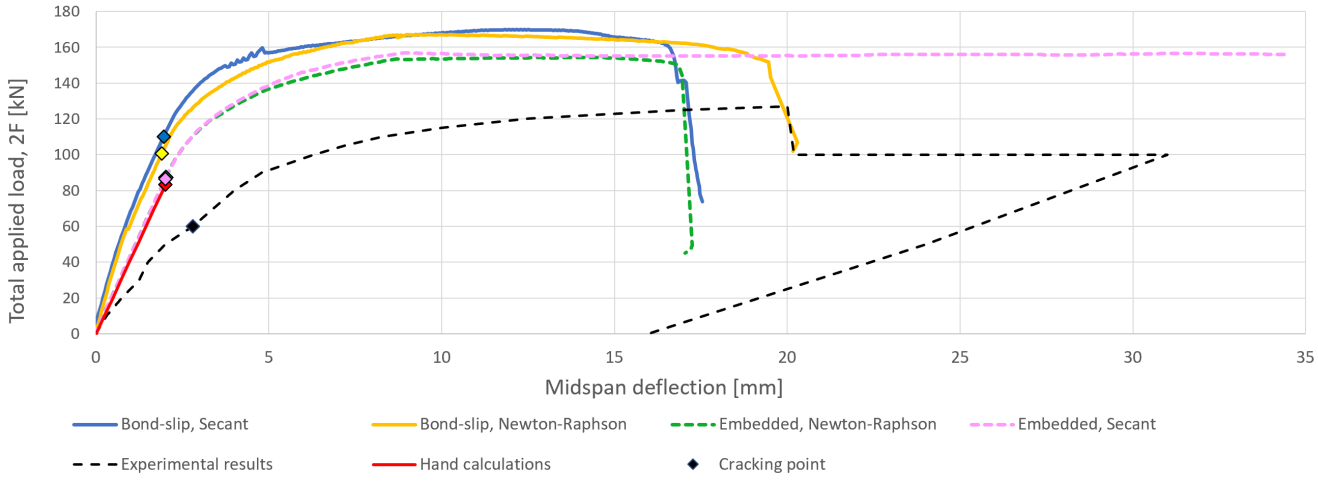


Figure 41: Load-deflection curve for the PT1 beam, compared to the experimental results and the hand calculations.

| | Numerical results | Experimental results | Analytical calculations |
|---|---|---|---|
| Cracking load $2F_{cr}$ [kN] | 86,4 - 110,0 | 60,0 | 83,2 |
| Corresponding midspan deflection [mm] | 1,9 - 2,0 | 2,8 | 2,0 |
| Ultimate load capacity $2F_{Rd}$ [kN] | 154,2 - 169,8 | 127 | 194,6 |

Table 9: Post-tensioned beam 1; The point of cracking and the ultimate load capacity found in the numerical analysis, compared to the experimental results and the analytical calculations.

The results that were found using DIANA are agreeing well with the results that are found with analytical calculations for the initial linear behaviour of the beam until the cracking point. As for the ultimate load capacity, the analytical calculations give a higher capacity than what is found with DIANA; The reduction compared to the analytical results are between 12,7% and 20,8%, depending on which bond-slip model and which analysis type that is used.

Neither the numerical results nor the analytical results were close to the experimental values. The load-deflection curve in Figure 41 shows that the beam used in the experiment had a considerably less stiff behaviour than what was managed to be recreated in DIANA and that the cracking load was 31 - 45% lower than expected. The ultimate load capacity found in the experiment was also about 18 - 25% lower than the DIANA outputs. The embedded model using the Secant method gave the same issue as for the RC beam

results; the beam seems to never reach failure, and the deformation keeps increasing for a constant applied load, giving a horizontal curve.

During the initial linear behaviour of the beam, the results using a finite element model are expected to be quite accurate. Therefore, none of the results from the DIANA analyses were satisfactory. To aim for a result that was closer to the experiment, the beam was re-modelled several times and controlled by two employees of the Department of Structural Engineering at NTNU. The material models presented in Chapter 6.3 were changed to investigate whether they gave a response closer to that of the experiment, particularly for the initial linear behaviour. For instance, the concrete stiffness $E_c$ was reduced by 20 %. Unfortunately, this did not give any considerable improvement.

As the DIANA models seem to agree quite well with the analytical results, this suggests that the PT1 beam model is appropriately modelled. Therefore, it was assumed that the information provided in the experimental report is either incomplete or invalid, or that the reported geometry, the material parameters, the experimental set-up or the presented results have been incorrectly interpreted when the DIANA model was created. Therefore, it was decided not to use this beam model to proceed with the investigation of the bond-slip modelling.

Nevertheless, the work with PT1 was a learning experience that was used in further work with PT2. In particular, it was experienced how the choice of iteration method affected the result, as well as the chosen bond-slip model. This is further elaborated in Section F of the Appendix.

## 7.3 Results from PT2

The post-tensioned beam PT2 was modelled in a similar manner as the PT1, and gave results that were much closer to the experimental results from the reference. The PT2 model was therefore used in a further investigation of the bond-slip reinforcement modelling by performing a parametric study of the reinforcement interface elements. As described in Section F of the Appendix, it was experienced that the linear bond-slip model gave more stable and reliable results than the Dörr bond-slip model. Also, the Newton-Raphson iterations gave better results than the Secant iterations. Furthermore, a study of the importance of load step size and the effect of the arc length control, presented in Section G of the Appendix, was performed. It was then decided to perform the analyses for PT2 with Linear interface elements and with Newton-Raphson iterations. The most appropriate shear stiffness parameters from the parametric study were then used to compare the results for a fully grouted and an ungrouted beam.

### 7.3.1 Parametric study of linear stiffness parameters

In the case of PT2, the only parameter that affects the bond-slip is the shear stiffness $k_t$, as it has a straight tendon. This parameter defines the level of bonding between the reinforcement and the surrounding concrete. It must be found both for a weak shear stiffness $k_{t,w}$, and a stiff shear stiffness $k_{t,s}$. During the jacking phase, $k_{t,w}$ is applied to allow a free elongation of the tendon. For the grouted beam, the shear stiffness is changed to $k_{t,s}$ to represent the presence of the grout. For the ungrouted beam, $k_{t,w}$ is kept during the loading phase. It was decided that a model with weak stiffness parameters could be compared to the experimental results as it was reported as an unbonded beam. A model with stiff stiffness parameters could be compared to an embedded model representing a fully grouted PT2 beam.

| **Phase** | **Ungrouted tendons** | **Grouted tendons** |
|---|---|---|
| Tensioning phase | $k_{t,w}$ | $k_{t,w}$ |
| Loading phase | $k_{t,w}$ | $k_{t,s}$ |

Table 10: Overview of the choice of shear stiffness parameters for the ungrouted and the grouted beam, during the two phases of the analysis.

As presented in Table 10, by first modelling an ungrouted tendon with a constant weak shear stiffness $k_{t,w}$, this parameter can be calibrated correctly before proceeding to the grouted model, which includes $k_{t,s}$ as well. To represent a very low bonding, the value for the interface shear stiffness should be as low as possible to minimize the level of bonding. However, it was discovered that the values could not be set too low because this will cause an incorrect behaviour of the ungrouted beam.

Figure 42 shows the load-deflection curves for the ungrouted tendons, using different values for $k_{t,w}$. This plot indicates that the value of $k_{t,w}$ will not affect the linear behaviour in the first part of the load-deflection curve. The peaks that can be observed for when the displacements are about 3-5 mm, indicate the first point of yielding for the tendons. The applied load at this point depends on which value for $k_{t,w}$ that is defined;

the highest value of $k_{t,w}$ = 1,0 N/mm$^3$ reached the yielding point at $2F$ = 20,0 kN, while $k_{t,w}$ = 0,05 N/mm$^3$ reached the yielding point at $2F$ = 30,0 kN. However, the difference in capacity is reduced as the deflection increases, and all four models seemed to have a final ultimate capacity $2F_{Rd}$ of between 31 and 32,5 kN. It was also found that a value of $k_{t,w}$ lower than 0,1 N/mm$^3$ diverged and terminated the analysis before the concrete reached the compressive capacity. For instance, $k_{t,w}$=0,05 N/mm$^3$ diverged for a midspan deflection of 28,1 mm. $k_{t,w}$ should therefore not be set lower than 0,1 N/mm$^3$ for this model.

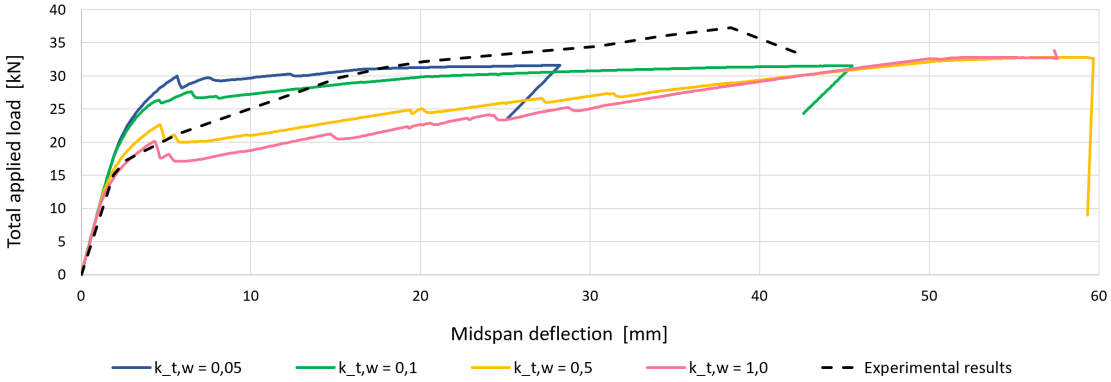


Figure 42: Load -deflection curves for unbonded PT2 models, by changing the value of $k_{t,w}$. (Units of $k_{t,w}$ are in N/mm$^3$)

The most important reason for the difference in the behaviour of the beams when $k_{t,w}$ is changed, can be found by examining the post-tensioning force along the tendon. According to Sørensen [6], the immediate friction losses for a straight tendon are negligible. Therefore, a constant post-tensioning force $P_x$ along the tendon after jacking is to be expected. However, the choice of $k_{t,w}$ seems to significantly influence the level of friction loss, as presented in Table 11. If $k_{t,w}$ is set too high, the shear forces developing at the reinforcement interface elements will be too large and will prevent the unrestrained elongation of the tendon, which is desired during the jacking phase. The considerable friction losses that appear for the highest values of $k_{t,w}$ can explain why the beam has a lower capacity when it is loaded, as seen in Figure 42; The friction losses during the tensioning phase limit the upward deflection after jacking, and thereby the intended effect of the prestressing is not achieved. According to the analytical calculations, which can be found in Section E of the Appendix, the upward deflection should be about 0,55 mm after the jacking phase.

| | **Analytical calculations** | **Numerical results (DIANA)** | | | |
|---|---|---|---|---|---|
| | | $k_{t,w}$ = 0,05 | $k_{t,w}$ = 0,1 | $k_{t,w}$ = 0,5 | $k_{t,w}$ = 1,0 |
| Post-tensioning force $P_x$ at midspan [kN] | ≈ 54,0 | 47,10 | 41,60 | 19,30 | 9,86 |
| Loss of post-tensioning force at midspan | ≈ 0 % | 12,8 % | 23,0 % | 64,3 % | 81,7 % |
| Upward deflection after jacking [mm] | -0,55 | -0,48 | -0,41 | -0,14 | -0,022 |
| Bending moment after jacking($M_p - M_g$) [kNm] | 1,70 | 1,31* | 1,08* | 0,15* | -0,24* |
| Cracking load $F_{cr}$ [kN] | 16,3 | 21,2 | 22,3 | 26,2 | 29,6 |

Table 11: Post-tensioned beam 2; Numerical results compared to analytical calculations for unbonded tendons, $k_{t,w}$ in both phases.(Units of $k_{t,w}$ are in N/mm$^3$)
* Bending moment of cross-section at mid-span

Figure 43 shows the results for the model with an interface shear stiffness of $k_{t,w}$= 0,1 N/mm$^3$. The first plot shows how the post-tensioning force $P_x$ is reduced from the initial value of $P_0$= 54,0 kN. Near the anchorages, the reduction is only about 0,1 kN, but at the midspan, $P_x$ is reduced with 23 %, to 41,6 kN. The second plot shows that the maximum upward deflection is 0,41 mm.

The moment diagram presented in the third plot of Figure 43 is calculated using the composed line. Correspondingly to the reduced prestressing force $P_x$ towards the centre of the beam, the bending moment $M_p = P \cdot e$ is also reduced at the mid-span. As the composed line calculates the moment by including all stress-contributions at the cross-section, the elements of the support- and load plates are also included. This explains the inconsistencies of the moment diagram at the position of these plates.

This first part of the shear stiffness calibration indicated that $k_{t,w}$=0,1 N/mm$^3$ gave the best results. A further reduction of the parameter gave a too early divergence of the analysis, and a higher value of $k_{t,w}$ gave too high values for the friction losses, and therefore a reduced capacity of the unbonded beam.

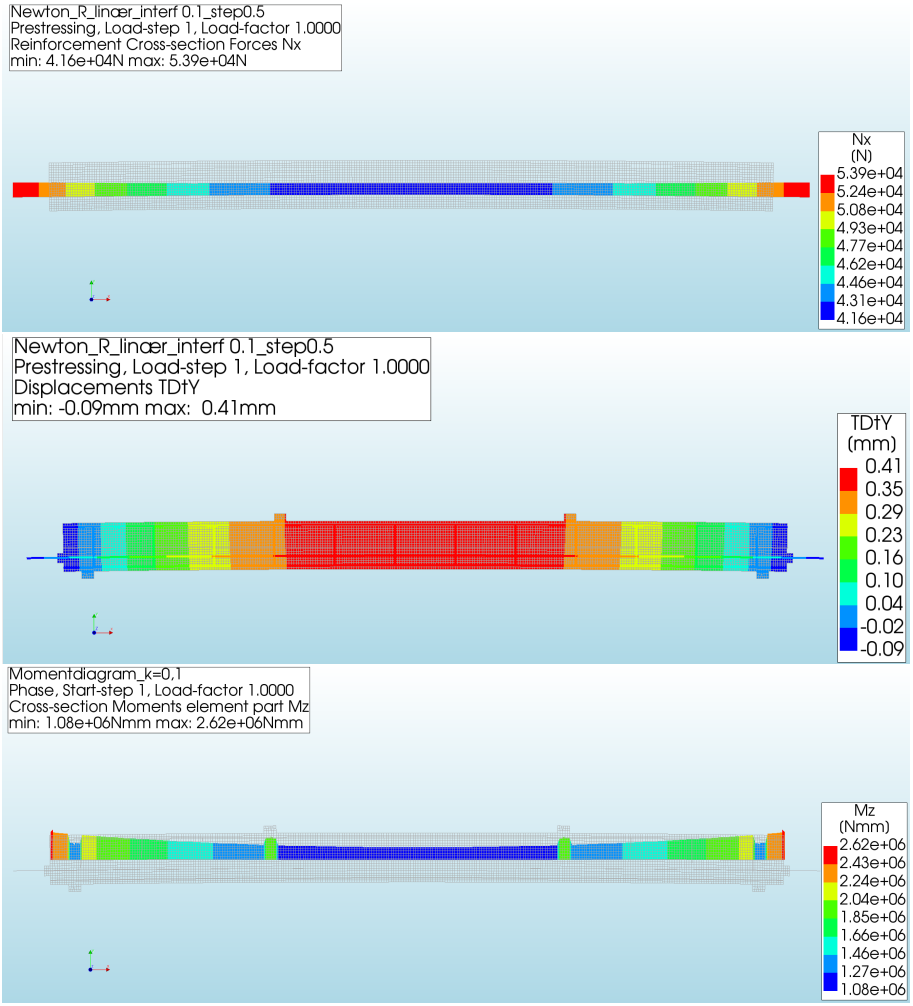


Figure 43: Results for the PT2 beam after the jacking phase, using unbonded properties for the reinforcement interface elements.

1. Reinforcement cross-section forces along the tendon
2. Nodal vertical displacements

3.Moment diagram for bending about the z-direction(perpendicular to plane), $M_z$

To proceed, new analyses were performed with a high value of $k_{t,s}$ for the loading phase, representing a fully grouted tendon. The values that are recommended by DIANA for the shear stiffness $k_{t,s}$ are between $1{\cdot}10^4$ N/mm$^3$ and $1{\cdot}10^6$ N/mm$^3$, as described in Section H.1 of the Appendix. Figure 44 shows the load-deflection curves for models with different values of $k_{t,s}$. A constant value of $k_{t,w}$=0,1 N/mm$^3$ is used in the tensioning phase, as this gave the best results for the unbonded beams. The figure shows that increasing $k_{t,s}$ from 20.000 to 100.000 N/mm$^3$ gave almost no change in response. This indicates that these values give the largest possible capacity for the bonded beams, or in other words, that a further increase of $k_{t,s}$ will produce the same load-deflection curve. It can also be observed that a value of $k_{t,s}$ = 100 N/mm$^3$ only gives a slight decrease in the capacity at the beginning of the linear response.

The model was also made with embedded reinforcements, which should be similar to the bond-slip bar reinforcement when the stiffnesses are high. However, the ultimate load capacity of the embedded model was $2F$ = 37,6 kN, while the bond-slip model did not seem to exceed $2F$ = 34,1 kN for any value of $k_{t,s}$. This can be explained by the choice of the stiffness parameter during the jacking phase, $k_{t,w}$, which was set to 0,1 N/mm$^3$. If it were possible to further reduce this parameter, and thereby the friction losses, the ultimate load capacity would probably have been closer to the embedded model.

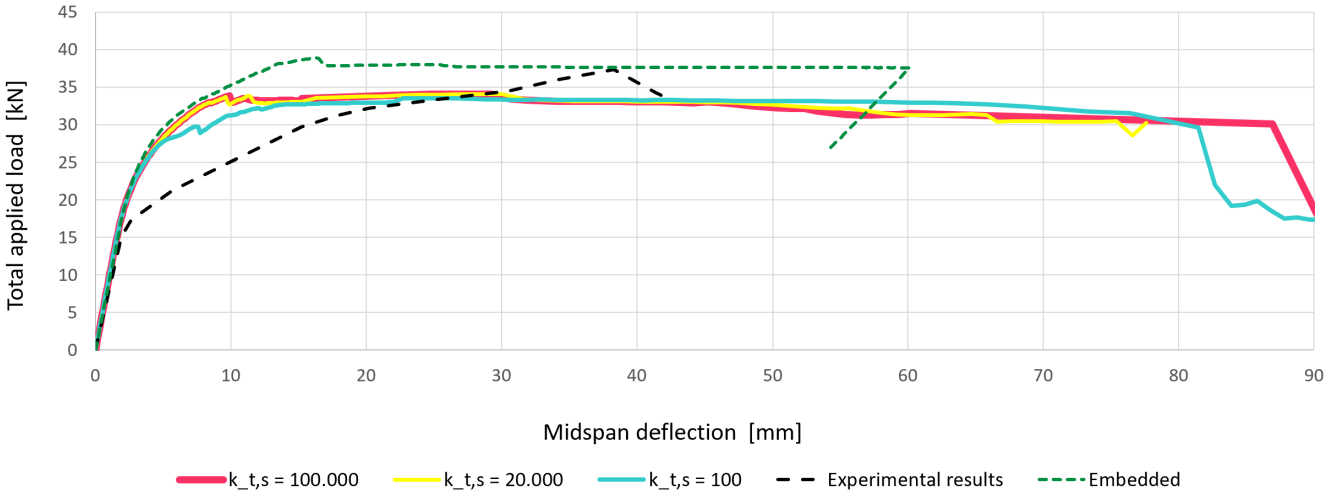


Figure 44: Load -deflection curves for unbonded PT2 models, by changing the value of $k_{t,s}$.
(Units of $k_{t,s}$ are in N/mm$^3$)

### 7.3.2 Comparison of bonded and unbonded tendons

The parametric study of the shear stiffness on the reinforcement interface indicated that the most appropriate values were $k_{t,w}$ = 0,1 N/mm$^3$ and $k_{t,s}$ = 100.000 N/mm$^3$. To compare a fully grouted and an ungrouted beam, these values, which are presented in Table 12, were used in order to compare the responses of the two beams during loading.

| Phase | Ungrouted beam | Grouted beam |
|---|---|---|
| Jacking phase /tensioning phase | $k_{t,w}$=0,1 N/mm$^3$ | $k_{t,w}$=0,1 N/mm$^3$ |
| Loading phase | $k_{t,w}$=0,1 N/mm$^3$ | $k_{t,s}$=100000 N/mm$^3$ |

Table 12: Overview of the choice of shear stiffness parameters for the ungrouted and the grouted beam during the two phases of the analysis.

The load-deflection curve of the two beams are presented in Figure 45, and the most important results are presented in Table 13 and compared to the results of the experiment and the analytical calculations (Section E in the Appendix). The grouted and the ungrouted beams had a similar behaviour for the initial linear part of the curve, including the point of cracking, which also occurred almost simultaneously. This part of the results is also corresponding to the experiment as well as to the analytical calculations. After the cracking point, the DIANA models have a stiffer behaviour than the beam in the experiment. The ungrouted beam reaches a peak point with an applied load of $2F$ = 26,2 kN, which is where the tendon starts to yield. The transition to a ductile behaviour causes a sudden drop in the slope of the load-deflection curve. This is caused by a numerical error. The grouted beam seems to withhold a higher applied load before the yielding point is reached, at $2F$ = 33,1 kN. After the yielding point, the curves flatten, and the approach a final load capacity of 34,1 and 31,5 kN, for the grouted and ungrouted beams, respectively.

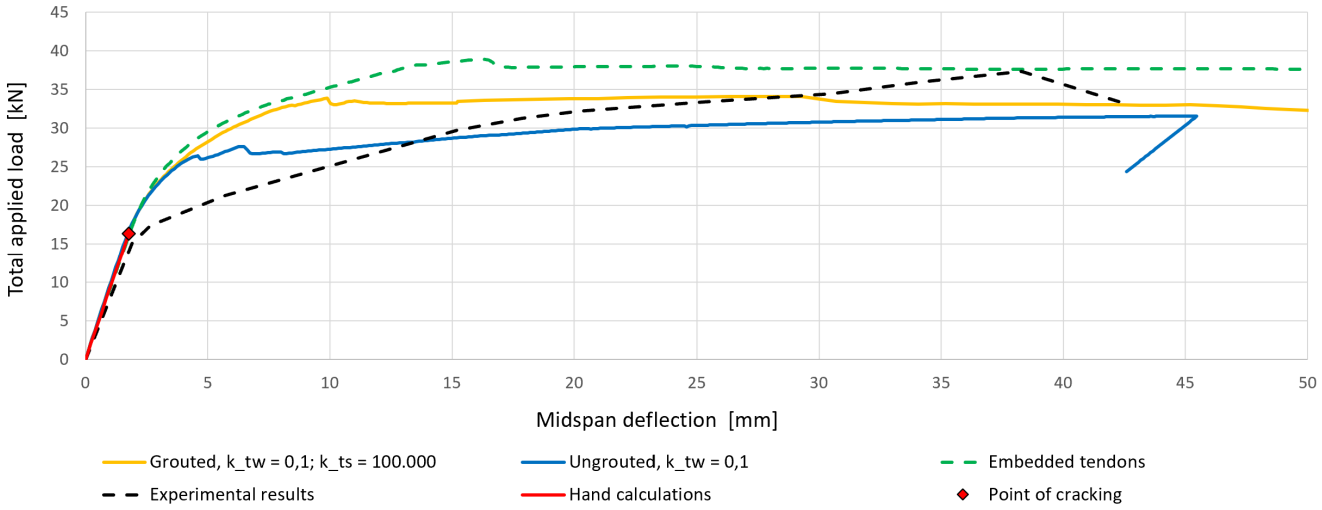


Figure 45: Beam PT2; Load-deflection curves for grouted and ungrouted beams, compared to analytical calculations an the embedded model.(Units of $k_t$ are in N/mm$^3$)

To summarize, the numerical results were not as expected for the load-deflection curves. It can be observed from Figure 45 that the grouted numerical model has a lower capacity than the embedded model, even though a similar behaviour is expected as they are supposed to represent a perfect bond. The experiments seem to neither give a good match with the grouted nor the ungrouted model. Despite this, a difference can be observed between the grouted and ungrouted numerical models when comparing the yield load and the ultimate capacity. More precisely, the ultimate capacity of the ungrouted beam is 2,6 kN lower than the

| | Numerical results (DIANA) | | Experimental results | Analytical calculations |
|---|---|---|---|---|
| | **Grouted beam** | **Ungrouted beam** | | |
| Cracking load $2F_{cr}$ [kN] | 16,2 | 16,3 | 17,2 | 16,3 |
| Corresponding midspan deflection [mm] | 1,72 | 1,72 | 2,6 | 1,76 |
| Load $2F$ at yielding of tendon[kN] | 33,1 | 26,2 | 35,0 | - |
| Corresponding midspan deflection [mm] | 10,0 | 4,4 | $\approx$ 34,5 | - |
| Ultimate load capacity $2F_{Rd}$ [kN] | 34,1 | 31,5 | 37,3 | 36,6 (34,6 ungrouted) |

Table 13: Comparison of numerical results for bonded and unbonded tendons, including the experimental results and analytical calculations.

grouted beam, which is a 7,6% decrease. This corresponds to the analytical calculations, where the reducion in capacity was 2 kN, or 5,5 %.

Figure 46 shows the crack widths of the grouted and the ungrouted beams just after the initiation of cracking. The cracking pattern for the two models is almost identical at these early stages. The crack widths are shown as a uniform ”zone” and not as concentrated cracks, and the maximum widths of the cracks at the bottom edge of the midspan are about $5{\cdot}10^{-4}$ mm. Some small cracks of about 0,05 mm can also be observed around the anchor on the right-hand side of the beam. Higher stresses are expected in this area, and normally when constructing a post-tensioned member, the area will be additionally strengthened. However, in this thesis, the additional strengthening is not included in the model. Therefore, some small cracks can be tolerated close to the anchor points.

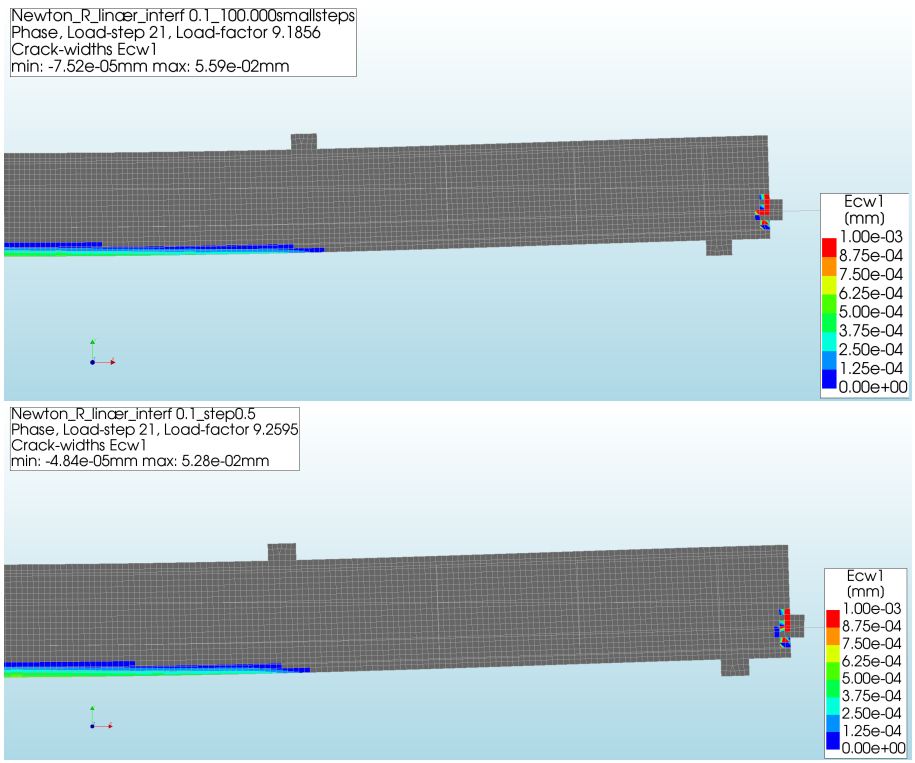


Figure 46: Beam PT2; Crack widths for a grouted beam(top) and an ungrouted beam(bottom) just after the appearance of the first cracks.

Figure 47 shows the cross-section stresses of the tendon at the point of yielding. The stresses are no longer even, but have a higher value in specific areas, where the cracks have appeared.

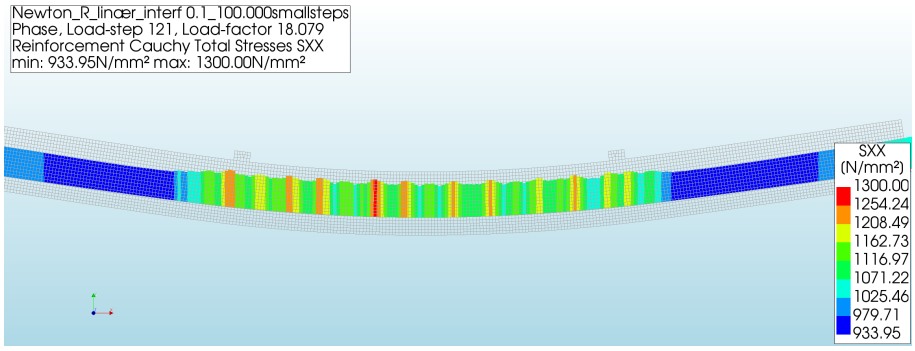


Figure 47: Beam PT2; Cross-section stresses [N/mm$^2$] of the tendon in a grouted beam at the ”peak” point in the load-deflection curve.

Figure 48 shows the crack widths and the crack patterns for the grouted and the ungrouted beam at the point of yielding. As the point of yielding is not occurring at the same loading configuration for the two beam models, these two results are not directly comparable; While the applied load is higher for the grouted beam, the maximum crack width is 0,59 mm, the maximum width for the ungrouted beam is 0,19 mm because of the lower stress levels. Nevertheless, the results show that the grouted beam develops finer and more evenly distributed cracks, while the cracks for the ungrouted beam are more concentrated, with a larger distance between the most prominent cracks.

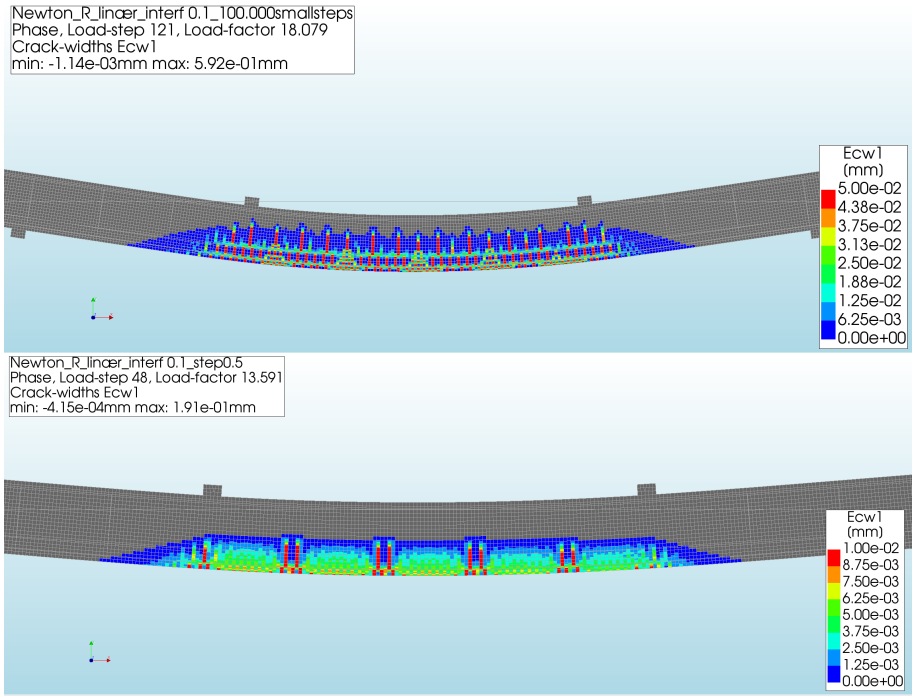


Figure 48: Beam PT2; Crack widths for a grouted beam(top) and an ungrouted beam(bottom) at the tendon yielding points of the load-deflection curves.

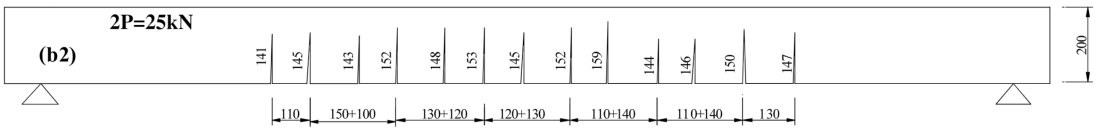


Figure 49: Cracking pattern reported in the reference experiment for PT2 for a load application of $2F$=25 kN. [25]

As can be observed in Figure 49 the reported cracking pattern is not corresponding to that of the ungrouted beam, even though the experiment had unbonded beams. Instead, this crack pattern seems evenly distributed and more similar to a grouted situation.

As the differences between the extreme cases of beams with no grout and fully grouted beams were relatively small, it was decided not to model a partly grouted beam. The expected difference between a partly grouted, fully grouted and not grouted beam would most likely be negligible.

# Part II

# Post-tensioned beam bridge with lack of grouting

# 8 Part II - General information

To model a generic beam bridge, technical drawings of post-tensioned place produced beam bridges in Norway were studied. By using an existing bridge as an inspiration for the model, it could be assured that the model was representative, considering both the geometry and the load configuration. With guidance from Håvard Johansen from Statens Vegvesen, it was decided to focus on bridges with two or more spans. After looking into Statens Vegvesens' bridge database, the bridge Rossvollbrua was chosen as an inspiration for the bridge model. The technical drawings from BRUTUS used to make the DIANA model are attached to the end of this document.

Rossvollbrua is a relatively new bridge built in 2004 and is located in Skaun municipality in Trøndelag. It has three lanes and is a part of the European Route E39 as it crosses the river Børselva. The bridge has a length of 114 m, distributed over four spans with a maximum length of 32 meters.

Figure 50: Rossvollbrua [27]

In the following chapters, the modelling approach of the bridge is described and the results from the analysis are presented. Similarly to Part I, a parametric study was performed to find appropriate stiffness parameters for the reinforcement interface. The non-linear behaviour of the bridge has been studied by applying the self weight and gradually increasing vertical traffic loads until the bridge failure. Lastly, the non-linear response of a grouted and an ungrouted bridge model was compared.

# 9 Modelling of the post-tensioned beam bridge

## 9.1 Topology, geometry and boundary conditions of the bridge model

### 9.1.1 Bridge topology and static model

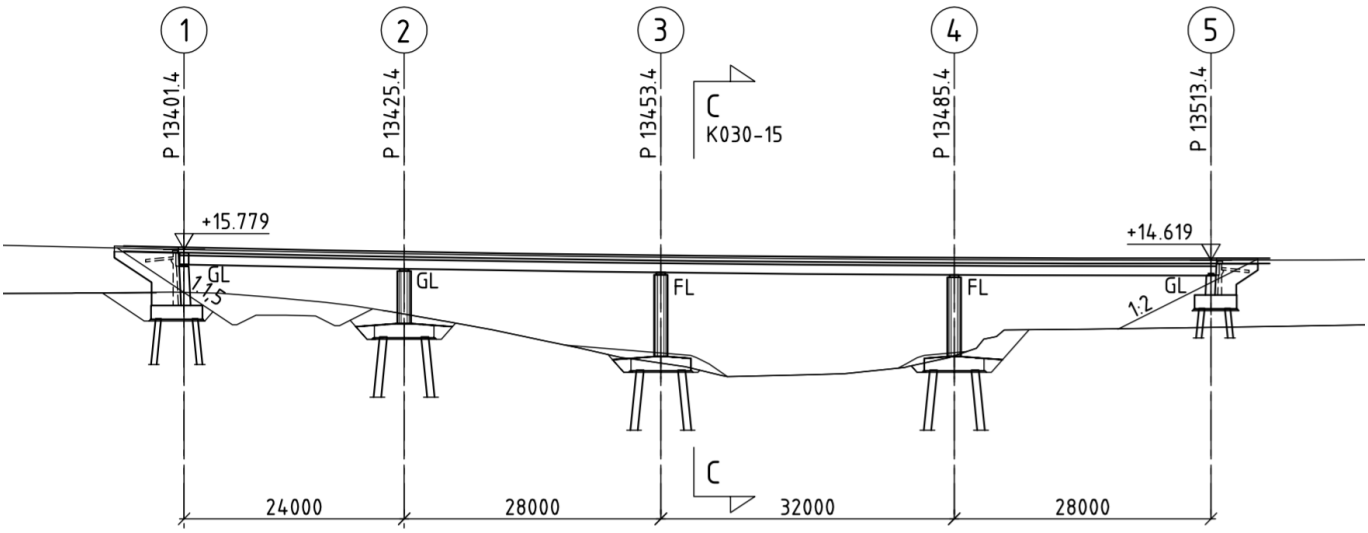


Figure 51: Topology of Rossvollbrua. Measures are in mm.
Figure from attachment K030-01.

A sectional view of Rossvollbrua is presented in Figure 51. The bridge has a 112 meter continuous concrete slab, supported by abutments at the far ends, as well as three intermediate columns dividing the bridge into four spans. The five supports are numbered from 1 to 5 in the figure and the support type is specified for each of them; Support 1, 2 and 5 are marked with ”GL”, short for *roller support* (glidelager) and the supports 3 and 4 are marked with ”FL”, short for *pinned support* (fastlager). At the roller supports, the beam is free to move horizontally, independently from the abutments or columns. The static model of the beam is presented in Figure 52. The difference in altitude between the two abutments, causing a slight slope of the slab, has been neglected, so that the bridge was modelled to be perfectly horizontal.

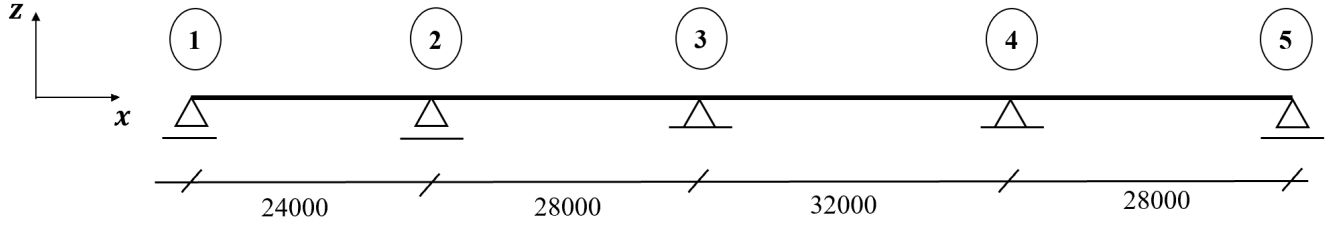


Figure 52: Static model of Rossvollbrua. Measures are in mm.

It was decided to model a single span of the bridge in DIANA, to limit the computational time. A single span is enough to study the non-linear behaviour with insufficient grouting. The span between column 3 and 4 was chosen as this is the largest span, where the most critical bending moments should appear. A static model of the span is presented in Figure 53a. As the edges of the model of this section are moment stiff and not pinned, a model which is clamped in both ends is suitable. However, this is a simplification of the real situation, because no rotation is prescribed above the columns. For a non-uniform loading of the bridge, which will often occur in the case of traffic load, there will often be a rotation at these points.

To further reduce the size of the model, only half of the span was modelled in DIANA, as seen in Figure 53b. By considering a completely symmetrical geometry and load configuration about the midspan, zero rotation was also assumed for the midspan cross-section. This means that this cross-section will stay horizontal, aligned with the *yz* plane. Movements are only restrained in the *x*-direction due to symmetry, but not in the *y*- and *z*-direction.

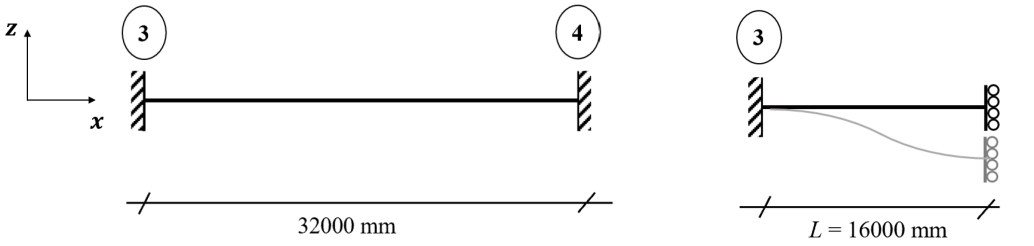


(a) Static model of the span between columns 3 and 4

(b) Static model for half of the span, as modelled in DIANA

Figure 53

### 9.1.2 Bridge cross-section

A view of the beam bridge cross-section is presented in Figure 54. The shape of the cross-section is quite complex, with diagonal edges of the two beams and a varying thickness of the slab. The cross-section is also inclined from the southern edge beam (sydside) to the northern edge beam (nordside).

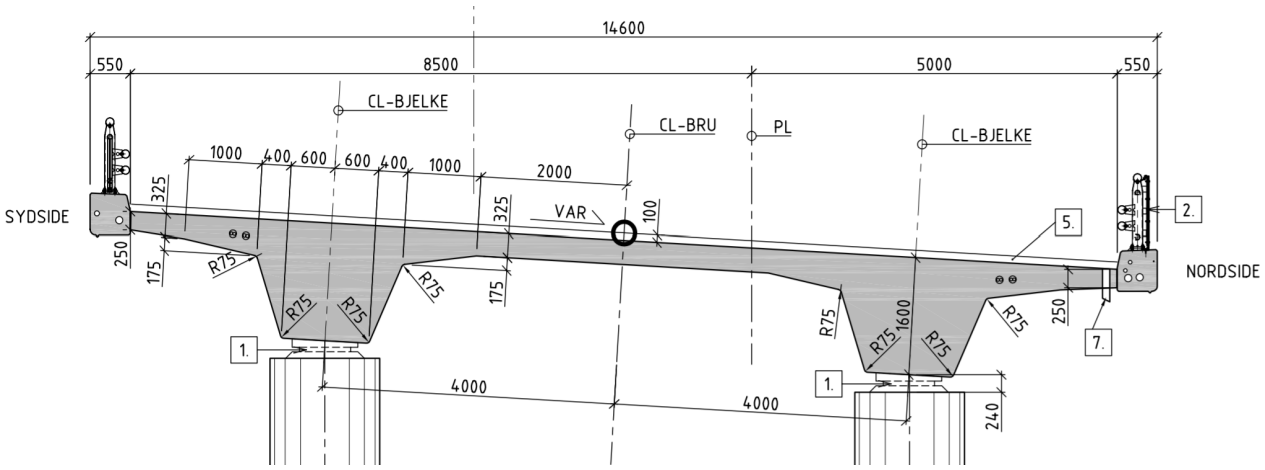


Figure 54: Cross-section of Rossvollbrua. Measures are in mm.
Figure from attachment K030-15.

To simplify the DIANA model, several adjustments were made to the original cross-section. The measurements of the model are presented in Figure 55. The inclination of the slab was disregarded and only half of the cross-section was modelled due to symmetry considerations. Therefore, the model includes only one of the beams, supporting a slab with a constant thickness of 325 mm and a width of 7300 mm.

The geometry of the beam was simplified by considering all edges as horizontal and vertical, giving a rectangular shape of the beam. The dimensions of the beam were selected so that the second moment of inertia $I_y$=9,786·$10^{11}$ $mm^4$ of the half bridge cross-section would remain the same as for the original cross-section.

Similarly to the beam models, a steel plate was attached to the point of support 3 to represent the column tops. The plate has a length of 800 mm in the $x$-direction, which corresponds to the radius of the column top. Between the steel plate and the bottom edge of the beam, an interface material is applied to ensure a connection between the column top and the concrete beam.

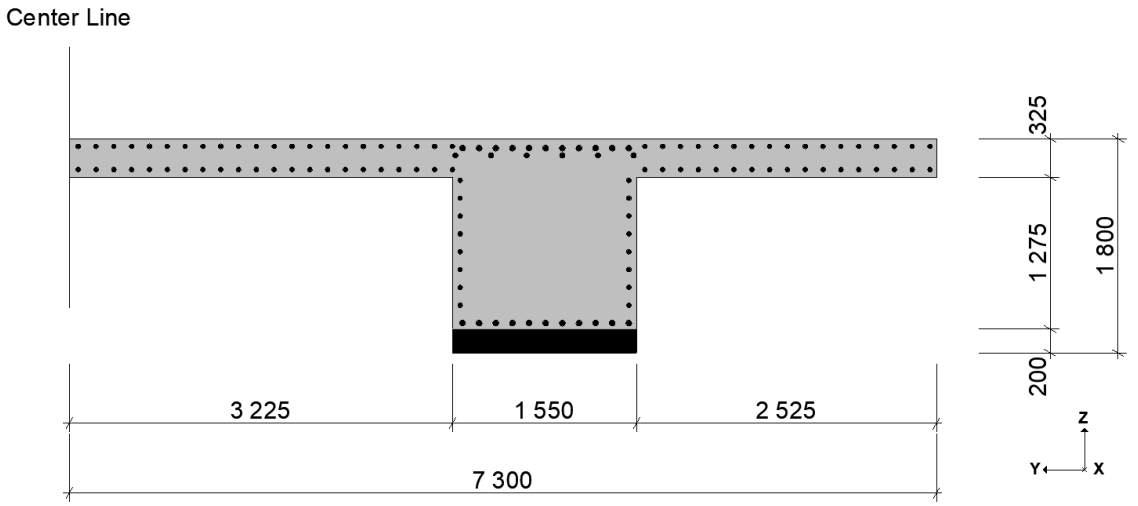


Figure 55: Cross-section of the DIANA bridge model. Measures are in mm

### 9.1.3 Bridge reinforcements

The passive reinforcements of the bridge model were made similarly to the reinforcement on Rossvollbrua, following the technical drawings K030-17 and K030-18, which can be found in the Attachments. This includes the longitudinal and shear reinforcements of both the deck and the beam. The reinforcement in the edge beams was disregarded and the shape and position of the reinforcements were adapted to the simplified shape of the cross-section where this was necessary. The cover was set to 55 mm, as stated in the technical drawings. The passive reinforcement was modelled as embedded reinforcements.

Rossvollbua has six post-tensioned tendons where the eccentricity $e$, varies along the length of the beam as presented in Figure 56. This shape is based on the technical drawing K030-21. $e$ is the vertical distance between the tendon center and the position of the neutral axis N.A of the cross-section, which is located at a distance $z_c$=526 mm below the top of the deck. In the model, the tendons were assumed to be completely parallel, with an eccentricity $e$ equal to the tendons 3 and 4.The maximum eccentricities were $e_1$ = 934 mm at midspan and $e_2$ = 384 mm over the support. At these two points, the cover of the tendons is 140 mm.

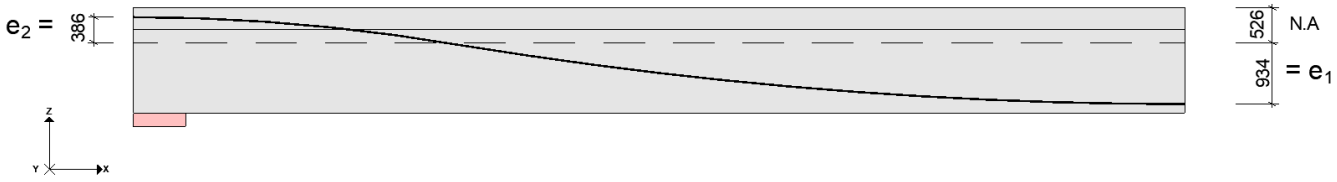


Figure 56: Position of the tendons in the bridge model. Measures are in mm

Technical drawing K030-22 states that the prestressing force is $S_{02}$ = 2806 kN per cable. This is the force that gives a 2‰ strain in the tendon. For $S_{02}$ tendons, the yield stress is 1670 N/mm$^2$ giving an area of $A = F \cdot \sigma$ = 2806 kN · 1670 N/mm$^2$= 1680 mm$^2$ for each tendon. It can therefore be assumed that the tendons used in Rossvollbrua were 12-strand tendons, with a diameter of 140 mm$^2$ per strand. Today, $S_{01}$ strands are normally used for post-tensioned bridges in Norway [28]. These have a yield stress of 1640 N/m$^2$ and was therefore used in the calculations of the yield strength. Conservatively, the yield strength of the tendons were assumed to be

$$f_{p,0,1k} = \frac{\sigma}{\gamma_S} = \frac{1640 \text{ N/mm}^2}{1,15} = 1426 \text{ N/mm}^2$$

### 9.1.4 Boundary conditions and constraints

The boundary constraints were defined as to imitate the static model presented in Figure 53b, and is elaborated in Figure 57;

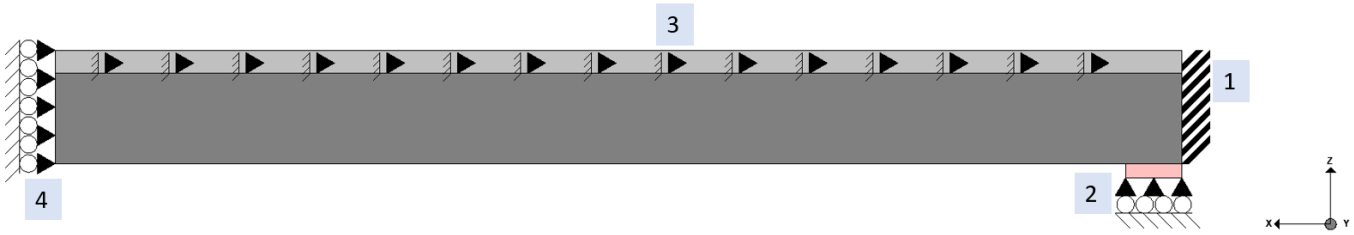


Figure 57: Boundary conditions of the bridge model

| | |
|---|---|
| 1. Concrete edge over support; | Fixed translations in x-direction<br>Fixed rotations in x-direction<br>Fixed rotations in y-direction<br>Fixed rotations in z-direction |
| 2. Steel plate; | Fixed translations in z-direction |
| 3. Longitudinal edge of the deck; (Along the Center Line) | Fixed translations in y-direction |
| 4. Edge at midspan; | Fixed translations in x-direction for the concrete<br>Fixed translations in x-direction for the tendons |

Fixed translations were modelled in the x-direction to simulate the continuation of the beam at midspan. The constraints were applied to both the concrete and the tendons. A fixed support was modelled by applying fixed rotations in all directions for the concrete as well as fixed translations in the z-direction for the support plate. To simulate the continuation of the bridge deck, fixed translations were modelled in the y-direction along the center line of the model. The constraints for the reinforcement at the anchoring points were applied through tyings and the ”NOBOND” option in the analyses. Since the model is assumed symmetrical about both the transverse and longitudinal direction, some behaviour that would appear for a whole bridge span model is neglected. By applying constraints in the longitudinal direction, the bridge can not rotate if a load is bigger on one side of the bridge.

## 9.2 Material properties of the bridge model

According to the technical drawing K030-01 the passive reinforcement was B500C. In technical drawing K030-15 it is stated that B55 concrete was used for the bridge.

Table 14 states the material properties used for the bridge model. The design values were used to calculate the properties of the concrete and the passive reinforcement
Eurocode 2, 3.1.6, equation 3.15;

$$f_{cd} = \alpha_{cc} \cdot \frac{f_{ck}}{\gamma_c} = 0.85 \cdot \frac{55\,\text{N/mm}^2}{1,5} = 31,17\,\text{N/mm}^2$$

Eurocode 2, 3.2.7, figure 3.8;

$$f_{yd} = \frac{f_{yk}}{\gamma_s} = \frac{500\,\text{N/mm}^2}{1,15} = 31,17\,\text{N/mm}^2$$

| **Material** | **Symbol** | **Magnitude** | **Unit** |
|---|---|---|---|
| **Concrete B55** | | | |
| Elastic modulus | $E_c$ | 38000 | N/mm$^2$ |
| Compressive strength | $f_{cd}$ | 31,17 | N/mm$^2$ |
| Tensile strength | $f_{ct}$ | 4,35 * | N/mm$^2$ |
| Poisson ratio | $\upsilon_c$ | 0,2 | |
| Concrete weight | $\gamma_c$ | 2400 | kg/m$^3$ |
| **Passive reinforcement** | | | |
| Elastic modulus | $E_s$ | 200000 | N/mm$^2$ |
| Yield strength | $f_y$ | 434 | N/mm$^2$ |
| **Prestressed tendon** | | | |
| Area of a single tendon | $A_p$ | 1680 | mm$^2$ |
| Elastic modulus | $E_p$ | 195000 | N/mm$^2$ |
| Yield strength | $f_{pd}$ | 1426 | N/mm$^2$ |
| Mass density | $\gamma_s$ | 7850 | kg/m$^3$ |

Table 14: Material properties of the bridge model.
* formula can be found in Section A of the Appendix

### 9.2.1 Material models

**Concrete**

When defining the properties for the concrete block, the Element Class was set to *Structural Solids*. The concrete material was defined with the following properties;

| | |
|---|---|
| Class; | *Concrete and masonry* |
| Material model; | *Total strain based crack model* |
| Crack orientation; | *Rotating* |
| Tensile curve; | *Exponential* |
| Crack bandwidth specification; | *Rots* |
| Poisson's ratio reduction model; | *No reduction* |
| Compression curve; | *Parabolic* |
| Reduction due to lateral cracking; | *Reduction model by Vecchio and Collins 1993* |
| Lower bound reduction curve | 0,6 |
| Stress confinement model | *No increase* |

**Reinforcement**

The passive reinforcements of the bridge model, including the tendons, were defined as;

| | |
|---|---|
| Class; | *Reinforcements and pile foundations* |
| Material model; | *Von Mises Plasticity* |
| Hardening function; | *No hardening* |

**Support plate**

| | |
|---|---|
| **Geometry** | |
| Length | 800 mm |
| Width | 1550 mm |
| Thickness | 200 mm |
| **Material properties** | |
| Class | *Steel* |
| Material model | *Linear elastic isotropic* |
| Elastic modulus | 210000 N/mm$^2$ |
| Poisson's ratio | 0,3 |
| Mass density | 0 |
| **Interface material properties** | |
| Class | *Interface elements* |
| Material model | *non-linear elasticity* |
| Type | *3D surface interface* |
| Normal stiffness modulus-z | 34200 N/mm$^3$ |
| Shear stiffness modulus-x | 0.000342 N/mm$^3$ |
| Shear stiffness modulus-y | 0.000342 N/mm$^3$ |
| No-tension or diagram | *No-tension with shear stiffness reduction* |
| Critical interface opening for reduction | 0,001 mm |
| Normal/shear stiffness reduction factor | 0 |

Table 15: Dimensions and material properties of the support plate

## 9.3 Loads

The relevant loads were found using "Håndbok R412 - Bruklassifisering", hereby referred to as R412. R412 is used to decide the classification of bridges, which includes the calculation of the maximum allowed traffic load on existing bridges based on technical drawings, previously calculated capacities and the state of the bridge. In R412 the loads are divided in:

- permanent loads
- variable loads
- deformation loads
- accidental loads

In this thesis, the most prominent permanent and variable loads were considered, while the deformation and accidental loads were not taken into account. Permanent loads are defined in R412 as loads that can

be considered constant within the time period considered [29]. For the bridge model, only the self weight of reinforced concrete was included. R412 defines variable loads as loads that vary in time, such as traffic loads, nature loads and loads from removable equipment. The main variable load of the bridge model was the traffic load.

## 9.4 Self weight

The self weight $g$ was calculated by Equation 12 where $\rho_c$ is the concrete density and $A$ is the cross-sectional area of the bridge. The self weight was found to be $g$ = 104,4 N/mm in Appendix I.2

. $$g = \rho_c \cdot A \tag{12}$$

## 9.5 Traffic loads

In R412, traffic load is defined as the loading in the vertical and the horizontal direction from pedestrians as well as the light and heavy vehicles on the carriageway, footpath, bike lane and central reservation.

Each bridge is assigned a serviceability class (Bruksklasse). The main principle is that this serviceability class shall reflect the serviceability load that can cross the bridge without restrictions. Furthermore, each bridge is classified as the highest serviceability class allowed from the capacity of the weakest element of the bridge. There are four serviceability classes in R412:

- Serviceability class 10 (Bk10)
- Serviceability class T8 (BkT8)
- Serviceability class 8 (Bk8)
- Serviceability class 6 (Bk6)

Rossvollbrua has a serviceability class of Bk10/60. In Bk10/60, each vehicle can apply a maximum load of 10 tons per axle and a total of 60 tons. Figure 3.2-1 from R412, here presented as Figure 58, was used to determine the vertical loads applied to the model.

| Lasttype | Lastkonfigurasjon | | Bruksklasser | | | |
|---|---|---|---|---|---|---|
| | (*) $H_{kN}$ | | Bk10 | BkT8 | Bk8 | Bk6 |
| Hjullast | 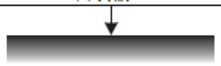 | H | 80 | 56 | 56 | 42 |
| Aksellast | 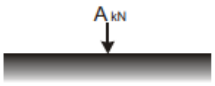 | A | 160 | 112 | 112 | 84 |
| Boggilast | 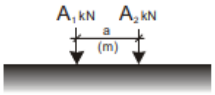 | $A_1$ | 65 | 40 | 40 | 30 |
| | | $A_2$ | 160 | 112 | 112 | 84 |
| | | a | 1,3 | 1,2 | 1,2 | 1,2 |
| Trippelboggilast | 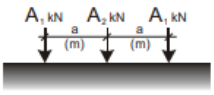 | $A_1$ | 70 | 60 | 50 | 40 |
| | | $A_2$ | 140 | 84 | 84 | 56 |
| | Aksellastenes rekkefølge er vilkårlig | a | 1,3 | 1,2 | 1,2 | 1,2 |
| Kjøretøylast | 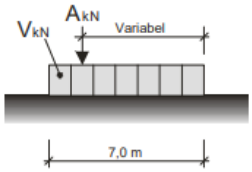 | A | 40 | 32 | 32 | 24 |
| | | V | 300 | 280 | 220 | 180 |
| | Aksellasten plasseres i ugunstigste stilling | | | | | |
| Vogntoglast | 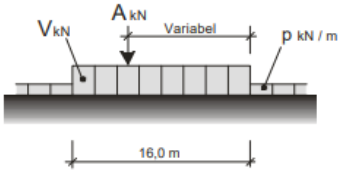 | A | 40 | 32 | 32 | 24 |
| | | V | 500 | 400 | 320 | 280 |
| | Aksellasten plasseres i ugunstigste stilling | p | 6 | 6 | 6 | 6 |

Figure 58: Traffic loads for different servicibility classes [29]

The vertical traffic loads should be placed in the least favourable position on the available carriageway. The carriageway is defined as the smallest horizontal width of:

- The distance between kerbs.
- The distance between the kerb and vertical edge or vehicle restraint system.
- The distance between two vertical edges or vehicle restraint systems.

Rossvollbrua has a carriageway of $w$ = 13,5 m, as the two edge beams of 2 · 0,55 m can not take any load. Since only half the width of the bridge was modelled, the considered carriageway for the model was 6,75 m. The carriageway was further divided into notional lanes. In Eurocode EN 1991-2:2003 Table 4.1 [30], the number of notional lanes for carriageways is found by Equation 13, where $n1$ is the integer number of

notional lanes and $w$ is the length of the carriageway.

$$\text{when } w \geq 6\text{m}; \qquad n1 = Int(\frac{w}{3}) = Int(\frac{13,5}{3}) = 4 \tag{13}$$

As the carriageway of the bridge was 13,5 m, four notional lanes could be placed within it.
Eurocode EN 1991-2:2003, 4.2.4 states that:

- The lane giving the most unfavourable effect is numbered Lane Number 1, the lane giving the second most unfavourable effect is numbered Lane Number 2, etc.
- The locations of notional lanes should not be necessarily related to their numbering
- For each individual verification (e.g. for a verification of the ultimate limit state of resistance of a cross-section to bending), the number of lanes to be taken into account as loaded, their location on the carriageway and their numbering should be so chosen that the effects from the load models are most adverse
- For fatigue representative values and models, the location and the numbering of the lanes should be selected depending on the traffic to be expected in normal conditions

The lanes for the full bridge width was distributed as presented in Figure 59. Lane Number 1 and Lane Number 2 was placed to the far right of the bridge span to give the most unfavourable load case for one bridge beam.

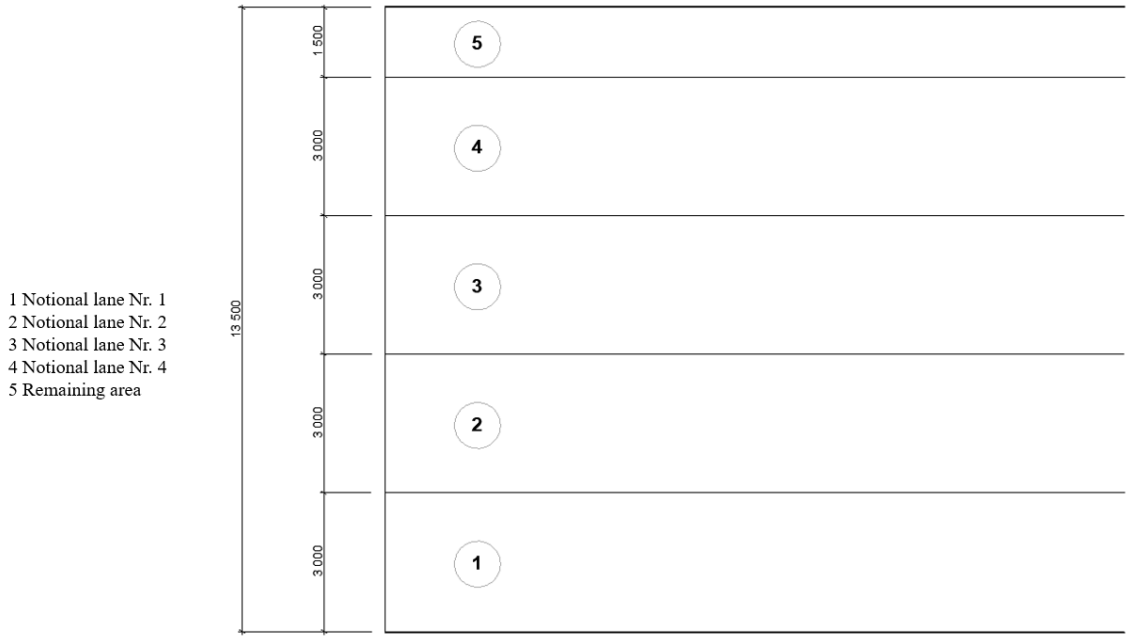


Figure 59: Notional lanes of the whole bridge width. Measures are in mm

The vertical loads are distributed as field loads over the carriageway and notional lanes. The load from heavy vehicles is 500 kN, as can be observed in Figure 58, and is distributed over a field with a width of 3

m and a length of 16 m. An axle load of 40 kN should be placed in the least favourable position of the field load as a point load. Since the model is divided at midspan, the load from heavy vehicles was modelled as a field load with a width of 3 m and a length of 8 m. The load field was placed at midspan. The length of the load field was reduced from 16m to 8m due to the load symmetry of the model. The axle load was reduced from 40 kN to 20 kN and was placed at midspan at half the width of the field load.

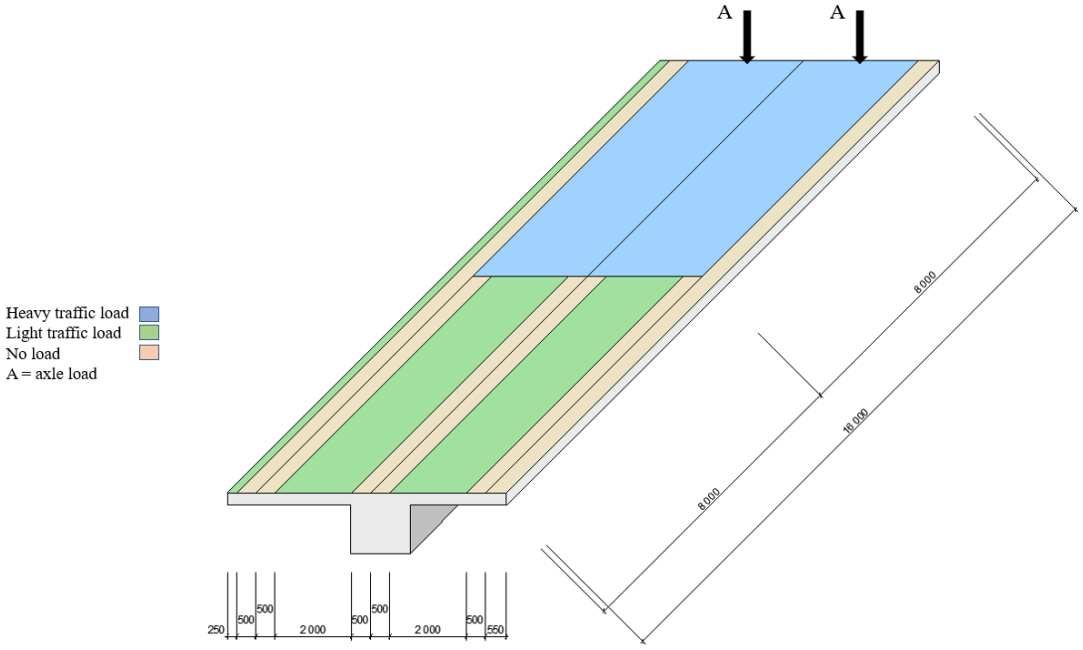


Figure 60: Traffic load placement in the bridge model. Measures are in mm.

A maximum of two lanes can be loaded by heavy vehicles. The remaining lanes can be loaded by a light traffic load of 6 kN/m$^2$ which should be distributed as a field load with a width of 2 m. After placing the notional lanes on the far edge of the model, there was a remaining area with a width of 0,25 m. This area was loaded with light traffic load. The traffic load placement is presented in Figure 60.

The results are not representative for the whole bridge span and should not be considered as an indicator for the capacity of the bridge. Regarding the symmetry of the model, the bridge span would have four loaded lanes with heavy traffic. Moreover, the 5th notional lane, which should not be loaded would now be loaded with light traffic loads. To model the whole bridge span correctly, both beams should have been included. This was not done as the interesting results for this thesis was the effect of grouting in the beam part of the bridge. Because many analyses were to be performed, modelling a quarter of the bridge was the best solution to save time.

It should be mentioned that there are also horizontal traffic loads such as braking loads, side loads and centrifugal loads. These loads were looked into, but as the thesis developed, it was decided that only vertical loads should be taken into account [29].

## 9.6 Prestressing force

The tendons in Rossvollbrua were loaded with a prestressing force $P$ = 2806 kN, as stated in 9.1.3, and it was decided to load the tendon of the model with the same force. Conservatively, the long term loss of prestress should be taken into account. Following the recommendations from the supervisor of this thesis, Daniel Cantero, the prestressing force was reduced by 35%, to simulate the state of an old bridge. The prestressing force in this thesis was then decided to be:

$$P = 2806\ kN$$

$$0,65 \cdot P = 1824,0\ kN$$

## 9.7 Meshing and analysis of the bridge model

Following "Guidelines for Nonlinear Finite Element Analysis of Concrete Structures" [17] the element size should not exceed $\frac{h}{6}$, or 300 mm. An attempt of running a general analysis on the bridge model was made with an element size of 100 mm. It was concluded that both the meshing of the elements as well as the analysis itself was too time-consuming. An adaptive mesh with solid elements of type HX24L was made with an element size of about 200 mm.

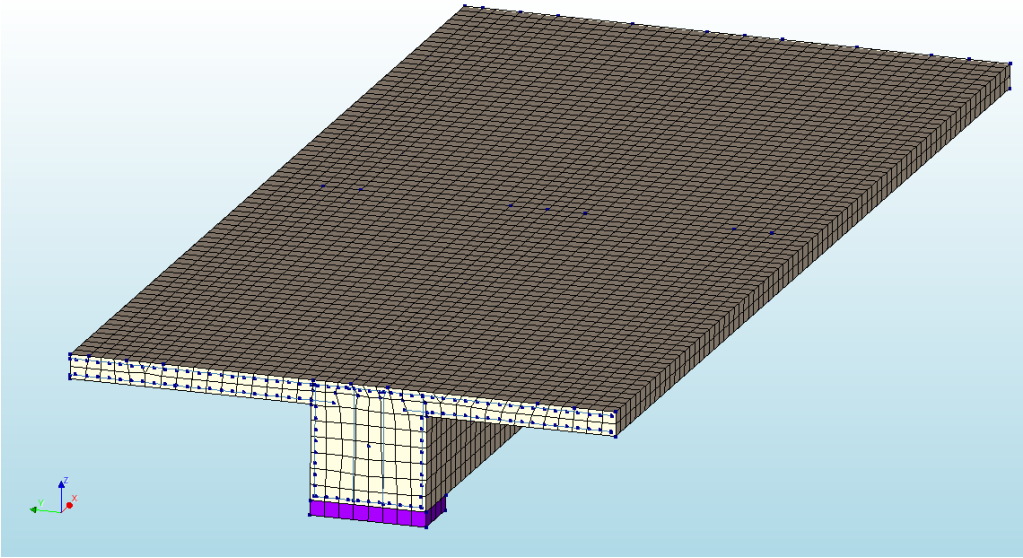

Figure 61: Meshed bridge model

### 9.7.1 Analysis set-up for load control

Before a more detailed analysis of the bridge model were to be performed, the self weight and the traffic load were added to the model one by one, in separate analyses, without including the prestressing load. This way, the results could be compared to simple analytical calculations to confirm that the bridge had a correct

behaviour. Figure 62 shows how the self weight was added in an anysis by using just one single execute block.

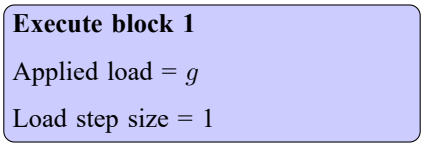


Figure 62: The analysis for the self weight control

Similarly, the traffic load was applied to the model with the analysis given in Figure 63.

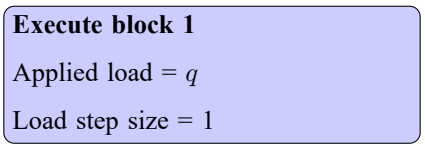


Figure 63: The analysis for the traffic load control

### 9.7.2 Analysis set-up for the parametric study

The parametric study was performed by making a phased analysis, which is visualised in Figure 64. The second phase is defined to simulate the anchoring of the tendons by activating the tyings. This made it possible to study the prestressing loss after the anchoring of the tendon.

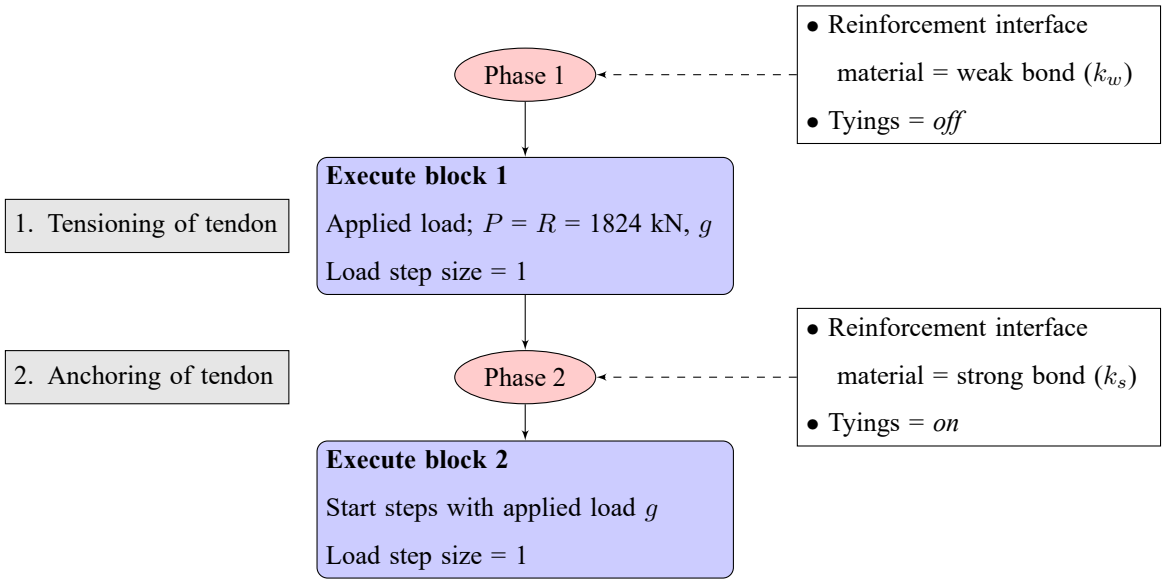


Figure 64: Flow chart showing the analysis set-up used during the parametric study

### 9.7.3 Analysis for control of prestressing

Figure 65 shows the set-up of the analysis for the control of the prestressing load of the bridge. Here, the self weight and the traffic loads were not added.

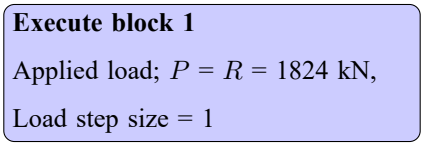


Figure 65: The analysis for the prestress control

### 9.7.4 Non-linear analysis

To study the non-linear behaviour of the bridge, a non-linear analysis was performed with gradually increasing traffic load until failure. Two types of analyses were performed; One where the tendons were defined as embedded reinforcements and one where the tendons were bond-slip reinforcements.

Figure 66 visualises the analysis set-up in DIANA for the embedded model.

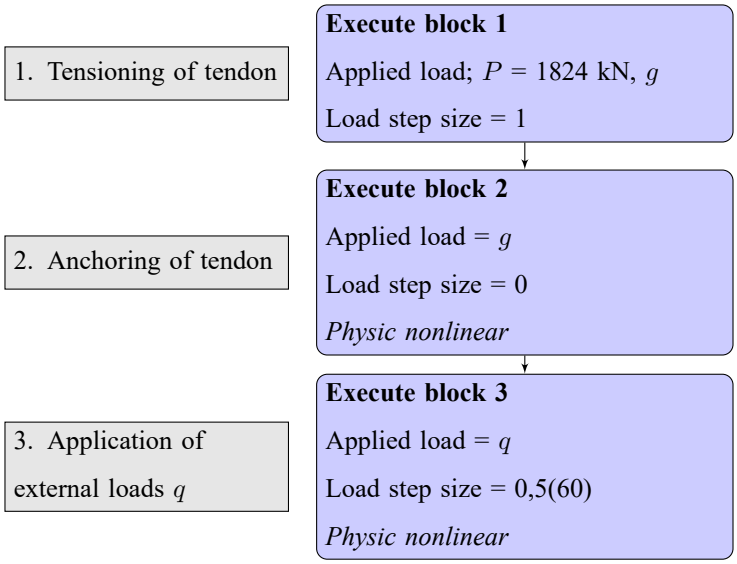


Figure 66: Flow chart showing the order of the non-linear analysis on the bridge model with embedded tendons

Figure 67 shows a flow chart of how the non-linear analyses were defined for the bridge when the tendons were modelled as bond-slip reinforcements.

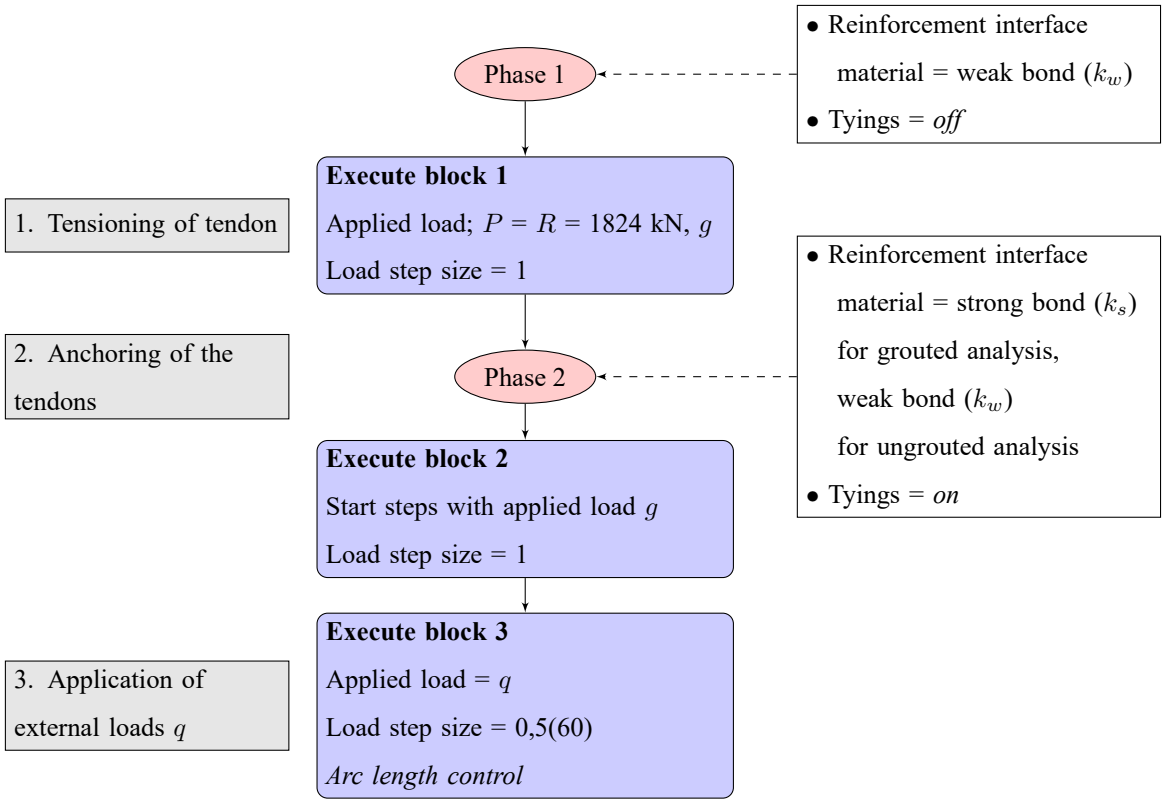


Figure 67: Flow chart showing the order of applied loads during an analysis with bond-slip tendons

# 10 Results from bridge model analysis

## 10.1 Load control

As an initial control of the model, it was decided to apply the loads one at a time. This way, potential errors could be detected before the loads were combined and the non-linear behaviour was studied. The results are compared to the analytical calculations that can be found in Section I.2 of the Appendix.

### 10.1.1 Self weight control

For the self weight, an analysis with one load step was created. The displacements are presented in Figure 68, while the moment diagram is presented in Figure 69. The comparison between the numerical and the analytical results is presented Table 16.

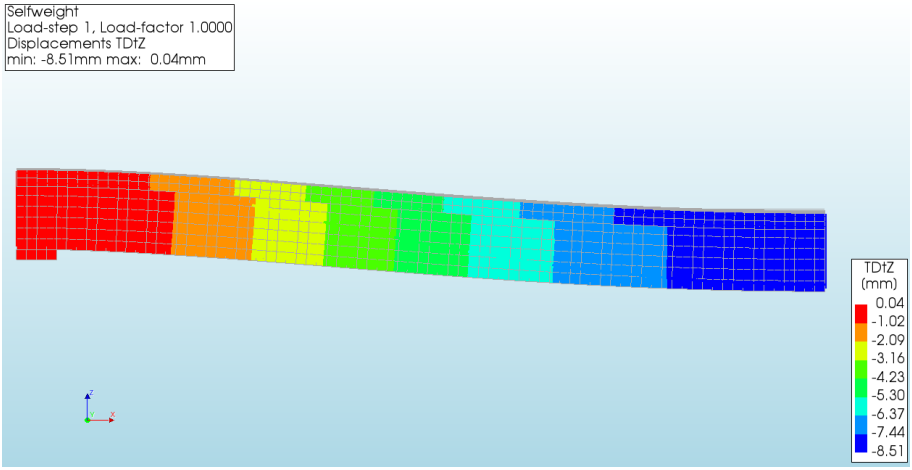


Figure 68: Vertical displacements of the bridge model after the application of self weight.

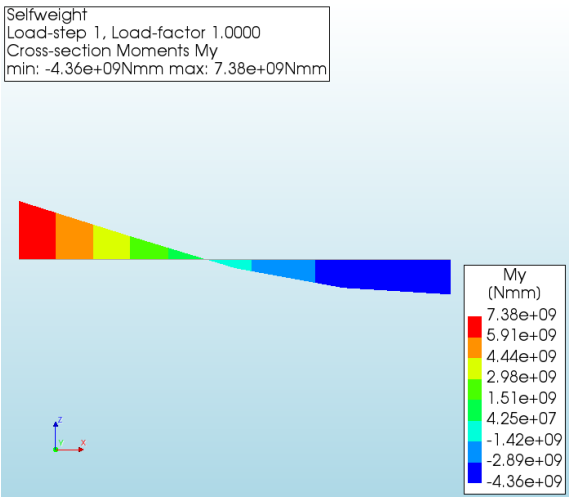


Figure 69: Resulting moment diagram when only self weight is applied to the bridge model

| | Reaction force [kN] | $M_y$ over support [kNm] | $M_y$ at midspan [kNm] | Max. deflection [mm] |
|---|---|---|---|---|
| **Analytical calculations** | 1669,9 | 8906,2 | -4453,1 | 7,66 |
| **DIANA** | 1650,7 | 7379,3 | -4359,6 | 8,51 |
| **Difference** | - 1,1% | - 17,1% | - 2,1% | + 11% |

Table 16: Comparison of numerical and analytical calculations for the bridge model, considering only self-weight

As presented in Table 16, the reaction force and the moment at midspan are especially close and are respectively 1,1% and 2,1% lower than the analytical results. The bending moment over the support is 17,1% lower than the analytical results. The difference between these results could be due to the fact that the static model used for the analytical calculations considered the reaction force as a point load. However, the support plate gives a reduced bending moment at the support because the reaction force is distributed over its width.

### 10.1.2 Traffic load control

For the traffic load, an analysis with one load step was created. The displacements are presented in Figure 70, while the moment diagram is presented in Figure 71. The difference between the numerical and the analytical results is presented in Table 17.

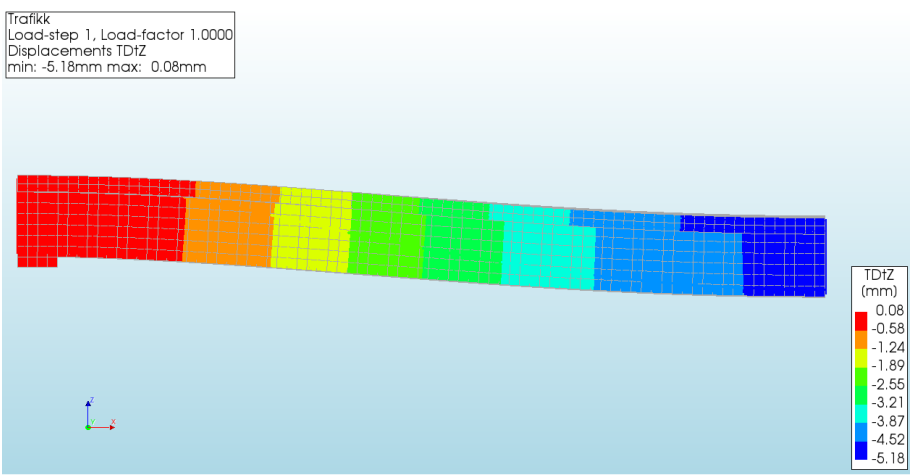


Figure 70: Vertical displacements of the bridge model after the application of traffic load.

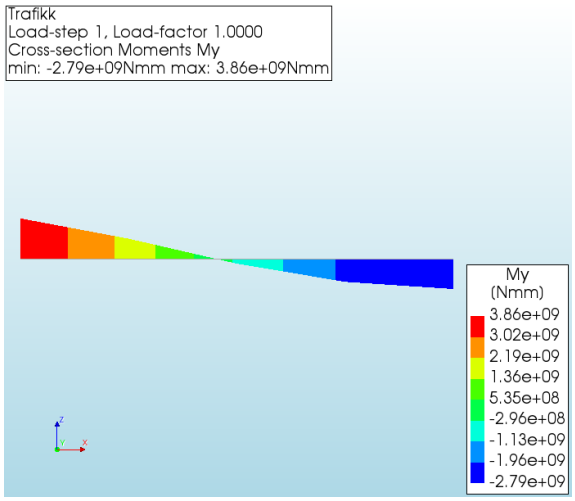


Figure 71: Resulting moment diagram when only the traffic load is applied to the bridge model

| | **Reaction force [kN]** | **$M_y$ over support [kNm]** | **$M_y$ at midspan [kNm]** | **Max. deflection [mm]** |
|---|---|---|---|---|
| **Analytical calculations** | 672,0 | 3584,0 | -1792,0 | 3,08 |
| **DIANA** | 671,2 | 3855,0 | -2786,0 | 5,18 |
| **Difference** | - 0,1% | + 7,5% | + 55% | + 68% |

Table 17: Comparison of numerical and analytical calculations for the bridge model, considering only traffic load

As presented in Table 16 and Table 17, the results from the DIANA analysis and the analytical calculations are generally in good agreement. The moment at midspan and the deflections are bigger in the DIANA analysis than the analytical results. This was expected, as the traffic load was applied as a simplified constant line load in the analytical calculations, while it was applied as bigger field- and point loads over midspan and lower field loads near the support, in the DIANA model.

When controlling the analyses, an error was discovered. The light traffic load which should be 6 kN/m was put in the model as 3 kN/m. This means that the total traffic load was reduced by 16,5 % compared to the correctly calculated traffic load. As this mistake was in all the bridge analyses, it was decided to let the light traffic load remain as 3 kN/m as it was too time-consuming to run all the analyses again with the correct traffic load. Furthermore, it can be argued that the results still show the different behaviour of a grouted and ungrouted bridge as the error appears in all the analyses.

## 10.2 Parametric study of reinforcement stiffness parameters

### 10.2.1 Weak stiffness parameters

When the reinforcement has a parabolic shape, both the normal stiffness and the shear stiffness of the reinforcement interface elements has to be calibrated. From the parametric study in Part I, it was experienced that the stiffness parameters which had a good agreement with the experimental results were not necessarily in agreement with the analytical results. When modelling the bridge, it was attempted to find stiffness

parameters that would coincide with the analytical results so that the model would be easier to control. As observed in Part I, the loss of prestressing force due to friction is automatically calculated in DIANA and is dependent on the stiffness parameters. In this regard, the losses due to friction were calculated analytically and the stiffness parameters were calibrated thereafter.

The prestressing force at midspan was calculated analytically by Equation 14 found in Eurocode 2 5.10.5.2,(5.45):

$$P_x = P_{max} e^{-\mu(\theta + kx)} \tag{14}$$

The complete calculation can be found in Section I.3 of the Appendix. It was found that the loss of prestressing force due to friction should be between 3,6% and 6,3%. The stiffness parameters were found by running a two-phased analysis on the bridge model. The first phase consisted of one load step where the prestressing load, the reaction forces on the anchorages and the self weight were applied. In this phase, the weak bond interface stiffness parameters were tested. In the second phase, only the self weight was included and the anchorages were activated using tyings. In this phase, the stiffness parameters were $k_{n,s} = 1 \cdot 10^6$ N/mm$^3$ and $k_{t,s} = 1 \cdot 10^5$ N/mm$^3$, as used in Part I. The results from the parametric analysis are presented in Table 18. The weak normal stiffness parameter is denoted $k_{n,w}$ while the shear stiffness parameter is denoted $k_{t,w}$. $P_{max}$ is the prestressing force at the anchoring point and $P_{mid}$ is the prestressing force at midspan.

| $k_{t,w}[N/mm^3]$ | $k_{n,w}[N/mm^3]$ | $Pmax[kN]$ | $P_{mid}[kN]$ | Loss [kN] | Loss [%] | Deflection [mm] |
|---|---|---|---|---|---|---|
| 1 | 1 | 1800 | 15,5 | 1784,5 | 99,14 | 7,16 |
| 1 | 0,01 | 1800 | 13,5 | 1786,5 | 99,25 | 7,25 |
| 0,1 | 1 | 1790 | 144 | 1646 | 91,96 | 5,69 |
| 0,01 | 1 | 1820 | 1120 | 700 | 38,46 | 0,55 |
| 0,001 | 1 | 1820 | 1720 | 100 | 5,49 | -2,20 |
| 0,001 | 0,1 | 1820 | 1720 | 100 | 5,49 | -2,20 |
| 0,001 | 0,01 | 1820 | 1720 | 100 | 5,49 | -2,17 |
| 0,001 | 10 | 1820 | 1720 | 100 | 5,49 | -2,18 |
| 0,001 | 1000000 | 1820 | 3,52 | 1816,48 | 99,81 | 7,79 |

Table 18: Results from the parametric study for the bridge model

As expected, the normal stiffness parameter should be bigger than the shear stiffness parameter [31]. A normal stiffness parameter that was 100-10000 times higher than the shear stiffness parameter would yield the best results. Normal stiffness parameters outside of this scope would result in an almost complete loss of prestress or unwanted reinforcement behaviour.

It was found that a change in the shear stiffness parameter had the most significant impact on the loss of prestress in the tendon. As presented in Table 18, the loss of prestressing force changed drastically when the shear stiffness parameter was decreased from 0,1 N/mm$^3$ to 0,001 N/mm$^3$.

When using a shear stiffness parameter $k_{t,w}$ = 0,001 N/mm$^3$ there was a 5,49% loss of prestressing force in the tendon. This was found satisfactory as it was between the maximum and minimum analytical calculations of 3,6% and 6,3%. It was observed that a small change in the normal stiffness parameter had little effect on the loss of prestress and the upward deflection of the bridge. However, the normal stiffness parameter should be minimum 1 N/mm$^3$, as the reinforcement got an unwanted shape when $k_{n,w}$ had a lower value. This is presented in Figure 72 and Figure 73.

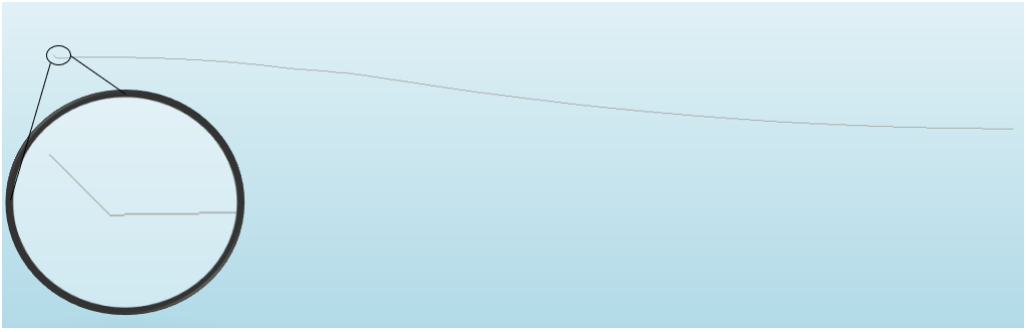

Figure 72: Tendon shape with applied parameters $k_{n,w}$ = 0,1 and $k_{t,w}$ = 0,001

Figure 73: Tendon shape with applied parameters $k_{n,w}$ = 0,01 and $k_{t,w}$

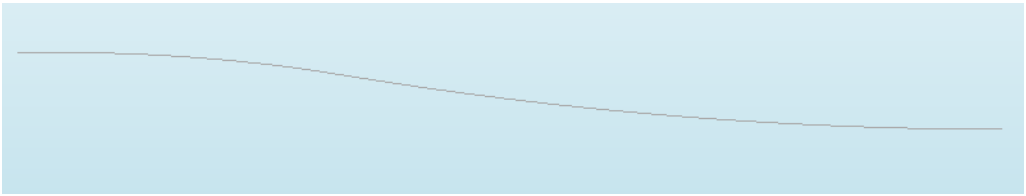

Figure 74: Tendon shape with applied parameters $k_{n,w}$ = 1 and $k_{t,w}$ = 0,001

Based on the results presented in Table 18 and Figure 74, it was decided to use the weak stiffness parameters $k_{n,w} = 1$ N/mm$^3$ and $k_{t,w} = 0,001$ N/mm$^3$ for the weak bond interface material for the bridge model.

### 10.2.2 Stiff stiffness parameters

At DIANAs web page [31] a guideline for reasonable choices for the shear- and normal stiffness parameters for the stiff interface elements is proposed. For the bridge model, these were found to be between $5 \cdot 10^4$ N/mm$^3$ and $5 \cdot 10^5$ N/mm$^3$. The complete calculation is found in Chapter H.2 of the Appendix. The shear stiffness parameter $k_{t,s}$ is recommended to be 10 to 100 times lower than the normal stiffness, which means it should be between $5 \cdot 10^2$ N/mm$^3$ and $5 \cdot 10^4$ N/mm$^3$. However, it can be argued that the stiffness parameters found from this guideline can be inaccurate. The formulae used to calculate the stiffness parameters

is dependent on the mesh size and the user's definition of a suitable elastic modulus for the elements surrounding the interface. Finally, it is stated on the DIANA web page [31] that the final choice of the values should be made only after the results seem to be satisfactory. In that regard, it was concluded that the values calculated from the DIANA proposal seemed to be too low, and continued to use the stiff bond parameters used in Part I, where $k_{n,s} = 1 \cdot 10^6$ N/mm$^3$ and $k_{t,s} = 1 \cdot 10^5$ N/mm$^3$. The analyses with the calculated guideline stiffness parameters were performed and can be found in Section J of the Appendix.

## 10.3 Prestress control

After performing the parametric study, the response of the bridge with only the prestressing load could be studied and compared to analytical calculations, which can be found in Appendix I.2. As the analysis should represent the tensioning phase, an analysis with one load step was created. The interface material parameters were $k_{n,w} = 1$ N/mm$^3$ and $k_{t,w} = 0{,}001$ N/mm$^3$ as found in the parametric study. The loads applied were the prestressing force $P$ on the tendons and the reaction forces $R$ on the anchorages. The displacements are presented in Figure 75, while the moment diagram is presented in Figure 76. A comparison between the numerical results and the analytical results is presented in Table 19.

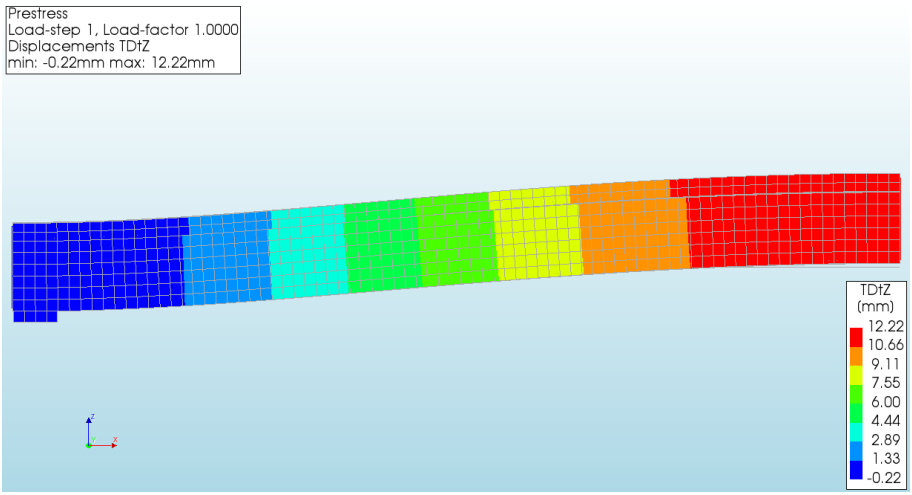


Figure 75: Vertical displacements of the bridge model after applying only prestress forces

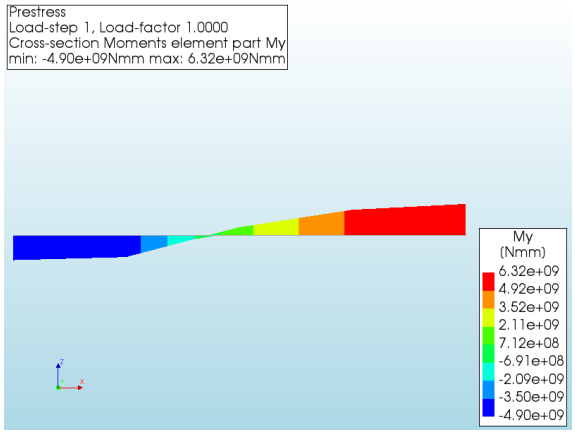


Figure 76: Moment diagram from the prestress control

| | $M_y$ **over support** $[kNm]$ | $M_y$ **at midspan** $[kNm]$ | **Max. deflection** $d_z[mm]$ |
|---|---|---|---|
| **Analytical calculations** | - 7672 | 6239 | -10,7 |
| **DIANA** | - 4898,9 | 6322,8 | - 12,22 |
| **Difference** | - 36,1 % | + 1,3% | + 14,2% |

Table 19: Comparison of analytical and numerical results for the prestress control

Similarly to the results found in Chapter 10.1, the bending moment over the support is lower in the results from DIANA. Again, this can be partly explained by the neglect of the width of the support.

## 10.4 Non-linear behaviour

After the initial control of each load, the bridge model was loaded until failure by applying a gradually increasing traffic load. This way the non-linear behaviour of the bridge, as well as the difference in response between the grouted and ungrouted model, could be studied. Three analyses were created. One for the grouted model, one for the ungrouted model and one where the tendons were modelled as embedded reinforcements. The stiffness parameters used in the grouted and ungrouted bridge analyses are shown in Table 20.

| **Phase** | **Ungrouted tendons** | **Grouted tendons** |
|---|---|---|
| Tensioning phase | $k_{t,w} = 0{,}001$, $k_{n,w} = 1$ | $k_{t,w} = 0{,}001$, $k_{n,w} = 1$ |
| Loading phase | $k_{t,w} = 0{,}001$, $k_{n,w} = 1$ | $k_{t,s} = 1{\cdot}10^5$, $k_{n,s} = 1{\cdot}10^6$ |

Table 20: Overview of the choice of shear stiffness parameters for the ungrouted and the grouted bridge model, during the two phases of the analysis. Units are in N/mm$^3$

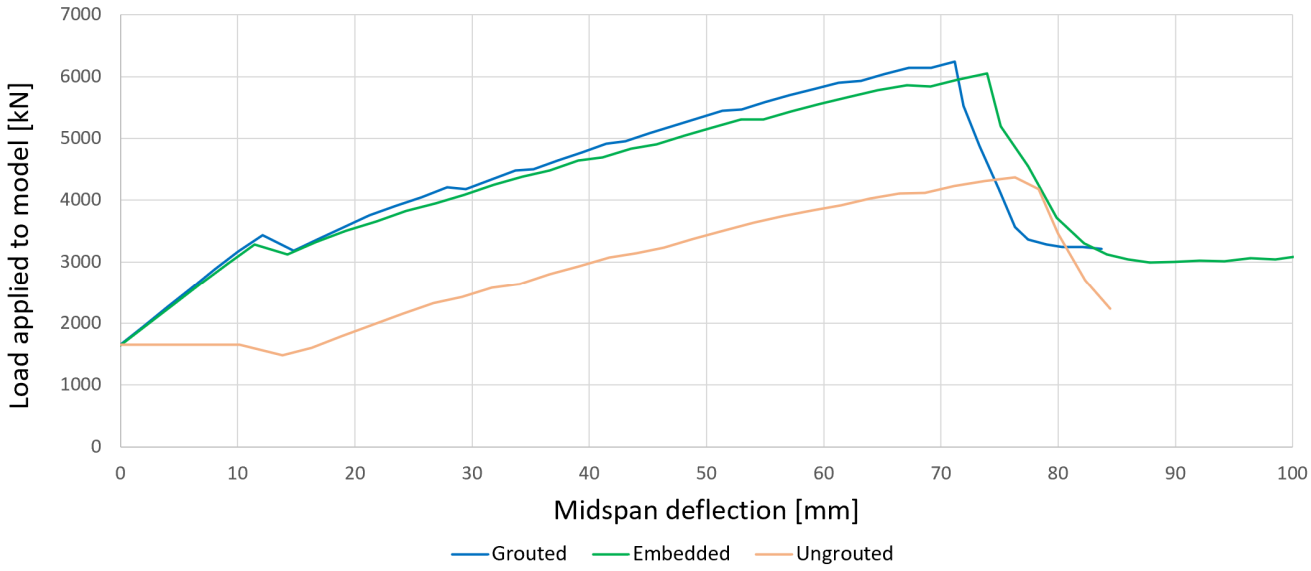


Figure 77: Results from the initial non-linear analysis on the bridge model

Figure 77 is a presentation of the first attempt at loading the bridge model until failure. It can be observed that analyses in Figure 77 starts with an initial load of 1650 kN. This represents the applied self weight. The linear area for the ungrouted model does not coincide with the two other results. The applied load seems to remain constant while the midspan deflections are increasing. The incorrect behaviour of the ungrouted model could be explained by studying the tensioning force along the tendon. The ungrouted model lost nearly all of its prestressing force in the start step of the second phase of the analysis. As presented in Figure 78, the prestressing force in the first phase was 1820 kN and 1720 kN for the anchoring point and midspan, respectively, while it was 1 kN and 0.002 kN in the start step of the second phase. This loss of prestress caused the model to get an unnaturally big downward deflection at midspan as the upward deflection disappeared in the start step. This result was not in agreement with the load-deflection curves from Part I of this thesis, which showed a minimal difference between the grouted and ungrouted tendons.

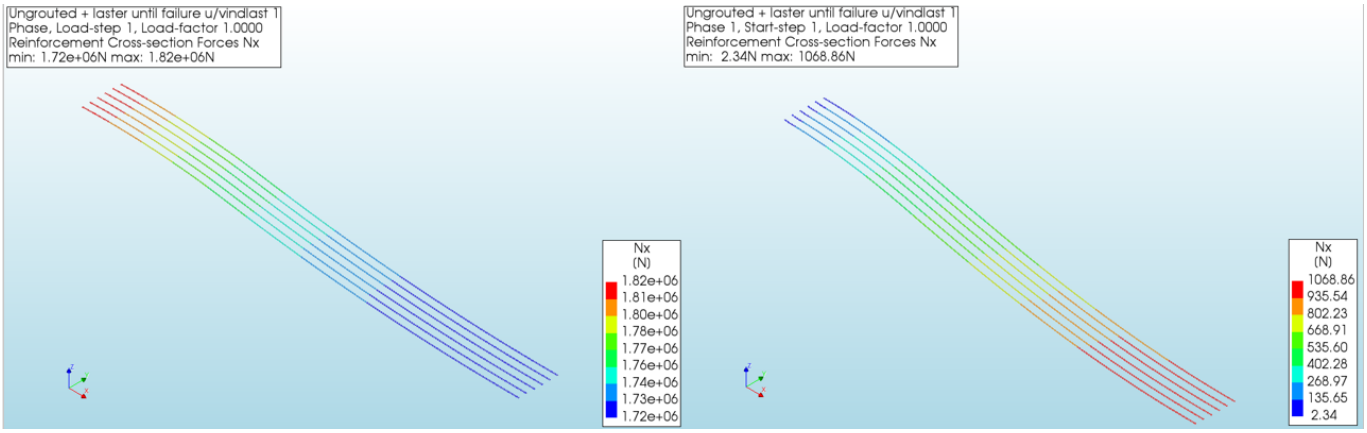


Figure 78: Prestress loss in the ungrouted tendons. Right: Load step 1 of phase 1, Left:Start step of phase 2

After controlling tyings and boundary conditions in the ungrouted model, it was decided to make a new model where the ends of the tendons were grouted. It was believed that the grouted parts would keep the prestress in the tendon, while the ungrouted part was still big enough to represent the behaviour of an ungrouted bridge. By using the *split wire* function in DIANA, a new model with ungrouted tendons was made as shown in Figure 79. The tendons were split 300 mm from each end. As this left 96% (15,4 m) of the tendon ungrouted, it was argued that the model could still represent ungrouted behaviour. The 300 mm parts over the support and at midspan were modelled with grouted properties, using the stiffness parameters presented in Table 20. The middle part of the reinforcement was modelled with weak stiffness parameters in both phases of the analysis. As presented in Figure 80, there was now no change in prestress between the two phases, so this configuration seemed to solve the problem.

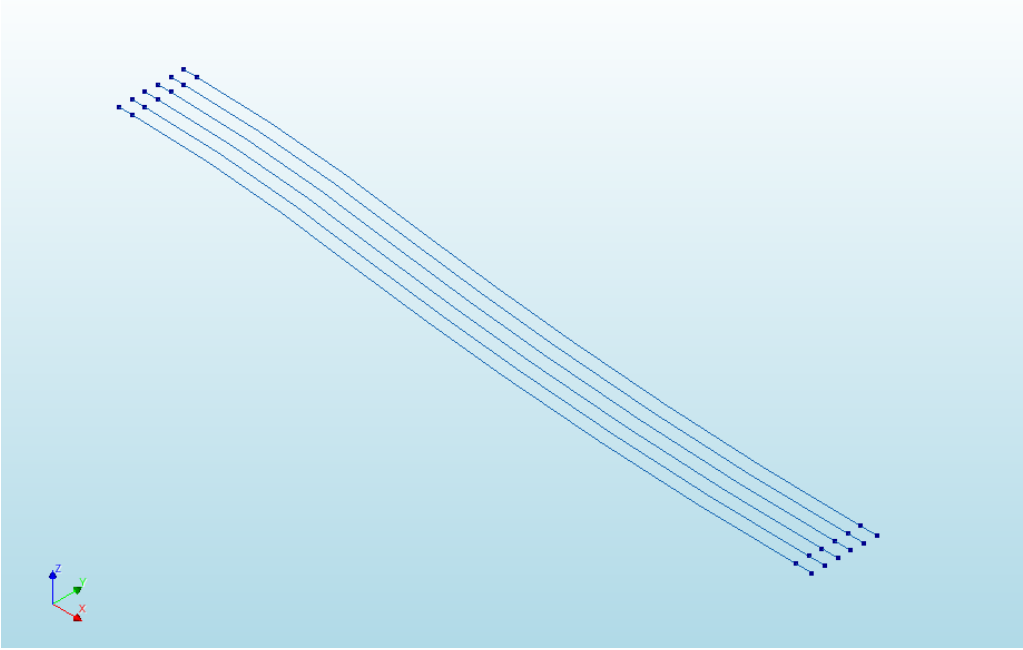

Figure 79: Reinforcement with grouted ends after using the *split wire* function

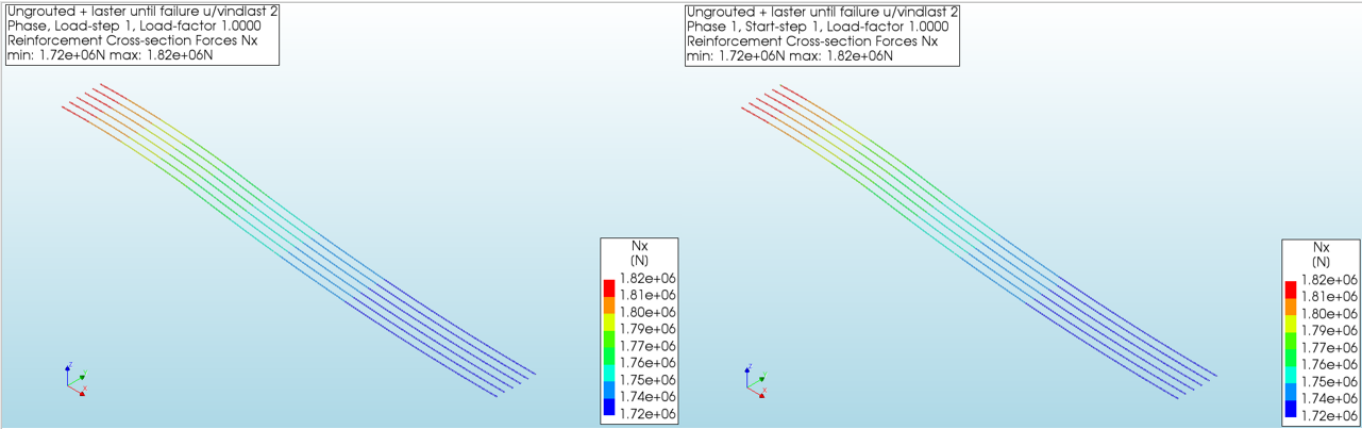


Figure 80: Prestress loss in ungrouted tendons, after modelling grout at the far ends of the tendon.
Right: Load step 1 of phase 1, Left: Start step of phase 2

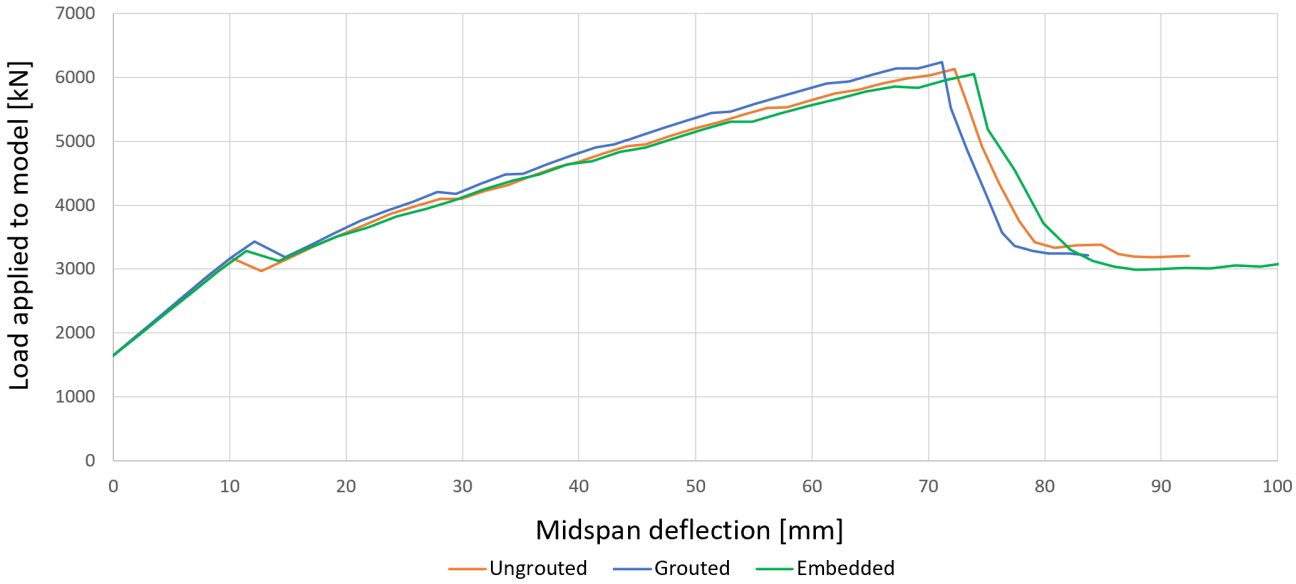


Figure 81: Final results from the non-linear analysis on the bridge model

The load-deflection curves for the different bridge models are presented in Figure 81. Similarly to the results from Part I of this thesis, the ungrouted and grouted models have equal linear behaviour. The cracking load for the ungrouted bridge model was found to be 3174 kN, while the cracking load for the grouted model was slightly higher at 3432 kN. The points of cracking are noticeable peaks in the load-deflection curves. The ultimate load capacity for the grouted bridge was also slightly higher than for the ungrouted bridge, with the ultimate loads being 6242 kN and 6129 kN, respectively. This corresponds to approximately eight times the design traffic load. In reality, this should have been lower as a mistake was made when the traffic loads were applied, as explained in the previous chapter. The maximum deflection is observed to be somewhat higher in the ungrouted bridge model, where the deflection at midspan is 72 mm for the ultimate load, while it is 71 mm for the grouted bridge model.

When comparing the bond-slip models to a model where the tendons were defined as embedded reinforcement, the embedded model had the lowest capacity. In an idealized situation, the results from the grouted model would perfectly coincide with the embedded model and the ungrouted model would have a slightly lower capacity, as they both represent a perfect bond. However, as experienced throughout this thesis, the size of the mesh and the size of the stiffness parameters will greatly affect the results. Here, it was concluded that even though the results could have been slightly altered, the difference in structural response between the grouted and ungrouted model is clear. Moreover, the difference between the embedded results and the grouted results is small. It is believed that the results could have been further improved by running the analyses with a finer mesh, but the computational equipment required for these analyses were not available.

Figure 82 and Figure 83 shows the crack distribution for the grouted and ungrouted bridge model at the point of their ultimate load. The cracks appearing at the bottom edge of the bridge beam were compared. The two models are almost equally loaded, but it can be observed that the cracks in the grouted model are finer and

more evenly distributed. As in Part I of this thesis, the ungrouted model seem to have slightly bigger and more grouped cracks. There are also cracks appearing underneath the concrete slab and over the support, because these areas will also have tensile stresses during a high loading level.

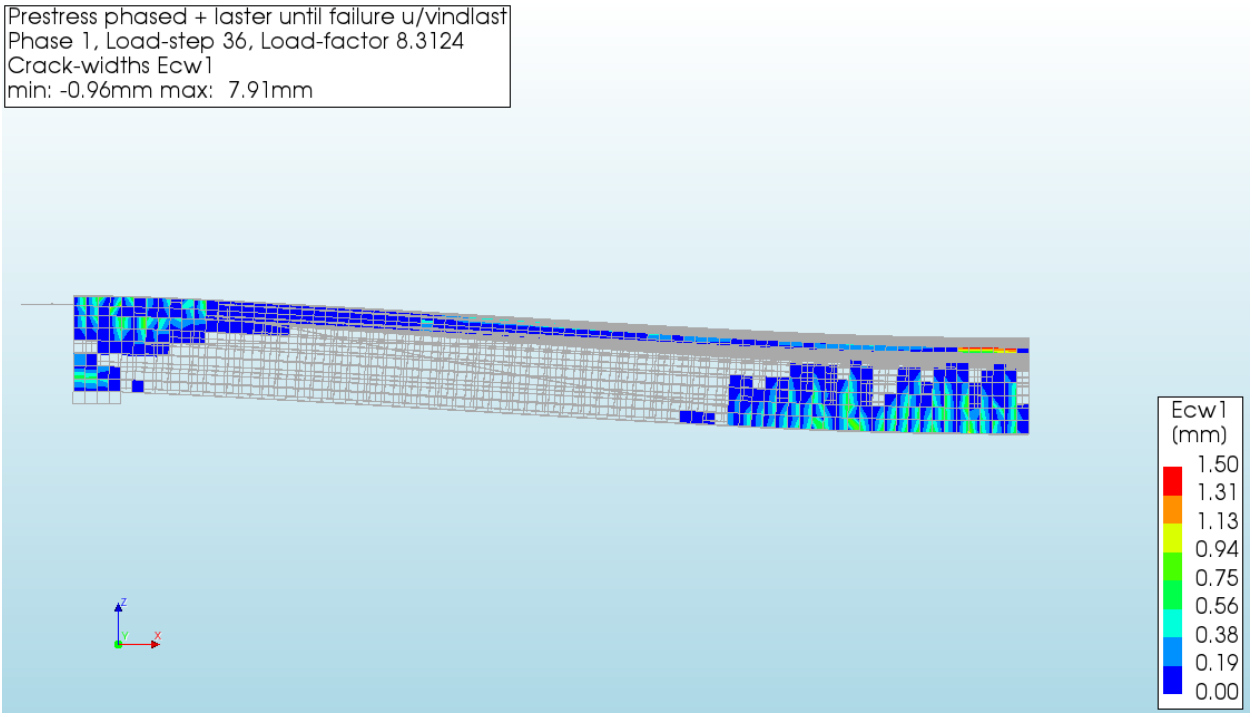


Figure 82: Cracking pattern of the grouted bridge model at failure

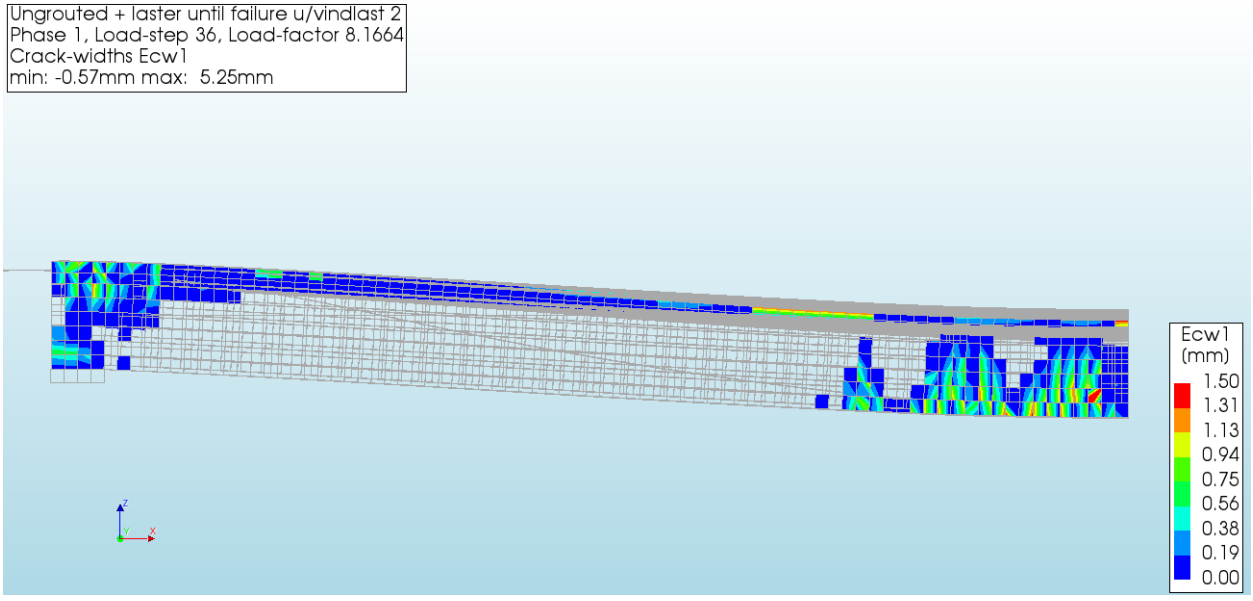


Figure 83: Cracking pattern of the ungrouted bridge model at failure

# 11 Discussion

In Part I and Part II, results from the non-linear finite element analyses were presented, along with the results from the parametric studies to find the appropriate stiffness parameters of the reinforcement interface elements.

In this final discussion, the obtained results from both the beam model and the bridge model are evaluated, followed by a comparison of the the two parts. The sources of error and accuracy of the obtained results are discussed, as well as the general experience with DIANA during the thesis work.

## 11.1 Discussion of Part I; Post-tensioned beam with lack of grouting

The beam models were created with the intention of recreating the experimental results that were reported in three research papers. However, it was discovered that recreating experiments with a non-linear analysis is quite challenging. This task gets even more complicated when the experiments are performed by an external party, as there is a considerable risk of misinterpreting the reported method and results. This was observed for the PT1 model; Even though many hours were spent making and re-making the model and changing the input variables, the recreation of the load-deflection curve remained unsuccessful.

For PT2, there was a much better match between the numerical results, the analytical results, and the experiment. This beam was therefore used for the parametric study and a comparison between the structural responses of a grouted and an ungrouted beam. As previously discussed, the modelled ungrouted beam did not display the same behaviour as the reported unbonded beam. Specifically, the ultimate load capacity reported in the experiment is close to the numerical model using embedded reinforcements, while the ungrouted models showed a consistently lower load capacity than the results reported in the experiment. One reason for this could be that even though there is no grout present in the duct, there is still friction appearing between the tendon and the surrounding concrete. The exact set-up of the experiment is not reported, for example whether the duct was coated with grease to create lower friction of the tendon surface.

The research paper by Lei Wang Et Al. [24] was an important starting point for the work with this thesis. As it reports that the level of grouting in a post-tensioned beam has a significant impact on its structural behaviour, this became a motive for the aim of the thesis. More precisely, the reported experiment gave a 23,8 % reduction of the ultimate load capacity for an ungrouted beam compared to a fully grouted beam. In addition, Lei Wang Et Al. reported a large difference in the cracking widths when comparing the two situations. Even if the PT1 beam was not successfully recreated, one should expect to see a quite similar behaviour for PT2, as these two experiments are very much alike. However, the difference between the grouted and the ungrouted beam models was considerably lower. The ungrouted beam models had a 7,6 % lower ultimate load capacity, and the crack widths were nearly indistinguishable. The analytical calculations on PT2 were closer to this value, with a reduction of 5,5%.

## 11.2 Discussion of Part II; Post-tensioned beam bridge with lack of grouting

In Part II of this thesis, the span of a generic beam bridge was modelled. Although this model was simplified with respect to the geometry, the boundary conditions and the loading configurations, it can still be argued that the results are representative and that they give some indications on the grouted and ungrouted behaviour.

For the loading configuration on the model, it was decided to only include the self weight and the vertical traffic load, in addition to the post-tensioning load. This was because the other loads that are included during the dimensioning of a bridge are normally less prominent. For the purpose of this thesis, which was to study the non-linear behaviour and thereby increase the load to the point of failure, it was deemed sufficient to look at the self weight and traffic load. The size of the loads was about eight times higher than the design traffic load of the bridge. It should however be stressed that the light traffic load that was applied to the bridge was reduced by 50% compared to the recommended value. However, the heavy traffic load and the point loads are the most significant, and the results from the analysis will still indicate the non-linear behaviour of a bridge of this type.

With the experience that was gained from the beam models, the modelling of the beam bridge became much less challenging than it would have been if it had been modelled right away. Many of the findings from the beam models were directly applicable to the bridge model; The chosen material models and analysis methods could be used for both cases. However, it was discovered that the reinforcement interface stiffness parameters that gave the best results for the beam models were unsuitable for the bridge model. According to DIANA FEA BV's recommandations [31], the stiffnesses are sensitive to the mesh size, which were significantly larger for the bridge model, as this is a model with much bigger dimensions. Another reason why the stiffness parameters had to be changed was because the tendons of the bridge model, opposing to the beam models, had a parabolic shape. The parabolic shape meant that the bonding of the tendons was also affected by the normal stiffness of the interface, $k_n$. To summarize, the choice of reinforcement interface stiffness should be evaluated independently for each DIANA model.

The load capacity of the grouted and ungrouted bridge model were both higher than the model with embedded reinforcements. This implies that the load capacity in reality should be lower, given that the embedded model represents a perfect bond. This could probably be shown by reducing the mesh size in the bridge models and further adapt the stiffness parameters. However, such analyses would be easier to perform on a more powerful computer, and it was argued that the difference between the grouted and ungrouted situation was clear.

## 11.3 Summary and comparison of Part I and Part II

Generally, both the beam models and the bridge model showed a good agreement when the analytical and numerical results were compared. From this, it can be concluded that the modelling and analysis method of the models seemed to give sufficiently representative and trustworthy results, bearing in mind the limits both in time and computational power.

The results from the cracking patterns when the structure is close to failure is slightly different between the grouted and the ungrouted case. It seems that the cracks are more evenly distributed for the grouted case, while for the ungrouted structures, the cracks are assembled in groups. More concentrated cracks will leave the reinforcement more exposed, which can lead to corrosion. To further investigate and confirm these results, a finer mesh is needed, as well as smaller step sizes when the external load is applied. This would require higher computational power and storage. However, it is doubtful that the differences in cracking pattern and crack widths are sufficient to be used during an inspection of a bridge to investigate problems with lack of grouting.

The two modelling methods for post-tensioned systems in DIANA, embedded reinforcements and bond-slip reinforcements, are different in many ways. The embedded reinforcements are the most user friendly, as the wobble parameter and Coulomb friction parameters are direct input values in the program. When modelling with bond-slip reinforcement, it is important that the user knows how the interface material properties should be chosen to ensure that the model is correct. The relation between the properties of the interface and the resulting friction and loss of prestress is very complex and requires some experience to be mastered. The stiffness parameters seem to directly influence the friction losses, which have a major influence on the behaviour of the beam during the non-linear response. This must be paid attention to while changing the stiffness parameters. Even though DIANA FEA BV provides some advice for the choice of stiffness parameters on an interface, these recommendations are unspecific and not necessarily correct for the model in question. Nevertheless, the advantage of the bond-slip reinforcements is that any level of bonding of the tendons can be modelled, giving the user control and more possibilities. For the embedded reinforcement, there is no other options than a complete bonding or no bonding at all.

Some general experiences with non-linear analyses in DIANA were gained during the thesis work. First of all, it was observed that the first part of the analysis, where the materials still have a linear elastic behaviour, is much more precise than the non-linear part of the analysis. This is to be expected, as the non-linear behaviour in this part requires a more complex computation, which will increase the potential errors and deviations. For the beam models, it was often the case that the analysis did not terminate on its own when the concrete failed due to crushing. Therefore, the point of failure must be found by looking at the stresses or strains in the result file. It is possible that there is a method in DIANA that will terminate the analysis when this point is reached, but since examining the results still gave the necessary information, so this was not looked further into. Throughout the thesis work, the Newton-Raphson and the Secant numerical iterative procedures were compared, see Section F of the Appendix). Here, the Newton-Raphson iterations were much more compatible when modelling different levels of grouting using bond-slip reinforcements.

However, the Newton Raphson method is more prone to divergence and seems to require smaller load steps when the external load is applied.

When comparing the beam and the bridge model, it must also be addressed that while plane stress elements were used in the beam, volume elements were used for the bridge model. When modelling in two dimensions, any strain in the out-of-plane direction is neglected. Also, the position of the reinforcement in the out-of-plane direction is not specified. Using volume elements will therefore give more exact results, and the results for a specific cross-section can be viewed in detail. The volume elements will however require a more time-consuming and storage demanding analysis. Since the beam models had a very simple geometry, the plain stress elements were sufficient.

## 11.4 Sources of error and accuracy of results

In the making of the numerical models, it was experienced that it is a difficult task to recreate both analytical and experimental results. The most important reason for this is the many sources of error present during a non-linear finite element analysis.

First of all, DIANA is a complex program where the user can easily make mistakes, and an understanding of the finite element method is demanded. An effort has to be made to make sure that the solutions are viable. There are a great number of options both regarding the model and material definition, as well as the numerical iteration methods. How these parameters influence each other and the outcome of the analysis is difficult to understand fully. The best way of deciding on which method to use is to run several analyses with different settings and then compare the results.

Also, the models are not an exact representation of a real-life structure. The defined geometry, load application and boundary conditions may in reality be irregular and influenced by the surroundings. Moreover, the model material curves are idealized representations of the non-linear behaviour. For the bridge model, the boundary conditions imply a strictly symmetric configuration which would be unlikely for a real bridge.

It should also be mentioned that the analytical calculations used to evaluate the numerical results are not exact predictions of the behaviour of a structure. Some simplifications of the model were made. For example, the application of loads was simplified as either point loads or constant line loads. In the calculation of the response due to traffic load, the complex load configuration was significantly simplified. Also, the contribution of the passive reinforcement of the bridge was not considered.

The element method also has sources of error. When the model is discretized, the element size and the element order will affect the accuracy of the result. In other words, the finite element analysis does not yield exact results but is an estimation with a decided tolerance. By using linear elements without mid-side nodes, the strain of each element is assumed to be constant. If the mesh is too coarse, this might result in a stress field that is not continuous [17]. To increase the accuracy of the results presented in this thesis, the element size could have been further refined, or the elements could have been defined with a higher order.

In addition, the loads could have been applied using smaller load steps. This was not performed because of the limits in computational power and the limited time scope.

When comparing the ultimate load capacity of the grouted and ungrouted bridge model, the difference was found to be 1,8 %. This was not as expected, considering the results from Part I of this thesis, the results from Lei Wang Et Al. [24] and ”Design of Prestressed Concrete to Eurocode 2” [32]. The latter states that the ultimate strength of a beam with unbonded tendons is 25 % lower than a beam with bonded tendons.

# 12 Conclusion

In this thesis, a post-tensioned beam and a span of a post-tensioned beam bridge were successfully modelled. The numerical results were overall reasonable when compared to analytical and experimental results. The non-linear analyses indicate that the structural effects due to lack of grouting are minimal.

In Part I and II, it was attempted to recreate experimental results from four point-bending tests. This turned out to be a complex and time-consuming task but it was a great learning experience that allowed a better transition to the modelling of the more complex bridge structure. By using both embedded reinforcements and the bond-slip reinforcements, it was possible to study the structural effects of insufficient grouting in a post-tensioned system. The results from both models suggest that the concrete member's behaviour is unaffected by the level of grouting until the cracking point. Then, for the non-linear response of the structure, the grouted model seem to have a slightly higher load capacity than an ungrouted case; For the ultimate load capacity, a 7,6% reduction could be observed for the beam models and a 1,8% reduction for the beam models. It was decided not to study partly grouted models, as these two extreme cases showed a very similar behaviour.

The bond-slip modelling in DIANA was used to a large extent as it allows discrete modelling of the interface of the tendons to specify the level of bonding between the tendon and the surrounding concrete. When modelling with bond-slip reinforcements, the Newton-Raphson iteration method was discovered to produce better results than the Secant iteration method. It was found that analyses with linear stiffness interface elements, where the behaviour is defined by the stiffness parameters $k_n$ and $k_t$, gave better results than using the Dörr curve.

Regarding the cracking behaviour of a fully grouted and an ungrouted system, the results until the crack initiation point and crack-width developments were quite similar. However, the results still suggest that there is a difference in cracking pattern between the two cases. While the models with grouted tendons seem to have evenly distributed cracks, the ungrouted model had cracks that were assembled in groups. This tendency could be further studied by refining the mesh. Despite this, it is unlikely that the cracking patterns for the two cases are characteristic enough to be used during a bridge inspection when the level of grouting is evaluated.

To further investigate the structural effects of lack of grouting, it would be interesting to perform an experiment with grouted and ungrouted concrete members. This will give better control of the set-up, results and sources of error. Then, the experiment can be recreated with a numerical model. There are also other options for modelling the reinforcement interface elements in DIANA that have not been looked into in this thesis, for instance by using the Power Law model or the fib Model Code 2010. The structural effect of missing grouting can also be investigated using another finite element program.

# References


[1] NS-EN1992-1-1:2004+A1:2014+NA:2018 *Eurocode 2: Design of concrete structures* Part 1-1*: General rules and rules for buildings*. Standard Norge.

[2] *MANUALS for DIANA FEA*. [Online]. Available: https://dianafea.com/diana-manuals

[3] Statens Vegvesen, *Bedre Bruvedlikehold*, 2017 (accessed June 2, 2021). [Online]. Available: https://www.vegvesen.no/fag/fokusomrader/forskning-innovasjon-og-utvikling/pagaende-programmer-og-prosjekter/bedre-bruvedlikehold/bedre-bruvedlikehold

[4] R. Woodward, "Collapse of a segmental post-tensioned concrete bridge," *Transportation research record*, no. 1211, 1989.

[5] A. H. Nilson, D. Darwin, and C. W. Dolan, *Design of Concrete Structures, 14th Edition*. McGraw-Hill, 2010.

[6] S. I. Sørensen, *Betongkonstruksjoner - Beregning og dimensjonering etter Eurocode 2, 2.utgave*. Fagbokforlaget, 2013.

[7] *Pre-and post tensioning of a concrete beam, DIANA 10.3*. DIANA FEA. Tutorial.

[8] M. P. Collins and D. Mitchell, *Prestressed concrete structures*. Prentice Hall Englewood Cliffs, NJ, 1991, vol. 9.

[9] L. Hangaard and M. Aasheim, "Analyse av ffb-bru med korrosjonsskadet spennarmering-tilstandsvurdering og kapasitetskontroll av osstrupen bru," Master's thesis, NTNU, 2018.

[10] *Publikasjon nr.14 - Spennarmeringsarbeider*. Norsk betongforening, 2016.

[11] P. Gjerp, *Grunnleggende betongteknologi*. BA forlaget, 1998.

[12] H. R. Kvale and T. J. Opheim, "Modellering av etteroppspente betongbruer med korrosjonsskadet spennarmering," Master's thesis, NTNU, 2019.

[13] M. S. Darmawan, "Pitting corrosion model for partial prestressed concrete (pc) structures in a chloride environment," *IPTEK The Journal for Technology and Science*, vol. 20, no. 3, 2009.

[14] G. M. Clark, "Post-tensioned structures–improved standards," *Proceedings of the Institution of Civil Engineers-Forensic Engineering*, vol. 166, no. 4, pp. 171–179, 2013.

[15] S. Kamalakannan, R. Thirunavukkarasu, R. G. Pillai, and M. Santhanam, "Factors affecting the performance characteristics of cementitious grouts for post-tensioning applications," *Construction and Building Materials*, vol. 180, pp. 681–691, 2018.

[16] *Reinforced Concrete Beam: Simulation of an Experimental Test, DIANA 10.5*. DIANA FEA. Tutorial.

[17] M. Hendriks, A. de Boer, and B. Belletti, *Guidelines for Nonlinear Finite Element Analysis of Concrete Structures*. Rijkswaterstaat Centre for Infrastructure, Report RTD:1016-1:2017, 2017.

[18] R. d. Borst, J. J. Remmers, A. Needleman, and M.-A. Abellan, "Discrete vs smeared crack models for concrete fracture: bridging the gap," *International journal for numerical and analytical methods in geomechanics*, vol. 28, no. 7-8, pp. 583–607, 2004.

[19] R. De Borst, M. A. Crisfield, J. J. Remmers, and C. V. Verhoosel, *Nonlinear finite element analysis of solids and structures*. John Wiley & Sons, 2012.

[20] M. Eriksen and M. Kolstad, "Investigation of cracking behavior in reinforced concrete panels with bond-slip reinforcement," Master's thesis, NTNU, 2016.

[21] *Hooke's Law for Plane Stress*, (accessed May 22, 2021), efunda engineering materials. [Online]. Available: https://www.efunda.com/formulae/solid_mechanics/mat_mechanics/hooke_plane_stress.cfm

[22] *Comparison of Nonlinear Finite Element Modeling Tools for Structural Concrete*, 2006 (accessed May 22, 2021), cEE561 Project Sanya Johnson, Illinois Department of Civil and Environmental Engineering College of Engineering. [Online]. Available: https://ibeton.epfl.ch/etudiant/et_doct-11/Courses/2011-11-09%20Sanya%20Johnson%20Report%20on%20Computational%20Tools.pdf

[23] R. Djamaluddin, "Flexural behaviour of external reinforced concrete beams," *Procedia Engineering*, vol. 54, pp. 252–260, 2013.

[24] L. Wang, X. Zhang, J. Zhang, Y. Ma, Y. Xiang, and Y. Liu, "Effect of insufficient grouting and strand corrosion on flexural behavior of pc beams," *Construction and Building Materials*, vol. 53, pp. 213–224, 2014.

[25] N. A. Vu, A. Castel, and R. François, "Response of post-tensioned concrete beams with unbonded tendons including serviceability an ultimate limit state," *Engineering Structures*, vol. 32, pp. 556–569, 2010.

[26] *DIANA Finite Element Analysis Verification Report Release 10.5*, May 9, 2021 (Accessed May 18, 2021), bV. TNO DIANA. [Online]. Available: https://dianafea.com/manuals/d105/Diana.html

[27] Ezzex. Picture of Rollvollbrua. [Online]. Available: https://no.wikipedia.org/wiki/Rossvollbrua#/media/Fil:Rossvollbrua_01.JPG

[28] Statens Vegvesen, *Beregningsveiledning for etteroppspente betongbruer*. Vegdirektoratet, 2017.

[29] . Statens Vegvesen, *Håndbok R412 - Bruklassifisering*. Vegdirektoratet, 2014.

[30] NS-EN 1991-2:2003+NA:2010. *Eurocode 1:* Laster på konstruksjoner *Del 2:* Trafikklast på bruer. Standard Norge.

[31] DIANA FEA BV, *What is the guideline for reasonable choice values of tangent and normal stiffness of tangent and normal stiffness of interface elements?*, 2021 (accessed June 6, 2021). [Online]. Available: https://dianafea.com/faq-tangent-normal-stiffness

[32] R. I. Gilbert, N. C. Mickleborough, and G. Ranzi, *Design of Prestressed Concrete to Eurocode 2,* Second Edition. CRC Press, Taylor Francis Group, 2017.

[33] *The fib Model Code for Concrete Structures 2010*. International Federation for Structural Concrete (*fib*), 2013.

[34] P. Larsen, A. Clausen, and A. Aalberg, *Stålkonstruksjoner, profiler og formler*. Fagbokforlaget, 3. utgave, 5. opplag, 2017.

[35] *Pre-and post tensioning of a concrete beam, DIANA 10.3*. DIANA FEA. Tutorial.

# Appendix

## A Derived concrete material properties

**Concrete tensile strength**

In cases where the concrete tensile strength $f_{ctm}$ is not stated, it can be estimated using the following equations found in EC2, Table 3.1:

$$f_{ck} = f_{cm} - 8MPa$$

$$f_{ctm} = 0.30 \cdot f_{ck}^{\frac{2}{3}}$$

**Concrete fracture values**

The Mode-I tensile fracture energy, $G_f$ and the compressive fracture energy, $G_c$, are necessary input values in DIANA for the chosen concrete stress-strain curves.

The Mode-I tensile fracture energy of concrete $G_f$ [N/m], is in the *fib* model code [33] defined as the energy required for a tensile crack to propagate by a length of 1 m.

The appropriate $G_f$ values are in this thesis calculated based on the compressive strength $f_{cc}$ in MPa using the following equation as recommended in the *fib* model code, equation (5.1-9);

$$G_f = 73 \cdot f_{cc}^{0.18}$$

The compressive fracture energy $G_c$ is a parameter for the energy required before the concrete crushes. This parameter influences the softening branch of the parabolic stress-strain diagram. It can be calculated based on the Mode-I tensile fracture energy [17];

$$G_c = 250 \cdot G_f$$

## B Midspan deflection in four-point bending tests

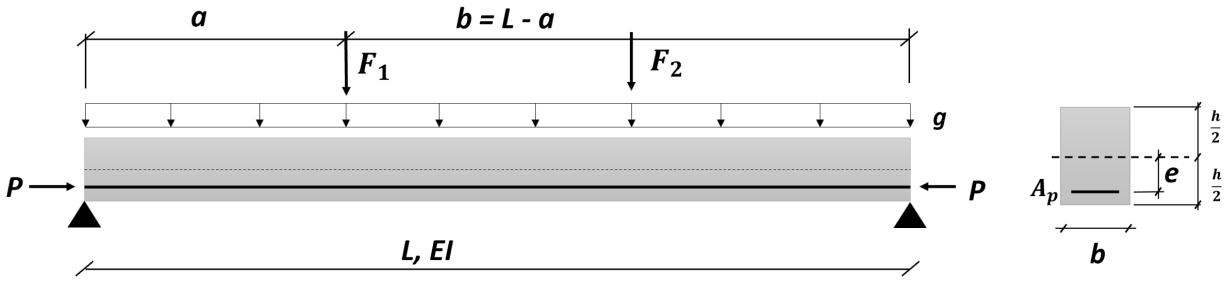


Figure 84: Forces acting on the beam in the four-point beding test

Figure 84 shows a typical set-up for a four-point bending test.There are three types of forces acting on the beam; The self weight *g* which can be regarded as a distributed load, the point loads $F_1$ and $F_2$ from the load cell, and the prestressing force *P*. The prestressing force produces a uniformely distributed axial compressive force *N* and a moment $M_P = N \cdot e$ that occurs because of the eccentricity, *e*.

The upward deflection $\delta_P$ because of the prestressing moment $M_P$, that is constant over the length of the beam, can be calculated using the quick integration table 3.6 in "Stålkonstruksjoner - Profiler og formler" [34]. The virtual moment $\bar{M}(x)$ is found by applying a virtual force with value of 1 on the midspan of the beam. This gives $\bar{M} = \frac{1}{4}L$;

$$\begin{aligned} \delta_P &= \frac{1}{EI}\int_0^L M(x)\bar{M}(x)dx \\ &= \frac{1}{EI}\cdot\frac{1}{2}M\bar{M}L \\ &= \frac{1}{EI}\,\frac{1}{2}(Pe)\,(\frac{1}{4}L)\,L \\ &= \frac{1}{8EI}\,PeL^2 \end{aligned} \tag{15}$$

The deformation $\delta_g$ can be regarded as a distributed load, $g = A \cdot \gamma_c$ where $A_c$ is the beam cross-section area and $\gamma_c$ is the concrete density. The midspan deflection because of self weight is then:

$$\delta_g = \frac{5}{384}\cdot\frac{gL^4}{EI} \tag{16}$$

as in table 3.1 in "Stålkonstruksjoner - Profiler og formler". The deformation $\delta_F$ can be calculated by superposition of the two point loads, so that $\delta_F = 2 \cdot \delta_{F_1}$ ($F_1 = F_2$). Then, this can be found based on the distance *a* as in Figure 84. This equation is found in table 3.1 in "Stålkonstruksjoner - Profiler og formler":

$$\begin{aligned} \delta_F &= 2\cdot\frac{1}{48}\cdot\frac{FL^3}{EI}\left(3\alpha - 4\alpha^3\right) \\ \text{where } \alpha &= \frac{a}{L} \end{aligned} \tag{17}$$

# C Analytical calculations of the RC beam

As the RC beam is an ordinary concrete beam without post-tensioning, it is subjected to pure bending. The point loads $2F$ and the self weight $g$ are considered in the following calculations.

## C.1 Deformations and cracking load of Stage I of the RC Beam

The following calculations and equations are based on page 122 in "Betongkonstruksjoner" [6]. As defined in EC2, a concrete cross-section subjected to small loads will have a linear behaviour with a constant bending stiffness $EI_I$, while the concrete is still uncracked and can sustain tensile forces. The cracking load is the load present when the first cracks develop, which is when the tensile stresses reaches the tensile strength $f_t$. In Stage I, we can treat the reinforced cross section as a transformed cross-section:

$$\begin{aligned} A_t &= A_c + \eta(A_s + A_s') \\ \eta &= \frac{E_s}{E_c} = \frac{210000}{24800} = 8,47 \end{aligned} \tag{18}$$

The moment of the areas about the upper edge of the cross section gives the position of the neutral axis N.A. at the position $\alpha d$:

$$\begin{aligned} A_t\ \alpha d &= A_c \frac{h}{2} + \eta(A_s d + A_s' d') \\ \alpha d &= \frac{A_c \cdot 0,5h + \eta(A_s d + A_s' d')}{A_t} \\ \alpha d &= \frac{(150 \cdot 200) \cdot 0,5 \cdot 200 + 8,47 \cdot (339,3 \cdot 170 + 56,5 \cdot 30)}{150 \cdot 200 + 8,47(339,3 + 56,5)} \\ \alpha d &= 105,0 \ \text{ mm} \end{aligned} \tag{19}$$

The bending stiffness $EI_I$ for Stage I is:

$$\begin{aligned} EI_I &= E_c I_c + E_s I_s + E_s I_s' \\ &= E_c\Big(\frac{bh^3}{12} + (bh)\big(\alpha d - \frac{h}{2}\big)^2\Big) + E_s\Big(A_s(d - \alpha d)^2 + A_s'(\alpha d - d')^2\Big) \\ &= 24800 \cdot 100,7 \cdot 10^6 + 210000\Big(1,43 \cdot 10^6 + 0,32 \cdot 10^6\Big) \\ &= 2,866 \cdot 10^{12} \ \text{ N/mm}^2 \end{aligned}$$

When the bending stiffness is known, the cracking moment,$M_{cr}$ and the corresponding cracking load $F_{cr}$ can be found by the curvature relation:

$$\frac{1}{r} = \frac{M}{EI_I} = \frac{\epsilon_c^u}{(h - \alpha d)}$$

where $\epsilon_c^u$ is the strain at the bottom edge of the concrete cross-section. The cracking moment $M_{cr}$ is defined as to when the stress at this point reaches the tensile capacity $\sigma_c^u = f_{ct}$:

$$\begin{aligned} M_{cr} &= -\frac{\epsilon_c^u \cdot EI_I}{(h - \alpha d)} \\ &= -\frac{\epsilon_c^u \cdot E_c \left(I_c + \eta(I_s + I_s')\right)}{(h - \alpha d)} \\ &= -\frac{f_{ct} \left(I_c + \eta(I_s + I_s')\right)}{(h - \alpha d)} \\ &= -\frac{3,47 \text{ N/mm}^2 \Big(100,7 \cdot 10^6 \text{ mm}^4 + 8,47(1,43 \cdot 10^6 + 0,32 \cdot 10^6) \text{ mm}^4\Big)}{(200 - 105,0) \text{ mm}} \\ &= -4,22 \cdot 10^6 \text{ Nmm} \end{aligned}$$

The moment $M_g$ at midspan due to the concrete self-weight $g$ is:

$$\begin{aligned} M_g &= -\frac{g\, L^2}{8} \\ \text{where } g &= \gamma_c A_c \\ &= 24 \text{ kN/m}^3 \cdot 0,200 \text{ m} \cdot 0,150 \text{ m} = 0,720 \text{ N/mm} \\ \text{which gives } M_g &= -0,563 \cdot 10^6 \text{ N/mm} \end{aligned} \tag{20}$$

The corresponding cracking load $2F_{cr}$ can now be found from the moment caused by this load, which is $M_{F,cr} = M_{cr} - M_g = -4,22 - (-0,563) = -3,66$ kNm . The cracking load of the RC beam is:

$$\begin{aligned} 2F_{cr} &= -2 \cdot \frac{M_{F,cr}}{a} \\ 2F_{cr} &= -2 \cdot \frac{-3,66 \cdot 10^6 \text{ Nmm}}{975 \text{ mm}} \\ 2F_{cr} &= 7508,5 \text{ N} \end{aligned}$$

Here, *a* = 975 mm is the arm of the force *F* as seen in Figure 84.

The linear midspan-deflection development during Stage I can now be found and plotted in the load-deflection curve. The deflection $\delta_g$ caused by self-weight is found to be 0,13 mm by Equation 16.$\delta_F$ is found using Equation 17.

| **Applied load, 2F [kN]** | $\boldsymbol{\delta_F}$ **[mm]** | $\boldsymbol{\delta_{TOT} = \delta_F + \delta_g}$ **[mm]** |
|---:|:---:|:---:|
| 0 | 0 | 0,13 |
| 2 | 0,21 | 34.12 |
| 4 | 0,42 | 0,55 |
| 6 | 0,64 | 0,76 |
| 7,5 kN | 0,80 | 0,92 |

Table 21: Midspan deflection of the RC beam in Stage I

### C.2 Ultimate load capacity of the RC Beam

The following calculations and equations are based on page 35-36 in "Betongkonstruksjoner" [6]. Assuming a pure bending problem and no axial force acting on the concrete, we can calculate the height of the effective concrete compression zone by the equation:

$$\begin{aligned} \Sigma N &= T_c + T_s' - S = 0 \\ Tc &= S - T_s' \\ 0,8\alpha dbf_c &= A_s f_y - A_s' \epsilon_s' E_s \end{aligned} \tag{21}$$

We can assume that the compression reinforcement still hasn't reached its yielding point. Then, the compression force $T_s'$ can be found by the following strain relations:

$$\begin{aligned} \frac{\epsilon_s'}{\epsilon_c} &= \frac{\alpha d - 30}{\alpha d} \\ \epsilon_s' &= \epsilon_c(1 - \frac{30}{\alpha d}) \end{aligned} \tag{22}$$

Combining equation 21 and 22 gives the following quadratic equation of $\alpha d$;

$$\begin{aligned} 0,8\alpha dbf_c &= A_s f_y - A_s' \epsilon_c E_s (1 - \frac{30}{\alpha d}) \\ 0,8(\alpha d)^2 bf_c - (\alpha d)(A_s f_y - A_s' \epsilon_c E_s) - A_s' \epsilon_c E_s \cdot 30 &= 0 \end{aligned} \tag{23}$$

When inserting the values presented in Table 5 in Chapter 6.2, the effective compression height will be $\alpha d = 0,239 \cdot 170$ mm = 40,63 mm .

At the point of failure, the concrete is crushing on the top fibre, where $\epsilon_c$= 3,5 ‰. The strain of the compression reinforcement is found based on Equation 22, which gives $\epsilon_s'$ = 0,91 ‰. As this strain is lower than the yielding strain of the reinforcement, $\epsilon_y$= 1,95 ‰, the assumption that the compression steel has not reached yielding was correct. At failure, the resulting forces acting on the cross-section at the midspan are as follows:

$$\begin{aligned} T_c = 0,8\alpha dbf_c &= 0,8 \cdot 40,63 \text{ mm} \cdot 150 \text{ mm} \cdot 26,3 \text{ N/mm}^2 = 128,2 \text{ kN} \\ S = A_s f_y &= 339,3 \text{ mm}^2 \cdot 410 \text{ N/mm}^2 = 139,1 \text{ kN} \\ Ts' = A_s' \epsilon_c (1 - \frac{30}{\alpha d}) E_s &= 56,5 \text{ mm}^2 \cdot 3,5‰ (1 - \frac{30 \text{ mm}}{40,63 \text{ mm}} 210000) = 10,9 \text{ kN} \end{aligned} \tag{24}$$

The calculated forces gives $\Sigma N$ = 0 as predefined. The moment capacity $M_{Rd}$ can be found from the

moment arms about the tensile reinforcement:

$$\begin{aligned} M_{Rd} &= -T_c z - T_s' h' \\ &= -T_c(d - \frac{0,8 \cdot \alpha d}{2}) - T_s'(h - 2 \cdot 30) \\ &= -128,2 \text{ kN} \cdot 153,7 \text{ mm} - 10,9 \text{ kN} \cdot 140 \text{ mm} \\ &= -21,2 \text{ kNm} \end{aligned} \tag{25}$$

The corresponding load capacity $F_{Rd}$ can then be found; $F_{Rd} = -\frac{M_{Rd}}{1,075m} = 39,5$ kN

# D Analytical calculations of the Post-tensioned beam 1

The hand-calculation of the post-tensioned beam can be done in a similar manner as for an ordinary reinforced beam, as long as the effects from the post-tensioning beam is included; The additional axial compression of the cross section $N = -P$ and the additional moment $M = -Pe$ causing an initial upward deflection $\delta_P$. The beam is regarded as a simply supported beam with a span of 1800 mm.

## D.1 Deformations and cracking load in Stage I of PT1

The following calculations and equations are based on page 250-253 in "Betongkonstruksjoner" [6].

The transformed cross-section can be found by including an additional stiffness from the bonded tendon to Equation 18 for the ordinary reinforced beam:

$$\begin{aligned}
\eta_s &= \frac{E_s}{E_c} = \frac{210000}{31793} = 6,61 \\
\eta_p &= \frac{E_p}{E_c} = \frac{195000}{31793} = 6,13 \\
A_t &= A_c + (\eta_s - 1)(A_s + A'_s) + (\eta_p - 1)A_p
\end{aligned}$$

The position of the neutral axis measured from the top of the cross-section, $\alpha d$, can now be found by taking the moment of the areas about the upper edge of the beam as in Equation 19

$$\begin{aligned}
A_t\, \alpha d &= A_c \frac{h}{2} + (\eta_s - 1)\big(A_s d + A'_s d'\big) + (\eta_p - 1)A_p(\frac{h}{2} + e) \\
\alpha d &= \frac{(220 \cdot 150) \cdot 0,5 \cdot 200 + (6,61 - 1)\big(100,53 \cdot 175 + 226,19 \cdot 45\big) + (6,13 - 1)188,69(110 + 50)}{(220 \cdot 150) + (6,61 - 1)(100,53 + 226,19) + (6,13 - 1)188,69} \\
\alpha d &= 110,07 \ \text{ mm}
\end{aligned} \tag{26}$$

It can be observed that $\alpha d$ is very close to the beam centroid, $\frac{h}{2}$ = 110 mm, such that the moment arm of the concrete $A_c$ can be considered as zero. The transformed moment of inertia, $I_t$, can be found by this equation:

$$\begin{aligned}
I_t &= I_c + (\eta_s - 1)(I_s + I'_s) + (\eta_p - 1)I_p \\
\text{where} \quad I_c &= \frac{bh^3}{12} + bh \cdot 0 \quad \text{(no moment arm)} \\
&= \frac{150 \cdot 220^3}{12} = 133,1 \cdot 10^6 \\
I_s &= A_s(d - \alpha d)^2 = 100,53(175 - 110)^2 = 424,7 \cdot 10^3 \ \text{ mm}^4 \\
I'_s &= A'_s(\alpha d - d')^2 = 226,19(110 - 45) = 955,7 \cdot 10^3 \ \text{ mm}^4 \\
I_p &= A_p e^2 = 188,69 \cdot 50^2 = 471,7 \cdot 10^3 \ \text{ mm}^4 \\
\text{which gives} \quad I_t &= 143,26 \cdot 10^6 \ \text{ mm}^4
\end{aligned}$$

The axial force $N$ and the moment in the neutral axis caused by the prestressing are $M_P$ are

$$\begin{aligned} N &= -P = -253.134 \text{ N} \\ M_P &= P \cdot e = 253.134 \text{ N} \cdot 50 \text{ mm} = 12,65 \cdot 10^6 \text{ Nmm} = 12,66 \text{ kNm} \end{aligned} \tag{27}$$

The stress at the bottom edge of the beam, $\sigma_c$ can now be found using Navier Stokes' equation. Here, $y$ is the distance from the neutral axis to the bottom fibre, as found in Equation 26. The cracking moment $M_{cr}$ occurs when the bottom edge reaches a stress level equal to $f_{ct}$

$$\begin{aligned} \sigma_c &= \frac{N}{A_t} + \frac{M}{I_t} \cdot y \\ M_{cr} &= -\frac{I_t}{y}\left(f_{ct} - \frac{N}{A_t}\right) \\ &= -\frac{143,26 \cdot 10^6 \text{ mm}^4}{110 \text{ mm}}\left(2,64 \text{ N/mm}^2 - \frac{-253134 \text{ N}}{35800 \text{ mm}^2}\right) \\ &= -12,64 \cdot 10^6 \text{ Nmm} = -12,64 \text{ kNm} \end{aligned}$$

The moment caused by the applied load from the load cells, $M_{F,cr}$, at the point of cracking, will be $M_{F,cr} = M_{cr} - M_g - M_P = -12,64 - (-0,32) - (12,65) = -24,97$ kNm. Here, $M_g$ is found in a similar manner as in Equation 20. The corresponding cracking load is:

$$\begin{aligned} 2F_{cr} &= -2 \cdot \frac{M_{F,cr}}{a} \\ 2F_{cr} &= -2 \cdot \frac{-24,97 \cdot 10^6 \text{ Nmm}}{600 \text{ mm}} \\ 2F_{cr} &= 83238 \text{ N} \end{aligned}$$

Here, *a* = 600 mm is the arm of the force *F*, the vertical distance from the middle of the support plate to the middle of the load plate.

The linear midspan-deflection development during Stage I is plotted in Table 22, where positive values are defined as downward deflection. The total deflection $\delta_{TOT}$ is the sum of the deflections $\delta_g, \delta_P$ and $\delta_F$ The deflection $\delta_P = -1,05$ mm is found using Equation 15 and $\delta_g$ caused by self-weight is found to be 0,02 mm by Equation 16. $\delta_F$ is found using Equation 17. $\delta'_{TOT}$ is the deflection including the initial upward deflection $= \delta_P + \delta_g$.

| **Applied load, 2F [kN]** | $\boldsymbol{\delta_F}$ **[mm]** | $\boldsymbol{\delta_{TOT}}$ **[mm]** | $\boldsymbol{\delta'_{TOT}}$ **[mm]** |
|---:|:---:|:---:|:---:|
| 0 | 0 | -1,03 | 0 |
| 20 | 0,48 | -0,54 | 0,48 |
| 40 | 0,96 | -0,06 | 0,96 |
| 60 | 1,44 | 0,42 | 1,44 |
| $2F_{cr}$ = 83,2 | 2,00 | 0,98 | 2,00 |

Table 22: Midspan deflection of PT1 in Stage I

### D.2 Ultimate load capacity of PT1

The following calculations and equations are based on pages 277-281 in ”Betongkonstruksjoner” [6] The ultimate load capacity of this beam can be calculated as for the RC beam, by including the resultant forces from the passive reinforcement, $S_s$ and $T'_s$ as well as from the tendon, $S_p$.

To control whether the cross-section is under- or over reinforced, the balanced reinforcement $A_{bal}$ is found by

$$\alpha_{bal} = \frac{\epsilon_{cu}}{\epsilon_{cu} + \Delta\epsilon_p} = \frac{\epsilon_{cu}}{\epsilon_{cu} + (\epsilon_p - \epsilon_{p0}} = \frac{3,5‰}{3,5 + (9,38 - 7,15)‰} = 0,611$$

$$\text{where } \epsilon_p = \frac{f_{p,0,1}}{E_p} = \frac{1830 \text{ N/mm}^2}{195000 \text{ N/mm}^2} = 9,38‰$$

$$\text{and } \epsilon'_{p0} = \frac{N/A_p}{E_p} = \frac{253134 \text{ N}/181,46 \text{ mm}^2}{195000 \text{ N/mm}^2} = 7,15‰$$

$$A_{bal} = \frac{0,8\alpha_{bal} b d f_{cd}}{f_{p,0,1}} = \frac{0,8 \cdot 0,611 \cdot 150 \text{ mm} \cdot 160 \text{ mm} \cdot 34,12 \text{ N/mm}^2}{1830 \text{ N/mm}^2} = 218,6 \text{ mm}^2$$

As the cross-section is under-reinforced, equilibrium can be found for the resultant forces at the failure of the beam

$$\begin{aligned} T_c - S_p - S_s + T'_s &= 0 \\ 0,8\alpha f_{cd} b d - A_p f_{p,0,1} - A_s f_y + A'_s E_s \epsilon'_s &= 0 \qquad (28) \\ \text{where } \epsilon'_s &= \epsilon_c\big(1 - \frac{45}{\alpha d}\big) \text{ (assuming no yielding)} \end{aligned}$$

The compression zone height is found to be $\alpha d = 0,448 \cdot 160$ mm = 71,74 mm. The equation for $\epsilon'_s$ gives a strain of 1,30 ‰. The strain of this reinforcement bar is lower that the yielding strain $\epsilon_y$ of 2 ‰, so the assumption in the previous equation was correct. The passive steel in tension yields as $\epsilon_s$= 5,04 ‰ $> \epsilon_y$.

At failure, the resulting forces acting on the cross-section at the midspan are:

$$T_c = 0,8\alpha d b f_c = 0,8 \cdot 71,74 \text{ mm} \cdot 150 \text{ mm} \cdot 34,12 \text{ N/mm}^2 = 293,7 \text{ kN}$$

$$S_p = A_p f_{p,0,1} = 181,46 \text{ mm}^2 \cdot 1830 \text{ N/mm}^2 = 332,1 \text{ kN}$$

$$S_s = A_s f_y = 100,53 \text{ mm}^2 \cdot 235 \text{ N/mm}^2 = 23,6 \text{ kN}$$

$$T'_s = A'_s E_s \epsilon'_s = 100,53 \text{ mm}^2 \cdot 210000 \cdot 3,5‰(1 - \frac{45 \text{ mm}}{71,74 \text{ mm}}) = 62,0 \text{ kN}$$

As predefined, equilibrium is reached; $T_c - S_p - S_s + T'_s$ = 0. The moment about the upper edge of the beam can be calculated to find the capacity $M_{Rd}$

$$\begin{aligned} M_{Rd} &= T_c \cdot 0,4\alpha d + T'_s \cdot 45 \text{ mm} - S_p \cdot (h - 60) - S_s \cdot (h - 45) \\ &= 293,7 \text{ kN} \cdot 28,70 \text{ mm} + 62,0 \text{ kN} \cdot 45 \text{ mm} - 332,1 \text{ kN} \cdot 160 \text{ mm} - 23,6 \text{ kN} \cdot 175 \text{ mm} \\ &= -46,0 \text{ kNm} \end{aligned}$$

$M_{Rd}$ is a sum of $M_F$, $M_g$ and $M_P$, where the two latter were found in the Stage I calculation. The moment $M_{F,Rd}$ caused by the total load capacity $2F_{Rd}$ can now be found

$$\begin{aligned}
M_{F,Rd} &= M_{Rd} - M_g - M_P \\
&= -46,0 \ \text{kNm} - (-0,32) \ \text{kNm} - 12,7 \ \text{kNm}) \\
&= -58,4 \ \text{kNm} \\
2F_{Rd} &= -2 \cdot \frac{-58,4 \ \text{kNm}}{0,6 \ \text{m}} \\
&= 194,6 \ \text{kN}
\end{aligned}$$

# E Analytical calculations of PT2

The analytical calculations of the PT2 Beam follow the same principles as for the PT1 Beam. The span of PT2 is assumed to be $L$=

## E.1 Deformations and cracking load in Stage I of PT2

The Stage I calculations of the PT2 Beam are calculated based on the equations stated in page 250-253 of "Betongkonstruksjoner" [6]. Considering that the tendon of this beam is unbonded, the strain of this tendon will not affect the bending stiffness $EI_I$ of the concrete beam. In other words, the transformed cross-section $A_t$ will be neglecting the presence of the tendon. However, the prestressing force *P* and the resulting moment $M_P$ must still be considered.

The transformed cross-section can be found using the same equations as for the RC beam, in Equation 18 and Equation 19.

$$\begin{aligned}\eta = \frac{E_s}{E_c} &= \frac{200000}{30000} = 6,66 \\ A_t &= A_c + (\eta - 1)(A_s + A_s') \\ &= 200 \cdot 150 + (6,66 - 1)(56,55 + 56,55) \\ &= 30641 \quad \text{mm}^2\end{aligned}$$

As the passive reinforcement is symmerical in the cross-section of PT2, $\alpha d$ coincides with the centroid of the cross-section. Thus, $\alpha d = \frac{h}{2} = 100$ mm. The second moment of inertia of the transformed cross-section is found to be:

$$\begin{aligned}I_{t,I} &= I_c + (\eta - 1)(I_s + I_s') \\ &= \left(\frac{bh^3}{12}\right) + \left(A_s(d - \alpha d)^2 + A_s'(\alpha d - d')^2\right) \\ &= 100,0 \cdot 10^6 + \left(1,80 \cdot 10^6 + 1,80 \cdot 10^6\right) \\ &= 103,6 \cdot 10^6 \quad \text{mm}^4\end{aligned} \tag{29}$$

where $d$ = 175 mm and $d'$= 25 mm, representing the distance from the upper edge of the beam to the center of the reinforcements.

The cracking moment $M_{cr}$ can be found using the same calculations as for PT1. The axial force $N = -P = -54000$ N, and the moment caused by the prestressing is

$M_P = P \cdot e = 54000 \cdot (100 - 56)) = 2,38$kNm.

$$\begin{aligned} M_{cr} &= -\frac{I_t}{y}\Big(f_{ct} - \frac{N}{A_t}\Big) \\ &= -\frac{103,6 \cdot 10^6}{100}\Big(2,9 - \frac{-54000}{30.641}\Big) \\ &= -4,83 \cdot 10^6 \text{ Nmm} = -4,83 \text{ kNm} \end{aligned}$$

The moment caused by the cracking load $2F_{cr}$ is $M_{F,cr} = M_{cr} - M_g - M_P = -4,83 + 0,68 - 2,38 = -6,53$ kNm. Here, $M_g$ is found in a similar manner as in Equation 20. The corresponding cracking load is

$$\begin{aligned} 2F_{cr} &= -2 \cdot \frac{M_{F,cr}}{a} \\ 2F_{cr} &= -2 \cdot \frac{-6,53 \cdot 10^6 \text{ Nmm}}{800 \text{ mm}} \\ 2F_{cr} &= 16314 \text{ N} \end{aligned}$$

Here, *a* = 800 mm is the arm of the force *F*, the vertical distance from the middle of the support plate to the middle of the load plate.

The linear midspan-deflection development during Stage I is presented in Table 23, where positive values are defined as downward deflection. The total deflection $\delta_{TOT}$ is the sum of the deflections $\delta_g, \delta_P$ and $\delta_F$ The deflection $\delta_P = 0,72$ mm is found using Equation 15 and $\delta_g$ caused by self-weight is found to be 0,17 mm by equation Equation 16.$\delta_F$ is found using Equation 17. $\delta'_{TOT}$ is the deflection including the initial upward deflection $= \delta_P + \delta_g$.

| **Applied load, 2F [kN]** | $\boldsymbol{\delta_F}$ **[mm]** | $\boldsymbol{\delta_{TOT}}$ **[mm]** | $\boldsymbol{\delta'_{TOT}}$ **[mm]** |
|---:|:---:|:---:|:---:|
| 0 | 0 | -0,55 | 0 |
| 4 | 0,43 | -0.12 | 0,43 |
| 8 | 0,86 | 0,31 | 0,86 |
| 12 | 1,30 | 0,75 | 1,30 |
| $2F_{cr}$ = 16,3 | 1,76 | 1,21 | 1,76 |

Table 23: Midspan deflection of PT2 in Stage I

### E.2 Ulitmate load capacity of PT2

The ultimate load capacity of this beam can be calculated as for the RC beam, by including the resultant forces from the passive reinforcement, $S_s$ and $T'_s$ as well as from the tendon, $S_p$. The following equations are found on the pages 277-281 of ”Betongkonstruksjoner” [6].

Equilibrum in a midspan section gives the equation

$$\begin{aligned} T_c - S_p - S_s + T'_s &= 0 \\ 0,8\alpha f_{cd} bd - A_p f_{p,0,1} - f_y A_s + \epsilon'_s E_s A'_s & \\ \text{where} \quad \epsilon'_s = \epsilon_c(1 - \frac{25}{\alpha d}) & \text{ (assuming no yielding)} \end{aligned}$$

The compression zone height is found to be $\alpha d = 0,130 \cdot 144 \text{ mm} = 18,74 \text{ mm}$. The equation for $\epsilon'_s$ gives a strain of -1,17 ‰, as the compressive passive reinforcement is in fact also in tension at the ultimate loading point. The strain of this reinforcement bar is lower that the yielding strain $\epsilon_y$ of 2 ‰, so the assumption in the previous equation was correct. Furthermore, the strain in the tensile reinforcement is $\epsilon_s = 29{,}2$ ‰ $> \epsilon_y$.

At failure, the resulting forces actiong on the cross-section at the midspan are

$$\begin{aligned} T_c &= 0,8\alpha d b f_c = 0,8 \cdot 18,74 \text{ mm} \cdot 150 \text{ mm} \cdot 45 \text{ N/mm}^2 = 101,2kN \\ S_p &= A_p f_{p,0,1} = 50,27 \text{ mm}^2 \cdot 1300 \text{ N/mm}^2 = 65,3 \text{ kN} \\ S_s &= A_s f_y = 55,56 \text{ mm}^2 \cdot 400 \text{ N/mm}^2 = 22,6 \text{ kN} \\ S'_s &= A'_s E_s \epsilon_c (1 - \frac{25}{\alpha d}) = 56,5 \text{ mm}^2 \cdot 200000 \cdot 3,5‰ (1 - \frac{30 \text{ mm}}{40,63 \text{ mm}}) = 13,2 \text{ kN} \end{aligned}$$

As predefined, equilibrum is reached; $T_c - S_p - S_s - S'_s = 0$. The moment about the the tendon can be calculated to find the capacity $M_{Rd}$

$$\begin{aligned} M_{Rd} &= -T_c z - S_s z_s + S'_s z'_s \\ &= -T_c(d - \frac{0,8 \cdot \alpha d}{2}) - S_s(h - d - 25) + S'_s(d - 25) \\ &= -101,2 \text{ kN} \cdot 136,5 \text{ mm} - 13,2 \text{ kN} \cdot 31 \text{ mm} + 10,9 \text{ kN} \cdot 119 \text{ mm} \\ &= -12,9 \text{ kNm} \end{aligned}$$

$M_{Rd}$ is a sum of $M_F$, $M_g$ and $M_P$, where the two latter were found in the Stage I calculation. The moment $M_{F,Rd}$ caused by the total load capacity $2F_{Rd}$ can now be found

$$\begin{aligned} M_{F,Rd} &= M_{Rd} - M_g - M_P \\ &= -12,9 \text{ kNm} - (-0,68 \text{ kNm}) - 2,38 \text{ kNm} \\ &= -14,6 \text{ kNm} \\ 2F_{Rd} &= -2 \cdot \frac{-14,6 \text{ kNm}}{0,8 \text{ m}} \\ &= 36,6 \text{ kN} \end{aligned} \tag{30}$$

### E.3 Reduced ultimate load capacity for PT2 due to undbonded tendons

In Eurocode 2, 5.10.8, it is stated that the reduction of the capacity of an unbonded post-tensioned concrete member may be considered by calculating a reduced stress in the tendon at the ultimate limit state. An increase of the stress from the effective prestress $\sigma_{pm,t}$, to the stress in the ultimate limit state $\sigma_{pud}$ can be estimated to $\Delta\sigma_{p,ULS} = 100$ N/mm$^2$.

For the PT2 model, the stress in the tendon caused by the initial prestressing force $P$ = 54000 N is

$$\sigma_{pm,t} = \frac{P}{A_p} = \frac{54000\,\text{N}}{50,27\,\text{mm}^2} = 1074,2\,\text{N/mm}^2$$

The design stress of the unbonded tendon is therefore

$$\sigma_{pud} = \sigma_{pm,t} + \Delta\sigma_{p,ULS} = 1074,2 + 100 = 1174,2\text{N/mm}^2$$

The ultimate load capacity was re-calculated, using an updated tensile force

$$S_p = \sigma_{pud} \cdot A_p = 1174,2\,\text{N/mm}^2 \cdot 50,27\,\text{mm}^2 = 59027\,\text{N}.$$

This gave a capacity of $2F_{Rd}$ = 34,6 kN for PT2 with unbonded tendons.

# F Choice of bond-slip model and iteration method in DIANA

When modeling bond-slip reinforcements, there are several possible models which can define the shear stiffness parameter. During the analysis of the PT2 beam, two different bond-slip models were applied to compare how they affected the results;

- The linear bond-slip model, where the shear stiffness parameter is defined as a constant $k_t$.
- The Dörr bond-slip model, where the shear stiffness parameter is described by the Cubic bond-slip curve, and is thereby representing a nonlinear relationship between the traction force and the slip of the tendon

In all analyses, the load steps for applying the external load, 2F, was set to 5 kN to limit the calculation time. The geometry, materials and analysis procedure is apart from this similar to what is presented in Chapter 6.4.

Figure 85 shows the difference between the load-deflection curves of the beam using the Linear bond-slip model and the Dörr model, with both grouted and ungrouted conditions. The stiffness parameters, presented in Table 24, were chosen based on the recommended values from a DIANA tutorial [35], and are meant to represent a fully grouted or fully ungrouted state. The iteration method to establish equilibrium for each load step of the analysis was carried out with both Newton-Raphson iterations and Secant (Quasi-Newton) iterations.

| | $k_t$, N/mm$^3$ | c, N/mm$^3$ | $\Delta u$, mm |
|---|---|---|---|
| **Linear model, grouted** | | | |
| Prestressing phase | 1 | - | - |
| Loading phase | 100.000 | - | - |
| **Linear model, ungrouted** | | | |
| Prestressing phase | 1 | - | - |
| Loading phase | 1 | - | - |
| **Dörr model, grouted** | | | |
| Prestressing phase | 100.000 | $1 \cdot 10^{-10}$ | 0,06 |
| Loading phase | 100.000 | 3 | 0,06 |
| **Dörr model, ungrouted** | | | |
| Prestressing phase | 100.000 | $1 \cdot 10^{-10}$ | 0,06 |
| Loading phase | 100.000 | $1 \cdot 10^{-10}$ | 0,06 |

Table 24: Stiffness parameters used to compare the Linear model and the Dörr model

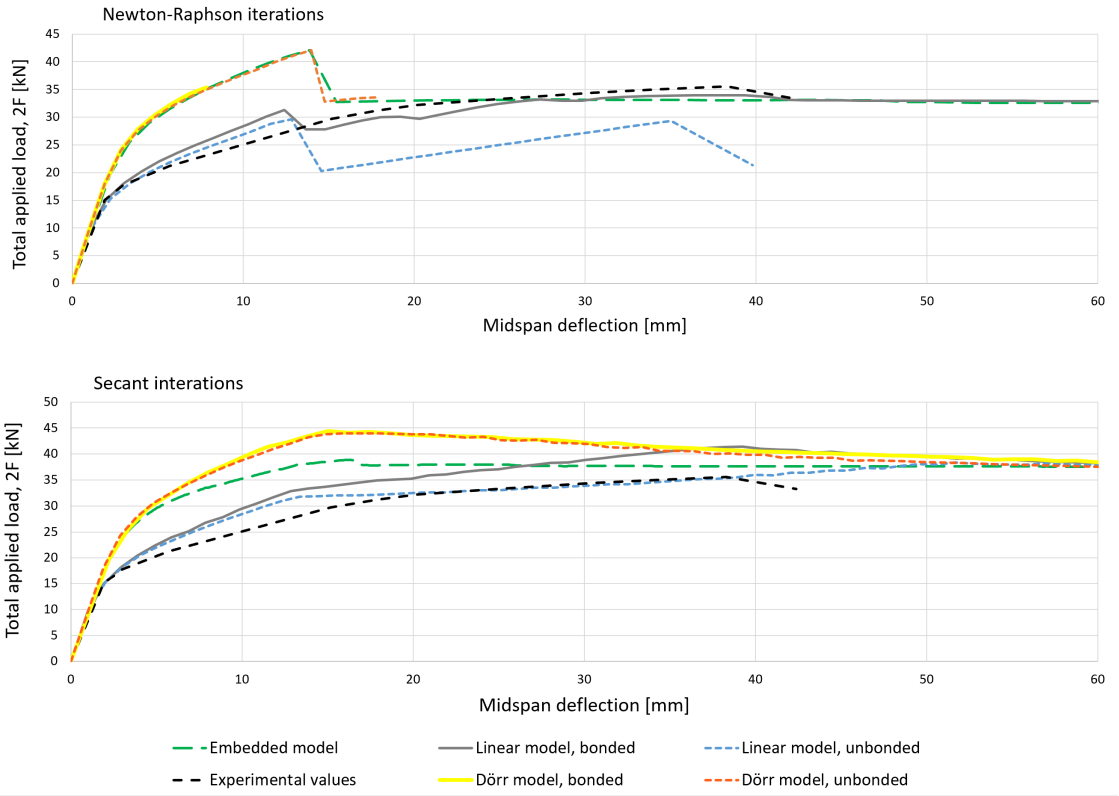


Figure 85: Beam PT2; Load-deflection curves for grouted and ungrouted tendons, using both the Linear model and the Dörr model. The first plot is achieved with Newton-Raphson iterations, while Secant iterations were used in the second plot.

Figure 85 shows that there is a considerable difference between the Newton-Raphson and the Secant iteration methods. The Newton-Raphson method is more sensitive to the yielding of the reinforcement, which creates a noticeable peak in the load-deflection curve. It was also experienced that the Newton-Raphson method easily diverges at early stages of the analysis. The problem with too early divergence can in some cases be solved by using smaller load steps, as explained in Section G. In the secant method, however, the point of yielding of the steel usually does not give a peak in the load-deflection curves, and the numerical calculation seems less prone to divergence.

The Dörr bond-slip model did not give satisfactory results for either of the iteration methods. When the Newton-Raphson method was used, divergence occured too early. With Secant iterations, divergence did not occur, but the beams did not behave as expected. First of all, the behaviour of the grouted and the ungrouted beams were similar, which was not what was expected. Secondly, they both seemed to have a higher load capacity than the model with embedded tendon. As the embedded tendon has a perfectly bonded tendon, these results are not reliable.

The linear bond-slip model gave better results for both iteration methods. Using the Newton-Raphson iterations, the fully grouted bond-slip model is behaving quite differently from the embedded model. Around the yielding point of the tendon (the ”peak” where the midspan deflection is about 10 mm), the embedded model withstands a load of 42,1 kN, while the bond-slip model withstands only 31,1 kN. However, both

models approaches a final load capacity of about 33 kN, which also agrees with the experimental results. The Newton-Raphson iteration method also gave a visibly lower capacity of the ungrouted beam.

To conclude, the Newton-Raphson method gave the best results for the analysis of the PT2 Beam, as the bond-slip models seemed to give a better agreement with the embedded models. The linear bond-slip model is preferred for describing the fully grouted and fully ungrouted beams, as the Dörr bond-slip model easily diverged.

# G Load steps and Arc-length method in DIANA

In this thesis, the nonlinear analyses were performed by applying a gradually increasing external load, $\boldsymbol{f_{ext}}$. To investigate the concept of load steps and arc length control, an analysis performed on the PT2 Beam is used as an example throughout this section. These analyses were performed using the same model and method as described Chapter 6.4. In this example, ungrouted tendons were used, using a linear bond-slip model with a shear stiffness parameter $k_{t,w}$ of 0,3.

In Figure 86a, the load steps are adapted in the *properties* window in the Analysis pane. Here, "Geometry load combination" includes only the external load of $\boldsymbol{f_{ext}} = 2F$= 2 kN, as defined in the model. The size of the increments, the load factor $t$, is defined, as well as the desired number of load steps. For each step, the applied load increases with a value of $t \cdot \boldsymbol{f_{ext}}$[ [2]DIANA 9.6, 11.3.5]. In this case, the user asks for a increment size of $t$=1 for the first 50 load steps, and then an increment size of $t$=5 for the next 200 steps. Figure 86b shows the output values for this analysis for the first 20 steps, along with the vertical displacement of a chosen node at the midspan of the beam. The load-factor shows that the external load $2F$ is increasing with about 2 kN for the first steps.

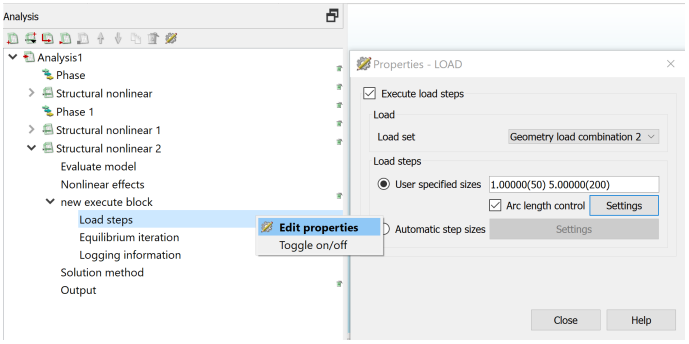


(a) Adapting the load step size and the number of load steps.

| Load-step number | Load-factor *t* | Total applied load *2F = t · 2 kN* | Vertical displacement of node 6831 [mm] |
|---|---|---|---|
| **1** | 1,00 | 2,00 | 0,00 |
| **2** | 1,00 | 2,00 | 0,20 |
| **3** | 2,00 | 4,00 | 0,39 |
| **4** | 3,00 | 6,00 | 0,59 |
| **5** | 4,00 | 8,00 | 0,79 |
| **6** | 4,99 | 9,98 | 0,98 |
| **7** | 5,97 | 11,94 | 1,18 |
| **8** | 6,91 | 13,82 | 1,38 |
| **9** | 7,69 | 15,37 | 1,58 |
| **10** | 8,34 | 16,68 | 1,78 |
| **11** | 8,90 | 17,80 | 1,99 |
| **12** | 9,39 | 18,77 | 2,19 |
| **13** | 9,81 | 19,63 | 2,40 |
| **14** | 10,19 | 20,38 | 2,61 |
| **15** | 10,53 | 21,06 | 2,82 |
| **16** | 10,84 | 21,67 | 3,03 |
| **17** | 11,12 | 22,24 | 3,24 |
| **18** | 11,38 | 22,75 | 3,45 |
| **19** | 11,62 | 23,24 | 3,66 |
| **20** | 11,85 | 23,69 | 3,87 |

(b) Output for a node at the midspan.

Figure 86: Load steps of $t$=1 for the PT2 beam.

The application of the arc length control was also used in the analyses. This method adapts the size of the increment, $t$, by using the displacement of a chosen node in a chosen direction. In this case, Arc length control was established for node 6831, which is located at the midspan of the beam, where the changes in displacements are at the largest. The direction of the arc length control was set to y-direction (vertically), and the parameter $alpha$ was set to -1 as a downward deflection is expected. The arc length control uses the size of the vertical displacement of the control node to modify the applied load $t \cdot \boldsymbol{f_{ext}}$. For instance, in cases where the load-displacement curve is almost flat, the load factor will be reduced to ensure a correct prediction of the further displacements. This can be observed in Figure 86b. In the beginning of the analysis,

the load factor increases with 2 kN at the time, as prescribed. Then, gradually, the load factor decreases to adapt to the displacement of the control node, which increases faster as the load deflection curve becomes less steep.

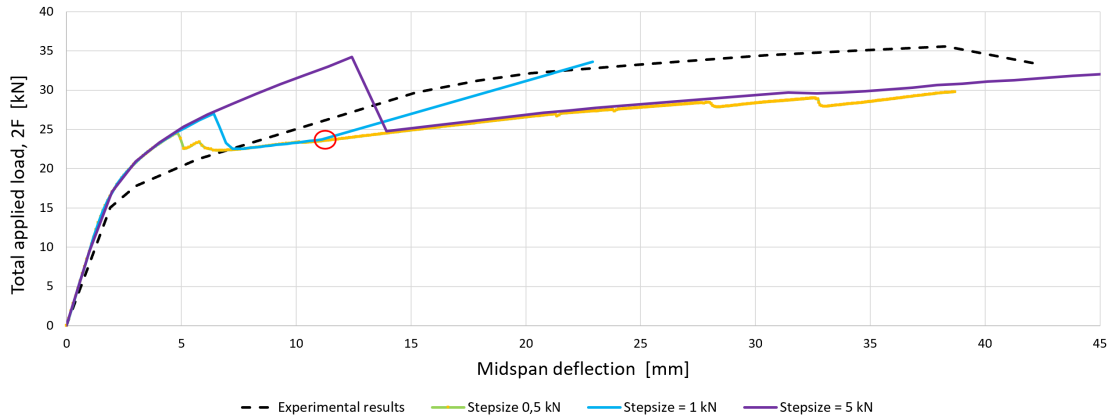


Figure 87: Beam PT2; Load-deflection curves with different step sizes, compared to the reference experiment

For the PT2 Beam, the size of the load steps seemed to greatly affect the result, as can be seen in Figure 87. Here, a step size $t$ of 0,5, 1 and 5 was compared. In other words by the load increased by 1 kN, 2 kN and 10 kN per load step. The arc length control was applied in all cases. In the first part of the analysis, before the cracking load is reached, the load-displacement curves are similar. However, the results start to deffer from each other soon after the nonlinear response is initiated. With a step size of 5, the loads start to increase faster, until it reaches a peak at 34,2 kN, which is where the tendon starts to yield. When the step size is reduced to 0,5 kN, the point of yielding occurs at 24,5 kN, giving a smoother and less noticeable peak. This result is more similar to the experimental results. The effect of reducing the step size, especially in the first part of the nonlinear response, was seen for all cases that were studied in this thesis, regardless of the choice of shear stiffness parameter. DIANA was also sensitive to a change in step size mid-analysis, as seen for the analysis with step size 1. After 50 steps the load factor $t$ was increased from 1 to 5 (Figure 86a), and after step 3, marked with a red circle, the analysis diverges and is terminated automatically.

In nonlinear analyses, the user should therefore choose the step size carefully. A reduced step size is more precise, but is also more time consuming and storage demanding.

# H Recommended values for normal and shear stiffness parameters for reinforcement interface elements

On the DIANA FEA webpage [31], a tentative guideline for the choice of stiffness parameters $k_t$ and $k_n$ for the reinforcement interface elements using a mesh dependent evaluation is provided. In the guildeline, it is clearly emphasized that the method only gives a rough estimation of the values, and that the results must be evaluated by the user to verify whether they are appropriate.

This method takes into account the average element size in the mesh, $l_e$, and an elastic modulus $E$ that is between the values of the surrounding elements. In the case of this thesis, we are considering the interface element of the tendon. $E$ should therefore be between the stiffness of the concrete, which is around 30000 MPa, and the stiffness of the tendon, which is normally 200000 MPa. Therefore, an elastic modulus of $E$ = 100000 MPa seems appropriate for this rough estimation.

## H.1 Recommended values for the Post-tensioned beam 2

Average mesh size; $l_e$= 10 mm Average E-modulus; ≈ 100.000 MPa

| | Maximum $k_t$= $k_n$/10 | Minimum $k_t$=$k_n$/100 |
|---|---|---|
| Minimum, $k_n = 100 \cdot E/l_e = 1 \cdot 10^6$ | $1 \cdot 10^5$ | $1 \cdot 10^4$ |
| Maximum, $k_n = 1000 \cdot E/l_e = 1 \cdot 10^7$ | $1 \cdot 10^6$ | $1 \cdot 10^5$ |

Table 25: Recommended values of $k_t$ and $k_n$ for the PT2. The unit is N/mm$^3$

## H.2 Recommended values for the Bridge model

Average mesh size; $l_e$= 200 mm
Average E-modulus; ≈ 100000 N/mm$^2$ (Considering a concrete stiffness $E_c$= 38000 and a tendon stiffness of $E_p$=195000 N/mm$^2$)

| | Maximum $k_t$= $k_n$/10 | Minimum $k_t$=$k_n$/100 |
|---|---|---|
| Minimum, $k_n = 100 \cdot E/l_e = 5 \cdot 10^4$ | $5 \cdot 10^3$ | $5 \cdot 10^2$ |
| Maximum, $k_n = 1000 \cdot E/l_e = 5 \cdot 10^5$ | $5 \cdot 10^4$ | $5 \cdot 10^3$ |

Table 26: Recommended values of $k_t$ and $k_n$ for the bridge model. The unit is N/mm$^3$

# I Analytical calculations of the Bridge model

## I.1 Properties of the simplified bridge cross-section

| | **Height h** [mm] | **Width b** [mm] | **Area** $A$ [mm$^2$] | $e$ [mm] | $A \cdot e$ | $I_y$ [mm$^4$] | $A \cdot (z_c - e)^2$ |
|---|---|---|---|---|---|---|---|
| **Bridge deck** | 325 | 7300 | 2,373 $\cdot 10^6$ | 162,5 | 3,855 $\cdot 10^8$ | 2,088 $\cdot 10^{10}$ | 3,136 $\cdot 10^{11}$ |
| **Bridge beam** | 1275 | 1550 | 1,976 $\cdot 10^6$ | 962,5 | 1,902 $\cdot 10^9$ | 2,677 $\cdot 10^{11}$ | 3,764 $\cdot 10^{11}$ |
| **Total** | | | 4,349 $\cdot 10^6$ | | 2,288 $\cdot 10^9$ | 2,886 $\cdot 10^{11}$ | 6,900 $\cdot 10^{11}$ |

Table 27: Calculation of second moment of inertia $I_y$ for the simplified beam cross-section

Table 27 shows the properties of the deck and the beam of the Bridge model. The area is found by $A = b \cdot h$ and the second moment of inertia is found by $I_y = \frac{1}{12} b h^3$. The distance $e$ is measured from the top of the deck to centroid of the area $A$. The distance to the neutral axis of the bridge model $z_c$, measured from the top of the deck, is found by:

$$z_c = \frac{\sum(A_i \cdot e_i)}{\sum A_i} = \frac{2,288 \cdot 10^{11}}{4,349 \cdot 10^9} = 526 \text{ mm} \tag{31}$$

The second moment of inertia of the bridge model is:

$$I_y = \sum I_{y,i} + \sum(A_i \cdot (z_c - e_i)^2)) = (2,886 + 6,900) \cdot 10^{11} \text{ mm}^4 = 9,786 \cdot 10^{11} \text{ mm}^4 \tag{32}$$

## I.2 Loads, moments and deformations of the Bridge model

In the following analytical calculations, the Bridge model is considered as a cantilever beam that is clamped in both ends, over the column tops. The following formulas are found in ”Profiler og formler” [34], Table 3.2. Here, the length of the bridge is set as the full span, $L$ = 32000 mm.
The bending stiffness $EI$ = 3,719 $\cdot 10^{16}$ Nmm$^2$ is found by the elastic modulus $E_c$ of B55-concrete and $I_y$ as found in Equation 32.

**Self weight**

The self-weight of the bridge can be considered as a line load $g$ along the span of the bridge;

$$g = \rho_c \cdot A = 24 \frac{\text{kN}}{\text{m}^3} \cdot \frac{1}{1000^3} \cdot \frac{\text{m}^3}{\text{mm}^3} \cdot 4,349 \cdot 10^9 \text{ mm}^2 = 104,4 \frac{\text{N}}{\text{mm}}$$

**Traffic loads**

It was decided to perform the analytical calculations for the traffic load, by using a simplified line load. In the following calculations half of two heavy vehicle loads and their axle loads are taken into account. The load distribution is the same as explained in Chapter 9.5. The sum of the traffic loads in a quarter of a bridge span is:

$$\frac{2 \cdot 500 \text{ kN}}{2} + \frac{2 \cdot 40 \text{ kN}}{2} + 6 \text{ kN}(2m \cdot 8 \text{ m} + 2 \text{ m} \cdot 8 \text{ m} + 0,75 \text{ m} \cdot 16 \text{ m}) = 804 \text{ kN}$$

The traffic load as a simplified line load $q$ distributed over half the length of the bridge span length will then be:

$$q = \frac{804 \cdot 10^3 \text{ N}}{16000 \text{ mm}} = 50.25 \frac{\text{N}}{\text{mm}}$$

The resulting loads, moments and deflections based on the calculated distributed loads $g$ and $q$ are presented in tab:Bridge2.

| | **Reaction force [kN]** | **$M_y$ over support [kNm]** | **$M_y$ at midspan [kNm]** | **Deflection $d_z$ [mm]** |
|---|---|---|---|---|
| **Self weight $g$** | 1669,9 | 8906,2 | -4453,1 | 7,66 |
| **Traffic load $q$** | 804,0 | -4288,0 | 2144,0 | 3,47 |

Table 28: Analytical results for the bridge loaded with self weight and traffic load

**Prestressing force**

The total prestressing force, considering all six tendons, is

$$P_{total} = 6 \cdot 1824 \text{ kN} = 10944 \text{ kN}$$

The analytical calculations for the prestressing of the Bridge model are done as in the example on the pages 232 - 235 in "Betongkonstruksjoner" [6]. The shape of the tendon is considered as two parabolas; One over the support where the tendon is placed above the Neutral axis, and one over the midspan. The two parabolas creates two equivalent distributed loads $q_1$ and $q_2$.

The inflection point between parabolas are located at the neutral axis, at $z_c$ = 526 mm below the upper part of the bridge deck. Using the tendon geometry information found in technical drawing K030-21 in the Attachment, the deflection point is found at a distance $x$=4179 mm from the supported edge of the bridge.

The parabolic shape over the midspan acts over a length of $L_1 = L - 2x = 23648$ mm. The maximum eccentricity $e_1$ is $(h - z_c) - c$ = (1600 - 526) - 140 mm = 934 mm. The equivalent distributed load $q_1$ is

$$q_1 = \frac{8P\, e_1}{L^2} = \frac{8 \cdot 10944 \text{ kN} \cdot 934 \text{ mm}}{(23648 \text{ mm})^2} = 146,2 \frac{\text{N}}{\text{mm}}$$

The parabolic shape over the support has a maximum eccentricity $e_2$ of $z_c - c$ = 526 - 140 mm = 386 mm. The equivalent distributed load is

$$q_2 = \frac{8P\, e_2}{(2x)^2} = \frac{8 \cdot 10944 \text{ kN} \cdot 386 \text{ mm}}{2 \cdot 4179 \text{ mm}^2} = 483,8 \frac{\text{N}}{\text{mm}}$$

To simplify the calculations, we consider the load $q_1 + q_2$ as a concentrated force $R$ acting at a distance $x$/2

from the edge of the bridge.

$$R = (q_1 + q_2) \cdot x = (146,2 \cdot 483,8 \text{ N/mm}) \cdot 4179 \text{ mm} = 2632,8 \text{ kN}$$

The moments because of $q_1$ are

$$M_{1,midspan} = -\frac{q_1 L^2}{24} = \frac{146,2 \cdot 32000^2}{24} = -6239,0 \text{ kNm}$$

$$M_{1,support} = \frac{q_1 L^2}{12} = \frac{146,2 \cdot 32000^2}{12} = 12478 \text{ kNm}$$

As the resultant force is located so close to the support, the moment because of $R$ at midspan can be neglected
The moment at the support is

$$M_{2,support} = R \cdot \frac{x/2 \cdot (L - x/2)^2}{L^2} = 2632,8 \text{ kN} \cdot \frac{2090 \cdot 29910^2}{32000^2} = -4806,3 \text{ kNm}$$

| | **$M_y$ over support [kNm]** | **$M_y$ at midspan [kNm]** | **Deflection $d_z$ [mm]** |
|---|---|---|---|
| **Contribution from equivalent load $q_1$** | -12.478 | 6239 | -10,7 |
| **Contribution from resultant $R$ (from $q_2$)** | 4806 | neglected | neglected |
| **Total** | -7672 | 6239 | -10,7 |

Table 29: Analytical results for the bending moments and deflection because of the equivalent prestressing load

### I.3 Loss of prestress due to friction

Eurocode 2 5.10.5.2.(5.45) The losses of the prestressing force $P$ due to friction can be estimated from:

$$\Delta P_\mu(x) = P_{max}(1 - e^{-\mu(\theta + kx)})$$

This can be rewritten as in ”Betongkonstruksjoner” [6] page 243:

$$P_x = P_{max} e^{-\mu(\theta + kx)}$$

$\mu$ is the coefficient of friction between the tendon and its duct. Recommended value from ”Betongkonstruksjoner” [6] s242: $\mu$= 0,15 - 0,2.
$\theta$ is the sum of the angular displacements over a distance x (irrespective of direction or sign)
k is an unintentional angular displacement for internal tendons (per unit length) which is recommended to be between 0,005 - 0,01 $\text{m}^{-1}$ in Eurocode 2, 5.10.5.2(3).

Sum of angular the angular displacements from the supports to mid span:

$$\begin{aligned}\theta &= \frac{2(e_1 + e_2)}{L/2} \\ &= \frac{2 \cdot (0,934\text{ m} + 0,386\text{ m})}{16\text{ m}} \\ &= 0,165 \text{ radians}\end{aligned}$$

Assuming $\mu$ = 0,2 and k = 0,01$m^{-1}$ the maximum losses due to friction at midspan can be calculated:

$$\begin{aligned}P_x &= P_{max}e^{-\mu(\theta+kx)} \\ &= 1824\text{ kN} \cdot e^{-0,2(0,165+0,01\cdot 16)} \\ &= 1709\text{ kN } or\ 0,937P_{max}\end{aligned}$$

Assuming $\mu$ = 0,15 and k = 0,005$m^{-1}$ the minimum losses due to friction at mid span can be calculated:

$$\begin{aligned}P_x &= P_{max}e^{-\mu(\theta+kx)} \\ &= 1824\text{ kN} \cdot e^{-0,15(0,165+0,005\cdot 16)} \\ &= 1758\text{ kN } or\ 0,964P_{max}\end{aligned}$$

The prestress loss due to friction should therefore be between 3,6% and 6,3%.

# J Recommended stiffness parameters for the Bridge model

The following results are from analyses on the bridge model using the calculated stiffness parameters found in Section H.2.

## J.1 Minimum recommended values

The results from the analysis on the bridge model with the minimum recommended stiffness parameters from DIANA are presented in Figure 88. It can be observed that the grouted model did not reach its ultimate capacity. This is because the model diverged.

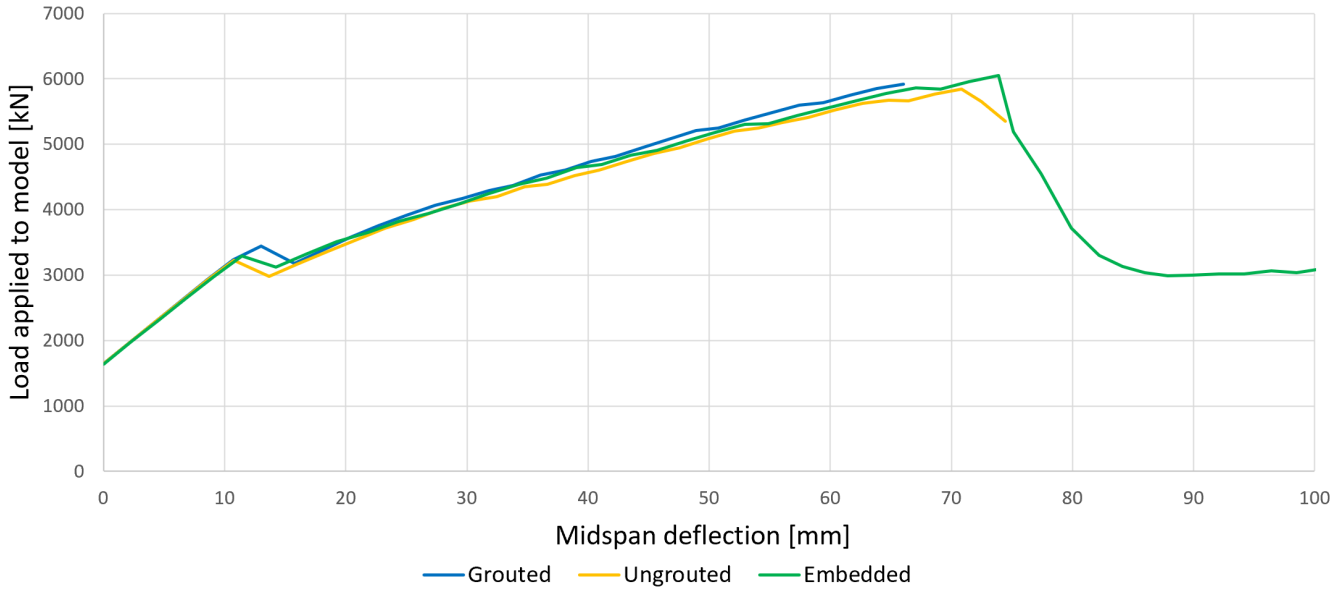


Figure 88: Results from bridge analysis with minimum recommended stiffness parameters

## J.2 Maximum recommended values

The results from the analysis on the bridge model with the maximum recommended stiffness parameters from DIANA is presented in Figure 89. As can be observed, the different models exhibit a similar behavior both in the linear and the non-linear area. Contrary to what is expected, it can be seen that the grouted model has a slightly lower ultimate load capacity than the ungrouted model, but the deflection is larger for the ungrouted model when the capacity is reached.

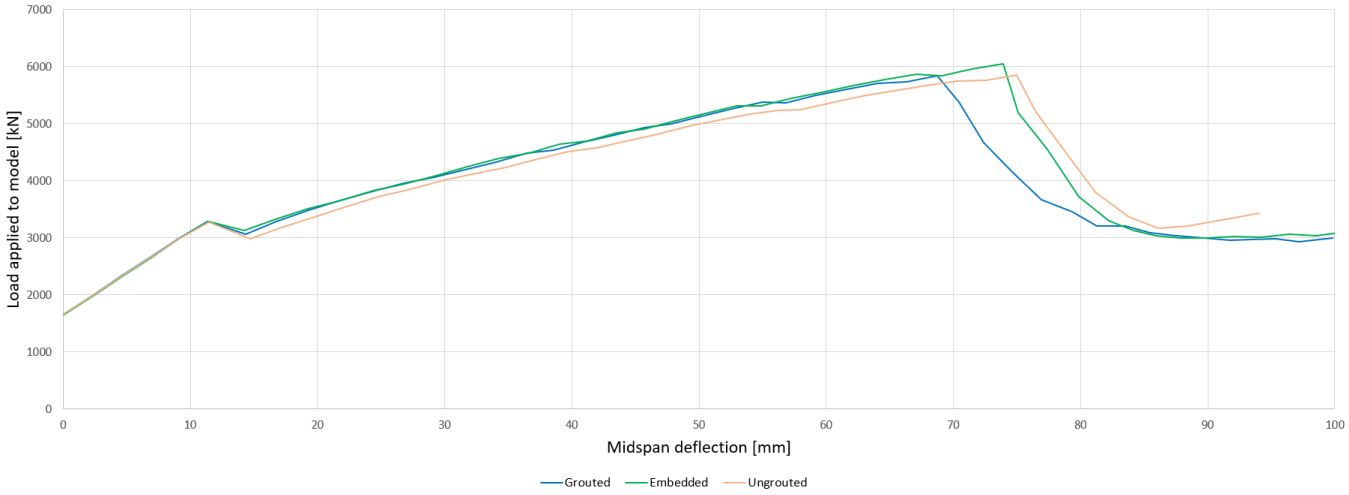


Figure 89: Results from bridge analysis with maximum recommended stiffness parameters

# Attachments

## List of Attachments

Attached to this document, the following documentation from Rossvollbrua is added. These drawings have been found in Statens Vegvesen's database BRUTUS.

**K030 - 01;** Overview of Rossvollbrua, topology

**K030 - 15;** Shape of bridge beam, cross-section

**K030 - 17;** Passive reinforcement of bridge beam, cross-section

**K030 - 18;** Passive reinforcement of concrete deck

**K030 - 21;** Shape of tendons between support 2 and 4

**K030 - 22;** Shape of tendons between support 1 and 2

Active road line is 11500

| | | | | | | | | | | | | | |
|---|---|---|---|---|---|---|---|---|---|---|---|---|---|
| PROFILNUMMER | 13390 | 13400 | 13410 | 13420 | 13430 | 13440 | 13450 | 13460 | 13470 | 13480 | 13490 | 13500 | 13510 |
| PROFILHØYDE | 16.037 | 15.809 | 15.601 | 15.412 | 15.244 | 15.096 | 14.967 | 14.859 | 14.771 | 14.702 | 14.654 | 14.626 | 14.618 |
| TERRENGHØYDE | 13 54 | 9 48 | 8 81 | 8 15 | 11 45 | 12 66 | 4 01 | 2 07 | 2 14 | 2 92 | 6 12 | 6 92 | 6 89 |
| VERTIKALKURVE | R = 5000 m | | | | | | | | | | | | |
| HORISONTALKURVE | A = 464.42 | | | | | | | | | | | | |

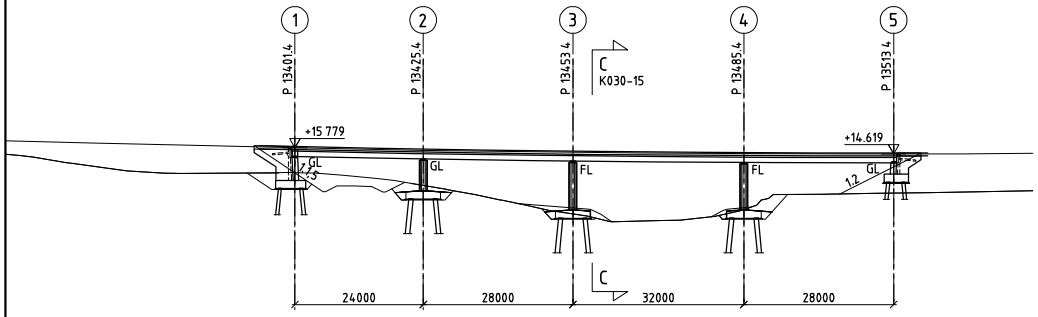


A OPPRISS
1500

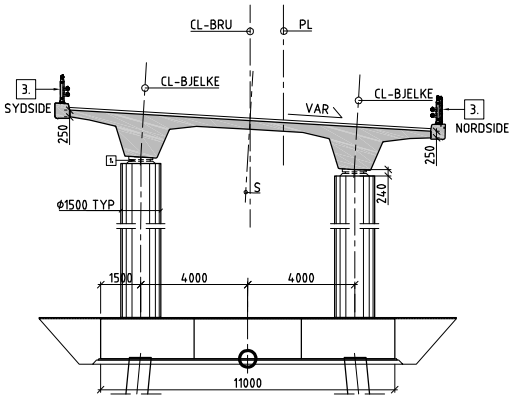


C SNITT
1:100

BEMERKNINGER

1. FELTVIS UTBYGGING FRA AKSE 5
2. FL = FASTLAGER AKSE 3 OG 4
   GL = SIDESTYRTE GLIDELAGER I AKSE 2
   1 STK SIDESTYRT OG 1 STK ALLSIDIG GLIDELAGER I AKSE 1 OG 5
3. REKKVERK SE TEGNING K030-27 SAMT EGNE REKKVERKSTEGNINGER FRA ØRSTA STÅL.
4. BRUA ER DIMENSJONERT FOR 100mm SLITELAG
5. FORSKALING:

   BRUOVERBYGNING — HORISONTAL BORDFORSKALING

   SØYLER: — VERTIKAL BORDFORSKALING
   MAKS BORDBREDDE 100mm

   ALLE UTVENDIGE HJØRNER AVFASES MED 20mm TREKANTLIST DER ANNET IKKE ER VIST.
6. OVERSIKT TYPISKE TVERRSNITT SE TEGN K030-15
7. BRUA SKAL BYGGES MED OVERHØYDE, SE TEGN. K030-16
8. BRUA FUNDAMENTERES PÅ SVEVENDE STÅLRØRSPELER
   - AKSE 1 OG 2: STÅLRØRSPEL Φ 813/10,0
   - AKSE 3. STÅLRØRSPEL Φ 1060/10,0.
   - AKSE 4. STÅLRØRSPEL Φ 813/12,5.
   - AKSE 5: STÅLRØRSPEL Φ 813/14,2.
9. BRUA ER DIMENSJONERT IHT Hb 184 LASTFORSKRIFTER" VERSJON 2001-1 OG IHT Hb 185 "PROSJEKTERINGSREGLER" VERSJON 2001-1

HENVISNINGER

| | | | |
|---|---|---|---|
| - STIKNINGSPLAN | SE TEGN | K030-02 |
| - PELEPLAN, DETALJER | SE TEGN: | K030-03 |
| - LANDKAR AKSE 1 | SE TEGN: | K030-04, 05 |
| - LANDKAR AKSE 5 | SE TEGN: | K030-06, 07 |
| - PELEHODER OG SØYLER | SE TEGN· | K030-12 |
| - BRUBJELKE FORM | SE TEGN: | K030-15, 16 |
| - REKKVERK/STØYSKJERM | SE TEGN | K030-27 |

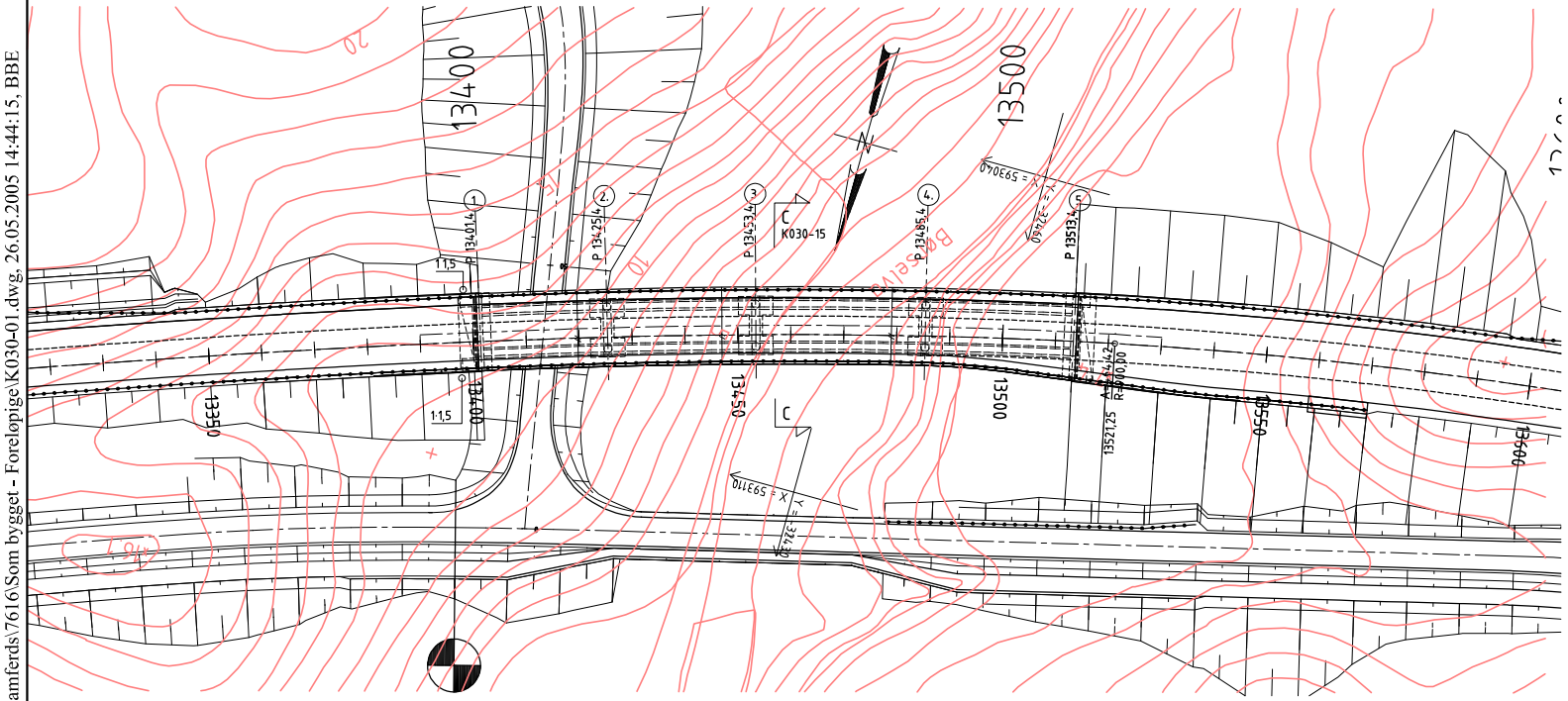


B PLAN
1500

Godkjent som arbeidstegning av
Vegdirektoratets bruavdeling i brev av 16.12.2003
Per Meaas (sign.) 16.12.2003
(prosjektansvarlig) (dato)

| Dato | Rev. | Endring | Sign. | Kontr. |
|---|---|---|---|---|
| 22.04.2005 | C | Som bygget | HPK | PME |
| 16.12.2003 | B | Arbeidstegning - korr. pelehode Akse 1 + 5, korr. stålrørspeler | BRS | EAJ |
| 22.09.2003 | A | Til kontroll | BRS | EAJ |

TEGNINGSSTATUS: Foreløpig tegning | Arbeidstegning | Anbudstegning | Som bygget X

Oppdragsgiver: Statens vegvesen Vegdirektoratet

Prosjekt: OPS-Prosjekt E39 Klett - Bårdshaug

Tegn. tittel: BRU NR: 16 - 1604 BRU OVER BØRSELVA OVERSIKT

Dato: 22.09.2003
Tegnet: BRS
Kontrollert: EAJ

OPS Selskap: Orkdalsvegen AS

Målestokk: 1:50 - 1:500

Prosjektnr.: 7616
Arkivnr.: 7616

Totalentreprenør: SKANSKA AS
Prosjekterende: ARC-JAKOBSEN
Tegn. nr.: K030-01
Rev. nr.: C

KontrollKlasse UTVIDET
MiljøKlasse MA
Betong
Betongens porevolum 4±1%
Armering B500C NS3576

J:\Arkiv\Samferds\7616\Som bygget - Foreløpige\K030-01.dwg, 26.05.2005 14:44:15, BBE

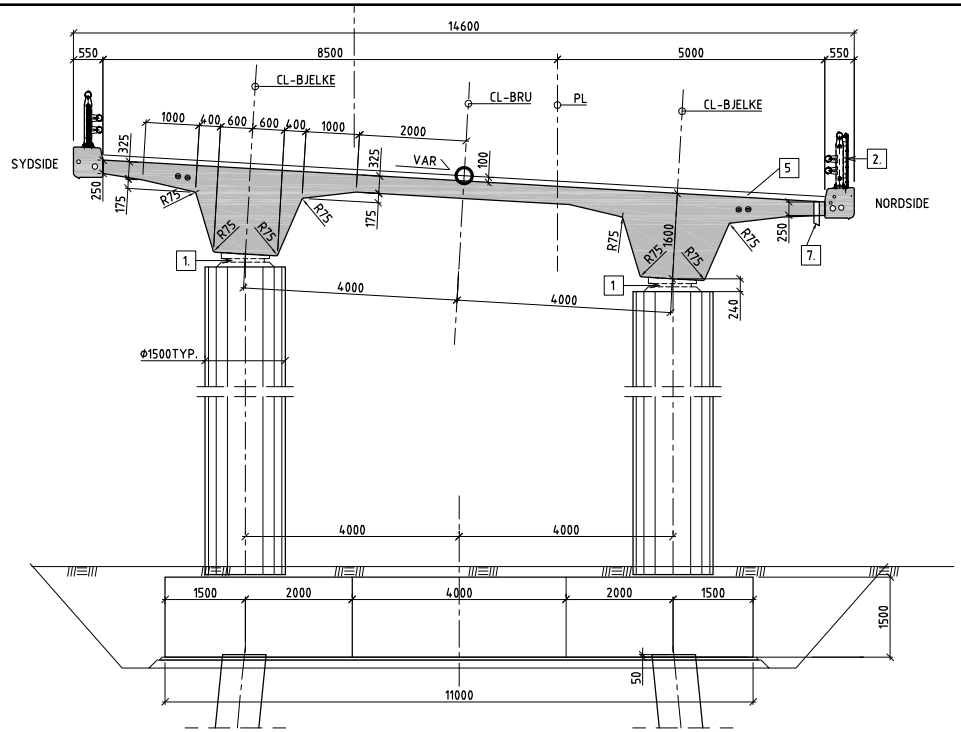


C SNITT P 13457
K030-01 1:50

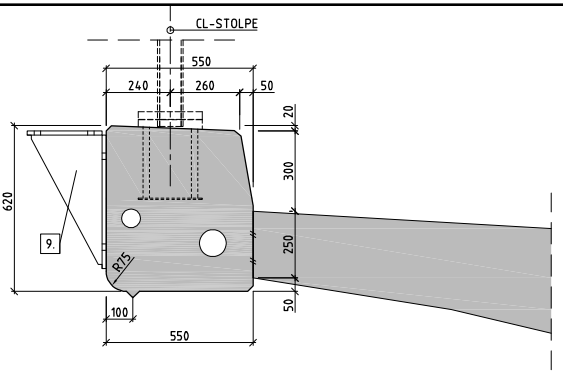


1 DETALJ
SØNDRE KANTBJELKE
1:10

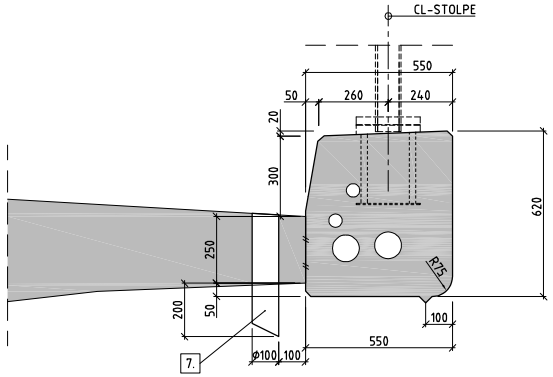


2 DETALJ
NORDRE KANTBJELKE
1:10

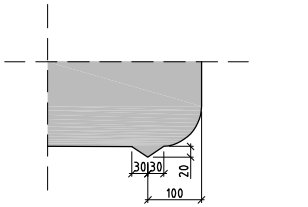


3 DETALJ DRYPPNESE
1:5

BEMERKNINGER :

1. LAGER SE TEGN K030-12 FOR BEMERKNINGER
2. STØYSKJERM H=1,2m PÅ NORDRE SIDE INTEGRERT I REKKVERK.
3. FELTVIS UTBYGGING FRA AKSE 5
4. FORSKALING BRUOVERBYGNING:
   HORISONTAL BORDFORSKALING ALLE SYNLIGE FLATER.
   ALLE UTVENDIGE HJØRNER FASES AV MED 20mm TREKANTLIST
   DER ANNET IKKE ER VIST
5. ASFALT SLITELAG MED FULL FUKTISOLERING TYPE A3-4
   IHHT. HÅNDBOK 145. SE TEGN F132
6. AVRETTING OG BEARBEIDING AV BRUDEKKE IHHT. PROSESSKODE
   -2 pkt 84 52 (84 521)
7. SLUK I PROFIL· P13405, P13440, P13478 OG P13508
   DETALJUTFORMING OG MATERIALVALG IHHT. STATENS VEGVESEN
   HÅNDBOK 145 OG PROSEESKODE -2
8. TREKKERØR.
   VENSTRE KANTBJELKE (SØNDRE)
   1 x Φ70mm FOR VEGLYS
   1 x Φ100mm FOR SKANSKA AS
   BRUPLATE VENSTRE: 4 x Φ40mm I 2 x Φ110mm VARERØR FOR SKANSKA AS

   HØYRE KANTBJELKE (NORDRE)
   2 x Φ50mm FOR STYREKABEL VAR SKILT FRA AKSE 5 OG FØRES
   UT AV KANTDRAGER I PROFIL 13500
   1 x Φ100mm FOR SKANSKA AS
   1 x Φ100mm FOR VEGDIREKTORATET
   BRUPLATE HØYRE: 4 x Φ40mm I 2 x Φ110mm VARERØR FOR
   VEIDIREKTORATET
9. KONSOLL FOR LYSMAST, SE TEGN. K000-03
   VENSTRE (SØNDRE) SIDE:
   PROFIL:13439 OG 13482

HENVISNINGER :

| | | | |
|---|---|---|---|
| - | OVERSIKT | SE TEGN: | K030-01 |
| - | PELEHODER/SØYLER | SE TEGN: | K030-12 |
| - | FORM | SE TEGN: | K030-16 |
| - | BRUPLATE/ARMERING | SE TEGN | K030-18, 19 |
| - | LAGER OG FUGER AKSE 1 | SE TEGN. | K030-23 |
| - | LAGER OG FUGER AKSE 5 | SE TEGN: | K030-24 |
| - | REKKVERK/STØYSKJERM | SE TEGN: | K000-01, K030-27 |
| - | BRAKETT FOR LYSMAST | SE TEGN· | K000-03 |

Godkjent som arbeidstegning av
Vegdirektoratets bruavdeling i brev av 16.12.2003
Per Meaas (sign.) 16.12.2003
(prosjektansvarlig) (dato)

| Dato | Rev. | Endring | Sign. | Kontr. |
|---|---|---|---|---|
| 22.04.2005 | D | Som bygget | HPK | PME |
| 21.10.2004 | C | Varerør Φ110mm for trekkerør | JKR | CHR |
| 16.12.2003 | B | Arbeidstegning - korr. trekkerør | BRS | EAJ |
| 22.09.2003 | A | Til kontroll | BRS | EAJ |

TEGNINGSSTATUS: Foreløpig tegning | Arbeidstegning | Anbudstegning | Som bygget X

Oppdragsgiver: Statens vegvesen Vegdirektoratet

Prosjekt: OPS-Prosjekt E39 Klett - Bårdshaug

Tegn. tittel: BRU NR:16 - 1604 BRU OVER BØRSELVA BRUBJELKE, FORM

Dato: 22.09.2003
Tegnet: BRS
Kontrollert: EAJ

OPS Selskap: Orkdalsvegen AS

Målestokk: 1:10, 1:50

Prosjektnr.: 7616
Arkivnr.: 7616

Totalentreprenør: SKANSKA SKANSKA AS
Prosjekterende: ARC-JAKOBSEN

Tegn. nr.: K030-15
Rev. nr.: D

Kontrollklasse UTVIDET
Miljøklasse MA SV 40
Betong Overbygning C55 Søyler C55 Øvrig C45
Betongens porevolum 5±1.5%
Armering B500C NS 3576

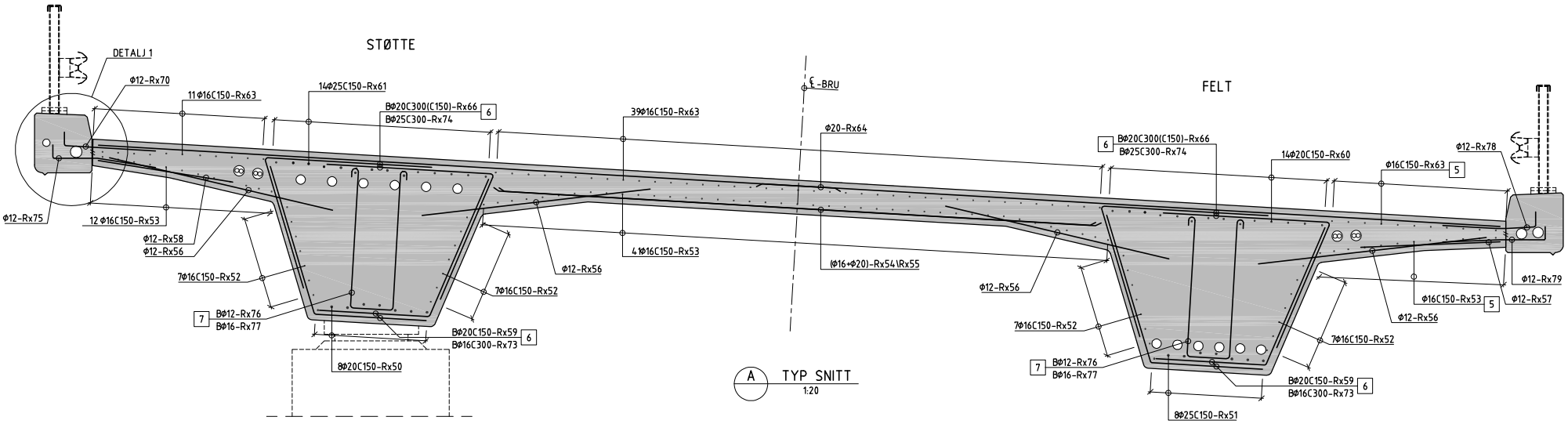


A TYP SNITT
1:20

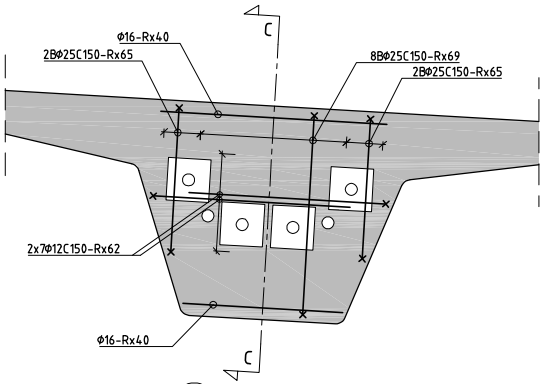


B TYP. SNITT
VED OPPSPENNING
I STØPESKJØT
1:20

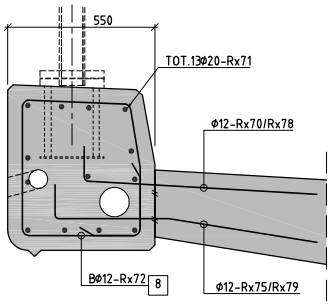


1 DETALJ
KANTBJELKE
1:10

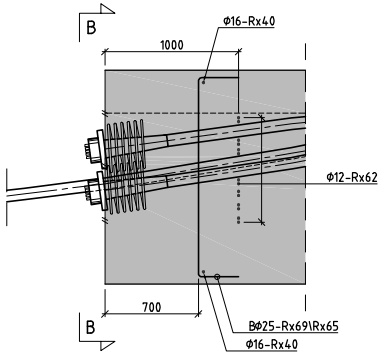


C TYP. SNITT
VED OPPSPENNING
I STØPESKJØT
1:20

4 FOR POSISJONSNUMMERERINGEN PÅ TEGNINGEN GJELDER:
x = 9 FOR AKSE 1 TIL AKSE 2-5.6m
x = 2 FOR AKSE 2-5.6m TIL AKSE 3-6.4m
x = 3 FOR AKSE 3-6.4m TIL AKSE 4-6.4m
x = 4 FOR AKSE 4-5.6m TIL AKSE 5

5 ANTALL VARIERER SE TEGN K030-18\K030-19 FOR MENGDER

6 Rx59, Rx66, Rx73, Rx74 FØRES OVER HELE BRULENGDEN MED UNNTAK FOR Rx73 OG Rx74 I DELER AV ENDEFELTENE. SE TEGN K030-18 OG K030-19 FOR OMFANG.
Rx66 OG Rx74 LEGGES FORSKJØVET 150mm SLIK AT Rx74 GIR OMFAR MED Rx73
Rx59 OG SLIK AT Rx66 GIR OMFAR MED Rx59.

7 Rx76 ERSTATTES MED Rx77 ±4m FRA STØTTE
SE TEGNING K030-18 OG K030-19 FOR OMFANG

8 DET LEGGES EN EKSTRA BØYLE PÅ HVER SIDE AV REKKVERKSFESTE.

BEMERKNINGER :

1 OVERDEKNING: TIL KONSTRUKTIV ARMERING : 55mm ± 15mm
TIL Φ12 MONTERINGSARM 40mm ± 5mm

2. OMFARSKJØT UTFØRES SOM 50Ø DER IKKE ANNET ER ANGITT
Φ12 50Ø = 600mm
Φ16 . 50Ø = 800mm
Φ20 50Ø = 1000mm
Φ25 : 50Ø = 1250mm
Φ32 : 50Ø = 1600mm
SKJØTER FORDELES SLIK AT MAKSIMALT ANNET HVERT JERN SKJØTES I SAMME SNITT.

3 BØYELISTE SIDE: Rx5-Rx7

HENVISNINGER :

| | | | |
|---|---|---|---|
| - | OVERSIKT | SE TEGN: | K030-01 |
| - | BRUBJELKE, FORM | SE TEGN | K030-15/16 |
| - | ARMERING PLATE, DEL 1 | SE TEGN: | K030-18 |
| - | ARMERING PLATE, DEL 2 | SE TEGN: | K030-19 |

Godkjent som arbeidstegning av Vegdirektoratets bruavdeling i brev av 16.12.2003
Per Meaas (sign.) 16.12.2003 (dato)
(prosjektansvarlig)

| Dato | Rev. | Endring | Sign. | Kontr. |
|---|---|---|---|---|
| 22.04.2005 | D | Som bygget | HPK | PME |
| 21.10.2004 | C | Varsrør Ø110mm for trekkerør | JKR | CHR |
| 16.12.2003 | B | Arbeidstegning - bøyler i brubjelke | BRS | EAJ |
| 22.09.2003 | A | Til kontroll | BRS | EAJ |

TEGNINGSSTATUS: Foreløpig tegning | Arbeidstegning | Anbudstegning | Som bygget X

Oppdragsgiver: Statens vegvesen Vegdirektoratet

Prosjekt: OPS-Prosjekt E39 Klett - Bårdshaug

Tegn. tittel: BRU NR. 16-1604 BRU OVER BØRSELVA BRUBJELKE ARMERING BJELKE

Dato: 22.09.2003
Tegnet: BRS
Kontrollert: EAJ

OPS Selskap: Orkdalsvegen AS

Målestokk: 1:50, 20, 10

Prosjektnr.: 7616
Arkivnr.: 7616

Totalentreprenør: SKANSKA SKANSKA AS
Prosjekterende: ARC-JAKOBSEN

Tegn. nr.: K030-17
Rev. nr.: D

Kontrollklasse UTVIDET
Miljøklasse MA SV-40
Betong Overbygning C55 Søyler C55 Øvrig C45
Betongens porevolum 5±1.5%
Armering B500C NS3576

J:\Arkiv\Samferds\7616\Som bygget - Foreløpige\K030-17.dwg, 26.05.2005 14:42:13, BBE

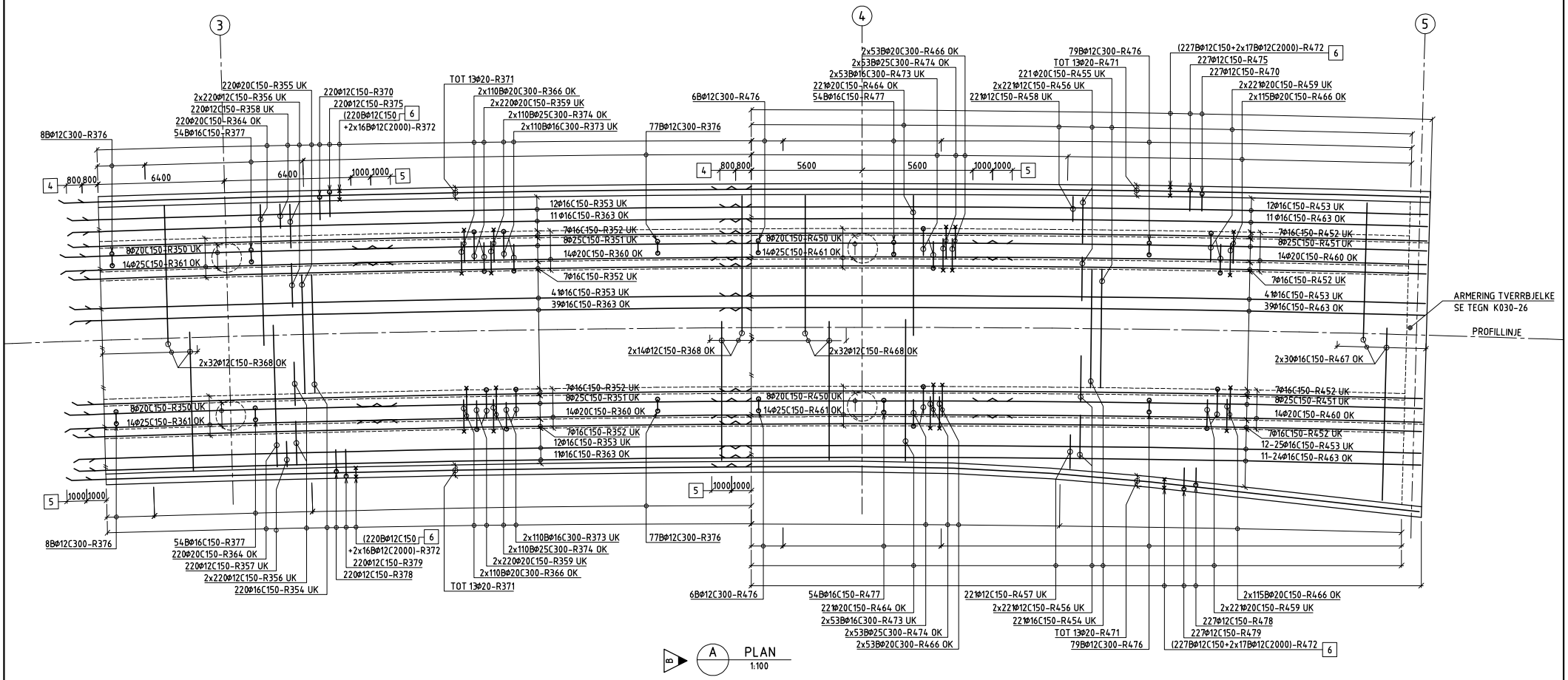


BEMERKNINGER :

1 OVERDEKNING: TIL KONSTRUKTIV ARMERING : 55mm ± 15mm
TIL Ø12 MONTERINGSARM. : 40mm ± 5mm

2 OMFARSKJØT UTFØRES SOM 50Ø DER IKKE ANNET ER ANGITT
Ø12 : 50Ø = 600mm
Ø16 : 50Ø = 800mm
Ø20 : 50Ø = 1000mm
Ø25 : 50Ø = 1250mm
Ø32 : 50Ø = 1600mm
SKJØTER FORDELES SLIK AT MAKSIMALT ANNET HVERT JERN SKJØTES I SAMME SNITT.

3 BØYELISTE SIDE R35-R37, R45-R47

4. GJELDER OMFAR VED SKJØTING AV Ø16 \ Ø16.

5 GJELDER OMFAR VED SKJØTING AV Ø20 \ Ø25

6 INKLUDERT 2 EKSTRA JERN VED HVER REKKVERKSTOLPE SE TEGN. K030-27

HENVISNINGER :

| | | |
|---|---|---|
| - OVERSIKT | SE TEGN: | K030-01 |
| - BRUBJELKE, FORM | SE TEGN: | K030-15/16 |
| - ARMERING BJELKE | SE TEGN: | K030-17 |
| - ARMERING PLATE, DEL 2 | SE TEGN. | K030-19 |
| - ARMERING TVERRBJELKE AKSE 5 | SE TEGN: | K030-26 |

Godkjent som arbeidstegning av
Vegdirektoratets bruavdeling i brev av 16.12.2003
Per Meaas (sign.) 16.12.2003 (dato)
(prosjektansvarlig)

| Dato | Rev. | Endring | Sign. | Kontr. |
|---|---|---|---|---|
| 22.04.2005 | C | Som bygget | HPK | PME |
| 16.12.2003 | B | Arbeidstegning - bøyler i brubjelke | BRS | EAJ |
| 22.09.2003 | A | Til kontroll | BRS | EAJ |

TEGNINGSSTATUS: Foreløpig tegning | Arbeidstegning | Anbudstegning | Som bygget X

Oppdragsgiver: Statens vegvesen Vegdirektoratet

Prosjekt: OPS-Prosjekt E39 Klett - Bårdshaug

Tegn. tittel: BRU NR. 16-1604 BRU OVER BØRSELVA BRUBJELKE ARMERING PLATE DEL 1

Dato: 22.09.2003
Tegnet: BRS
Kontrollert: EAJ

OPS Selskap: Orkdalsvegen AS

Målestokk: 1:100

Prosjektnr.: 7616
Arkivnr.: 7616

Totalentreprenør: SKANSKA (SKANSKA AS)
Prosjekterende: ARC-HAUGEN

Tegn. nr.: K030-18
Rev. nr.: C

KontrollKlasse UTVIDET
MiljøKlasse MA SV-40
Betong Overbygning C55 Søyler C55 Øvrig C45
Betongens porevolum 5±1.5%
Armering B500C NS3576

J:\Arkiv\Samferds\7616\Som bygget - Foreløpige\K030-18.dwg, 26.05.2005 14:42:21, BBE

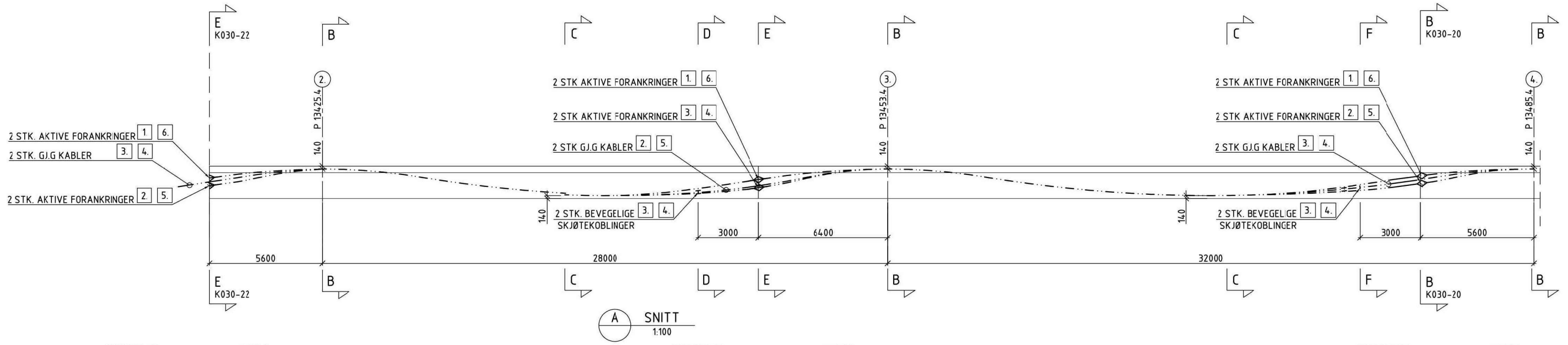

A SNITT
1:100

STØPESKJØT — AKSE 2 — STØPESKJØT — AKSE 3 — STØPESKJØT — AKSE 4

| AVSTAND "X" FRA AKSE (m) | | | -5.6 | -5,0 | -4,0 | -3,0 | -2,0 | -1,0 | 0,0 | 1,0 | 2,0 | 3,0 | 4,0 | 5,0 | 6,0 | 7,0 | 8,0 | 9,0 | 10,0 | 11,0 | 12,0 | 13,0 | 14,0 | 15,0 | 16,0 | 17,0 | 18,0 | 19,0 | 20,0 | 21,0 | 21,6 | 22,0 | 23,0 | 24,0 | 25,0 | 26,0 | 27,0 | 28,0 |
|---|---|---|---|---|---|---|---|---|---|---|---|---|---|---|---|---|---|---|---|---|---|---|---|---|---|---|---|---|---|---|---|---|---|---|---|---|---|---|
| KABEL | NR: 1 | HØYDE "A" | 990 | 1070 | 1195 | 1300 | 1385 | 1440 | 1460 | 1438 | 1370 | 1258 | 1101 | 919 | 756 | 611 | 486 | 381 | 294 | 227 | 178 | 150 | 140 | 155 | 215 | 295 | 413 | 542 | 687 | 845 | 938 | 990 | 1135 | 1250 | 1335 | 1395 | 1440 | 1460 |
| | | HØYDE "B" | -560 | -572 | -600 | -650 | -710 | -746 | -750 | -746 | -733 | -712 | -682 | -648 | -617 | -589 | -566 | -546 | -529 | -516 | -507 | -502 | -500 | -502 | -508 | -516 | -527 | -540 | -555 | -571 | -580 | -592 | -620 | -655 | -700 | -729 | -743 | -750 |
| | NR: 2 | HØYDE "A" | 610 | 710 | 921 | 1162 | 1331 | 1430 | 1460 | 1438 | 1370 | 1258 | 1101 | 919 | 756 | 611 | 486 | 381 | 294 | 227 | 178 | 150 | 140 | 148 | 165 | 200 | 250 | 323 | 420 | 541 | 628 | 690 | 852 | 1050 | 1230 | 1362 | 1437 | 1460 |
| | | HØYDE "B" | -380 | -388 | -410 | -425 | -439 | -448 | -450 | -448 | -440 | -427 | -409 | -389 | -370 | -354 | -339 | -327 | -318 | -310 | -304 | -301 | -300 | -302 | -305 | -312 | -322 | -336 | -355 | -379 | -396 | -402 | -423 | -431 | -435 | -444 | -449 | -450 |
| | NR: 3 | HØYDE "A" | 800 | 890 | 1058 | 1231 | 1358 | 1435 | 1460 | 1438 | 1370 | 1258 | 1101 | 919 | 756 | 611 | 486 | 381 | 294 | 227 | 178 | 150 | 140 | 147 | 159 | 186 | 219 | 278 | 351 | 447 | 528 | 588 | 770 | 1003 | 1209 | 1353 | 1437 | 1460 |
| | | HØYDE "B" | -150 | -150 | -150 | -150 | -150 | -150 | -150 | -149 | -147 | -142 | -136 | -130 | -123 | -118 | -113 | -109 | -106 | -103 | -101 | -100 | -100 | -101 | -103 | -107 | -112 | -121 | -132 | -146 | -158 | -157 | -156 | -154 | -152 | -151 | -150 | -150 |
| | NR: 4 | HØYDE "A" | 800 | 890 | 1058 | 1231 | 1358 | 1435 | 1460 | 1438 | 1370 | 1258 | 1101 | 919 | 756 | 611 | 486 | 381 | 294 | 227 | 178 | 150 | 140 | 147 | 159 | 186 | 219 | 278 | 351 | 447 | 528 | 588 | 770 | 1003 | 1209 | 1353 | 1437 | 1460 |
| | | HØYDE "B" | 150 | 150 | 150 | 150 | 150 | 150 | 150 | 149 | 147 | 142 | 136 | 130 | 123 | 118 | 113 | 109 | 106 | 103 | 101 | 100 | 100 | 101 | 103 | 107 | 112 | 121 | 132 | 146 | 158 | 157 | 156 | 154 | 152 | 151 | 150 | 150 |
| | NR: 5 | HØYDE "A" | 610 | 710 | 921 | 1162 | 1331 | 1430 | 1460 | 1438 | 1370 | 1258 | 1101 | 919 | 756 | 611 | 486 | 381 | 294 | 227 | 178 | 150 | 140 | 148 | 165 | 200 | 250 | 323 | 420 | 541 | 628 | 690 | 852 | 1050 | 1230 | 1362 | 1437 | 1460 |
| | | HØYDE "B" | 380 | 388 | 410 | 425 | 439 | 448 | 450 | 448 | 440 | 427 | 409 | 389 | 370 | 354 | 339 | 327 | 318 | 310 | 304 | 301 | 300 | 302 | 305 | 312 | 322 | 336 | 355 | 379 | 396 | 402 | 423 | 431 | 435 | 444 | 449 | 450 |
| | NR: 6 | HØYDE "A" | 990 | 1070 | 1195 | 1300 | 1385 | 1440 | 1460 | 1438 | 1370 | 1258 | 1101 | 919 | 756 | 611 | 486 | 381 | 294 | 227 | 178 | 150 | 140 | 155 | 215 | 295 | 413 | 542 | 687 | 845 | 938 | 990 | 1135 | 1250 | 1335 | 1395 | 1440 | 1460 |
| | | HØYDE "B" | 560 | 572 | 600 | 650 | 710 | 746 | 750 | 746 | 733 | 712 | 682 | 648 | 617 | 589 | 566 | 546 | 529 | 516 | 507 | 502 | 500 | 502 | 508 | 516 | 527 | 540 | 555 | 571 | 580 | 592 | 620 | 655 | 700 | 729 | 743 | 750 |

| AVSTAND "X" FRA AKSE (m) | | | 1,0 | 2,0 | 3,0 | 4,0 | 5,0 | 6,0 | 7,0 | 8,0 | 9,0 | 10,0 | 11,0 | 12,0 | 13,0 | 14,0 | 15,0 | 16,0 | 17,0 | 18,0 | 19,0 | 20,0 | 21,0 | 22,0 | 23,0 | 24,0 | 25,0 | 26,0 | 26,4 | 27,0 | 28,0 | 29,0 | 30,0 | 31,0 | 32,0 |
|---|---|---|---|---|---|---|---|---|---|---|---|---|---|---|---|---|---|---|---|---|---|---|---|---|---|---|---|---|---|---|---|---|---|---|---|
| KABEL | NR: 1 | HØYDE "A" | 1443 | 1391 | 1305 | 1185 | 1031 | 877 | 737 | 611 | 501 | 405 | 324 | 258 | 206 | 169 | 147 | 140 | 147 | 169 | 206 | 268 | 350 | 460 | 595 | 740 | 896 | 1062 | 1123 | 1202 | 1300 | 1373 | 1422 | 1445 | 1460 |
| | | HØYDE "B" | -747 | -737 | -721 | -698 | -669 | -640 | -613 | -589 | -568 | -550 | -535 | -522 | -513 | -505 | -501 | -500 | -501 | -503 | -507 | -514 | -523 | -536 | -551 | -567 | -584 | -603 | -610 | -627 | -663 | -700 | -730 | -746 | -750 |
| | NR: 2 | HØYDE "A" | 1443 | 1391 | 1305 | 1185 | 1031 | 877 | 737 | 611 | 501 | 405 | 324 | 258 | 206 | 169 | 147 | 140 | 147 | 169 | 206 | 248 | 298 | 350 | 407 | 482 | 578 | 692 | 748 | 860 | 1070 | 1237 | 1360 | 1441 | 1460 |
| | | HØYDE "B" | -448 | -442 | -432 | -419 | -401 | -384 | -368 | -354 | -341 | -330 | -321 | -313 | -308 | -303 | -301 | -300 | -301 | -304 | -309 | -314 | -321 | -328 | -335 | -345 | -358 | -373 | -380 | -391 | -412 | -428 | -440 | -448 | -450 |
| | NR: 3 | HØYDE "A" | 1443 | 1391 | 1305 | 1185 | 1031 | 877 | 737 | 611 | 501 | 405 | 324 | 258 | 206 | 169 | 147 | 140 | 147 | 169 | 206 | 258 | 324 | 405 | 501 | 611 | 737 | 877 | 938 | 1031 | 1185 | 1305 | 1391 | 1443 | 1460 |
| | | HØYDE "B" | -149 | -147 | -144 | -140 | -134 | -128 | -123 | -118 | -114 | -110 | -107 | -104 | -103 | -101 | -100 | -100 | -101 | -105 | -112 | -122 | -135 | -150 | -150 | -150 | -150 | -150 | -150 | -150 | -150 | -150 | -150 | -150 | -150 |
| | NR: 4 | HØYDE "A" | 1443 | 1391 | 1305 | 1185 | 1031 | 877 | 737 | 611 | 501 | 405 | 324 | 258 | 206 | 169 | 147 | 140 | 147 | 169 | 206 | 258 | 324 | 405 | 501 | 611 | 737 | 877 | 938 | 1031 | 1185 | 1305 | 1391 | 1443 | 1460 |
| | | HØYDE "B" | 149 | 147 | 144 | 140 | 134 | 128 | 123 | 118 | 114 | 110 | 107 | 104 | 103 | 101 | 100 | 100 | 101 | 105 | 112 | 122 | 135 | 150 | 150 | 150 | 150 | 150 | 150 | 150 | 150 | 150 | 150 | 150 | 150 |
| | NR: 5 | HØYDE "A" | 1443 | 1391 | 1305 | 1185 | 1031 | 877 | 737 | 611 | 501 | 405 | 324 | 258 | 206 | 169 | 147 | 140 | 147 | 169 | 206 | 248 | 298 | 350 | 407 | 482 | 578 | 692 | 748 | 860 | 1070 | 1237 | 1360 | 1441 | 1460 |
| | | HØYDE "B" | 448 | 442 | 432 | 419 | 401 | 384 | 368 | 354 | 341 | 330 | 321 | 313 | 308 | 303 | 301 | 300 | 301 | 304 | 309 | 314 | 321 | 328 | 335 | 345 | 358 | 373 | 380 | 391 | 412 | 428 | 440 | 448 | 450 |
| | NR: 6 | HØYDE "A" | 1443 | 1391 | 1305 | 1185 | 1031 | 877 | 737 | 611 | 501 | 405 | 324 | 258 | 206 | 169 | 147 | 140 | 147 | 169 | 206 | 268 | 350 | 460 | 595 | 740 | 896 | 1062 | 1123 | 1202 | 1300 | 1373 | 1422 | 1445 | 1460 |
| | | HØYDE "B" | 747 | 737 | 721 | 698 | 669 | 640 | 613 | 589 | 568 | 550 | 535 | 522 | 513 | 505 | 501 | 500 | 501 | 503 | 507 | 514 | 523 | 536 | 551 | 567 | 584 | 603 | 610 | 627 | 663 | 700 | 730 | 746 | 750 |

TABELL OVER KABELPLASSERING.

"A" = AVSTAND FRA UK TIL KABLENES ℄ I mm MÅLT VINKELRETT PÅ UK BRUBJELKE.
"B" = AVSTAND FRA ℄-BRUEJELKE TIL KABLENES ℄ I mm.

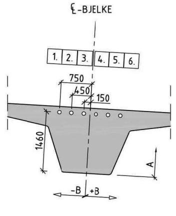

B SNITT
1:50

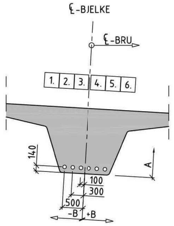

C SNITT
1:50

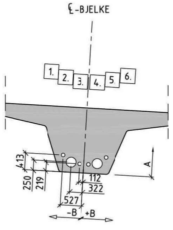

D SNITT
AKSE + 18m
1:50

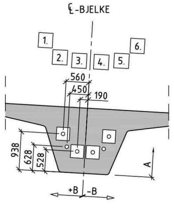

E SNITT
1:50

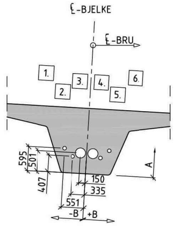

F SNITT
AKSE + 23m
1:50

BEMERKNINGER :

1. I HVER BRUBJELKE BENYTTES :
   6 STK. SPENNKABLER MED $S_{02}$ = 2806 kN pr KABEL.
2. KABLENE PLASSERES SYMMETRISK OM ℄-BRUBJELKE.
3. OPPSPENNINGSKRAFT KOMPENSERT FOR LÅSETAP
   $S = 0,8 \times S_{02}$
4. OPPSPENNINGSREKKEFØLGE:
   KABLENE SPENNES OPP SYMMETRISK OM ℄-BRUBJELKE.
5. MINIMUM BETONGFASTHET VED OPPSPENNING: 38 N/mm²
6. TILLATT AVVIK FRA ANGITT KABELPLASSERING:
   VERTIKALT: ± 10mm
   HORISONTALT: ± 20mm

HENVISNINGER :

- BRUBJELKE SPENNARMERING, ENDEFELT AKSE 4 - AKSE - 5 SE TEGN: K030-20
- BRUBJELKE SPENNARMERING, ENDEFELT AKSE 1 - AKSE 2 SE TEGN: K030-22

Godkjent som arbeidstegning av
Vegdirektoratets bruavdeling i brev av 16.12.2003
Per Meaas (sign.) 16.12.2003
(prosjektansvarlig) (dato)

| Dato | Rev. | Endring | Sign. | Kontr. |
|---|---|---|---|---|
| 22.04.2005 | C | Som bygget | HPK | PME |
| 16.12.2003 | B | Arbeidstegning | BRS | EAJ |
| 22.09.2003 | A | Til kontroll | BRS | EAJ |

| TEGNINGSSTATUS | Foreløpig tegning | | Arbeidstegning | |
|---|---|---|---|---|
| 32425 | Anbudstegning | | Som bygget | X |

Oppdragsgiver:
Statens vegvesen
Vegdirektoratet

Prosjekt:
OPS-Prosjekt
E39 Klett - Bårdshaug

Tegn. tittel:
BRU NR:16 - 1604
BRU OVER BØRSELVA
BRUBJELKE SPENNARMERING
INNERFELT AKSE 2 - AKSE 4

Dato: 22.09.2003
Tegnet: BRS
Kontrollert: EAJ

OPS Selskap
Orkdalsvegen AS

Målestokk: 1:100, 50
Prosjektnr.: 7616
Arkivnr.: 7616

Totalentreprenør: SKANSKA
SKANSKA AS

Prosjekterende: AAS-JAKOBSEN

Tegn. nr.: K030-21
Rev. nr.: C

Kontrollklasse
UTVIDET
Miljøklasse
MA Sv-40
Betong
C55
Betongens porevolum
5±1,5%
Armering
B500C
NS3576

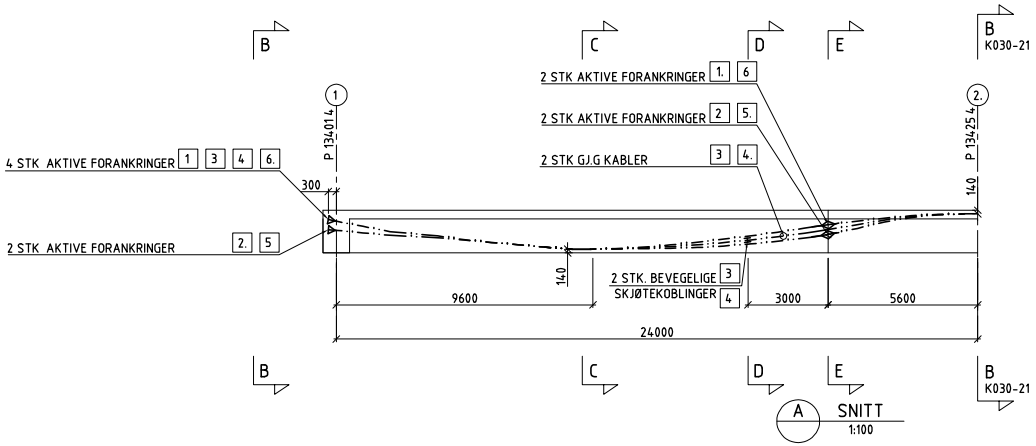


A SNITT 1:100

AKSE 1 — STØPESKJØT — AKSE 2

| AVSTAND "X" FRA AKSE (m.) | | -0.3 | 0.0 | 1.0 | 2.0 | 3.0 | 4.0 | 5.0 | 6.0 | 7.0 | 8.0 | 9.0 | 10.0 | 11.0 | 12.0 | 13.0 | 14.0 | 15.0 | 16.0 | 17.0 | 18.0 | 18.4 | 19.0 | 20.0 | 21.0 | 22.0 | 23.0 | 24.0 |
|---|---|---|---|---|---|---|---|---|---|---|---|---|---|---|---|---|---|---|---|---|---|---|---|---|---|---|---|---|
| KABEL | NR: 1 | HØYDE "A" | 1250 | 1185 | 966 | 767 | 600 | 463 | 355 | 272 | 209 | 166 | 144 | 141 | 162 | 215 | 300 | 405 | 517 | 640 | 773 | 925 | 990 | 1070 | 1195 | 1300 | 1390 | 1440 | 1460 |
| | | HØYDE "B" | -700 | -691 | -661 | -631 | -601 | -571 | -541 | -525 | -513 | -505 | -501 | -500 | -502 | -505 | -511 | -519 | -527 | -535 | -545 | -555 | -560 | -572 | -600 | -650 | -710 | -746 | -750 |
| | NR: 2 | HØYDE "A" | 870 | 841 | 744 | 647 | 549 | 452 | 355 | 272 | 209 | 166 | 144 | 141 | 152 | 163 | 176 | 203 | 259 | 336 | 437 | 553 | 610 | 710 | 921 | 1162 | 1326 | 1430 | 1460 |
| | | HØYDE "B" | -370 | -367 | -359 | -350 | -342 | -333 | -324 | -315 | -308 | -303 | -300 | -300 | -302 | -304 | -306 | -311 | -320 | -333 | -351 | -370 | -380 | -388 | -410 | -425 | -439 | -448 | -450 |
| | NR: 3 | HØYDE "A" | 1250 | 1185 | 966 | 767 | 600 | 463 | 355 | 272 | 209 | 166 | 144 | 141 | 157 | 189 | 238 | 304 | 388 | 488 | 605 | 739 | 800 | 890 | 1058 | 1231 | 1358 | 1435 | 1460 |
| | | HØYDE "B" | -190 | -185 | -170 | -154 | -139 | -124 | -108 | -105 | -103 | -101 | -100 | -100 | -113 | -125 | -138 | -150 | -150 | -150 | -150 | -150 | -150 | -150 | -150 | -150 | -150 | -150 | -150 |
| | NR. 4 | HØYDE "A" | 1250 | 1185 | 966 | 767 | 600 | 463 | 355 | 272 | 209 | 166 | 144 | 141 | 157 | 189 | 238 | 304 | 388 | 488 | 605 | 739 | 800 | 890 | 1058 | 1231 | 1358 | 1435 | 1460 |
| | | HØYDE "B" | 190 | 185 | 170 | 154 | 139 | 124 | 108 | 105 | 103 | 101 | 100 | 100 | 113 | 125 | 138 | 150 | 150 | 150 | 150 | 150 | 150 | 150 | 150 | 150 | 150 | 150 | 150 |
| | NR: 5 | HØYDE "A" | 870 | 841 | 744 | 647 | 549 | 452 | 355 | 272 | 209 | 166 | 144 | 141 | 152 | 163 | 176 | 203 | 259 | 336 | 437 | 553 | 610 | 710 | 921 | 1162 | 1326 | 1430 | 1460 |
| | | HØYDE "B" | 370 | 367 | 359 | 350 | 342 | 333 | 324 | 315 | 308 | 303 | 300 | 300 | 302 | 304 | 306 | 311 | 320 | 333 | 351 | 370 | 380 | 388 | 410 | 425 | 439 | 448 | 450 |
| | NR: 6 | HØYDE "A" | 1250 | 1185 | 966 | 767 | 600 | 463 | 355 | 272 | 209 | 166 | 144 | 141 | 162 | 215 | 300 | 405 | 517 | 640 | 773 | 925 | 990 | 1070 | 1195 | 1300 | 1390 | 1440 | 1460 |
| | | HØYDE "B" | 700 | 691 | 661 | 631 | 601 | 571 | 541 | 525 | 513 | 505 | 501 | 500 | 502 | 505 | 511 | 519 | 527 | 535 | 545 | 555 | 560 | 572 | 600 | 650 | 710 | 746 | 750 |

TABELL OVER KABELPLASSERING.

"A" = AVSTAND FRA UK TIL KABLENES ℄ I mm MÅLT VINKELRETT PÅ UK BRUBJELKE
"B" = AVSTAND FRA ℄-BRUBJELKE TIL KABLENES ℄ I mm

BEMERKNINGER.

1. I HVER BRUBJELKE BENYTTES :
   6 STK SPENNKABLER MED $S_{02}$ = 2806 kN pr KABEL
2. KABLENE PLASSERES SYMMETRISK OM ℄-BRUBJELKE.
3. OPPSPENNINGSKRAFT KOMPENSERT FOR LÅSETAP
   $S = 0{,}8 \times S_{02}$
4. OPPSPENNINGSREKKEFØLGE:
   KABLENE SPENNES OPP SYMMETRISK OM ℄-BRUBJELKE
5. MINIMUM BETONGFASTHET VED OPPSPENNING: 38 N/mm²
6. TILLATT AVVIK FRA ANGITT KABELPLASSERING:
   VERTIKALT. ± 10mm
   HORISONTALT: ± 20mm

HENVISNINGER.

- BRUBJELKE SPENNARMERING, INNERFELT AKSE 2 - AKSE 4 — SE TEGN. K030-21
- BRUBJELKE SPENNARMERING, ENDEFELT AKSE 4 - AKSE 5 — SE TEGN: K030-20

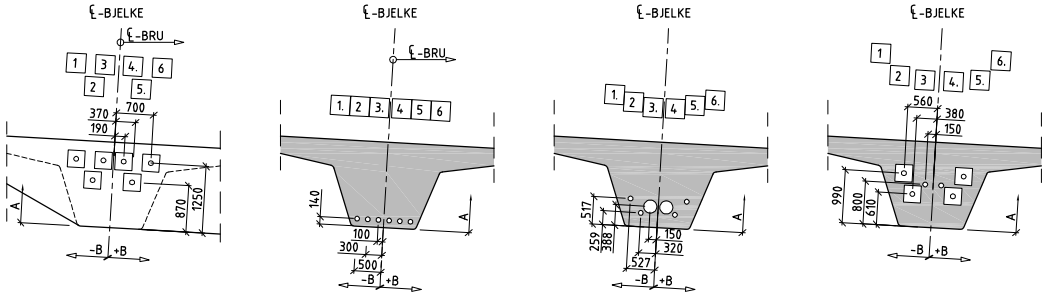


B OPPRISS 1.50

C SNITT 1.50

D SNITT AKSE 1 + 15m 1:50

E SNITT 1.50

Godkjent som arbeidstegning av Vegdirektoratets bruavdeling i brev av 16.12.2003
Per Meaas (sign.) 16.12.2003 (dato)
(prosjektansvarlig)

| Dato | Rev. | Endring | Sign. | Kontr. |
|---|---|---|---|---|
| 22.04.2005 | C | Som bygget | HPK | PME |
| 16.12.2003 | B | Arbeidstegning | BRS | EAJ |
| 22.09.2003 | A | Til kontroll | BRS | EAJ |

TEGNINGSSTATUS: Foreløpig tegning | Arbeidstegning | Anbudstegning | Som bygget X

Oppdragsgiver: Statens vegvesen Vegdirektoratet

Prosjekt: OPS-Prosjekt E39 Klett - Bårdshaug

Tegn. tittel: BRU NR: 16 - 1604 BRU OVER BØRSELVA BRUBJELKE SPENNARMERING ENDEFELT AKSE 1 - AKSE 2

Dato: 22.09.2003
Tegnet: BRS
Kontrollert: EAJ

OPS Selskap: Orkdalsvegen AS

Målestokk: 1:100, 50

Prosjektnr.: 7616 | Arkivnr.: 7616

Totalentreprenør: SKANSKA AS | Prosjekterende: ARC-HAUGEN

Tegn. nr.: K030-22 | Rev. nr.: C

Kontrollklasse UTVIDET
Miljøklasse MA Sv-40
Betong C55
Betongens porevolum 5±1,5%
Armering B500C NS3576

J:\Arkiv\Samferds\7616\Som bygget - Foreløpige\K030-22.dwg, 26.05.2005 14:42:51, BBE

Hedvig Vestad Magnus Vestad

NTNU
Norwegian University of
Science and Technology